Connectedness percolation of rods in two dimensions and in the smectic phase

de Bruijn, René A.J.

Award date:
2019

Eindhoven University of Technology

Connectedness percolation of rods in two dimensions and in the smectic phase

R.A.J. de Bruijn
0821035

supervisors
Prof.dr.ir. P.P.A.M. van der Schoot
S.P. Finner MSc

July 24, 2019

Abstract

Polymeric materials can be made electrically conductive by adding a sufficient amount of conductive nanoparticles to the material. Slender nanoparticles are extensively used for this purpose, since only a small amount of nanofillers is required to achieve the desired conductivity increase. The formation of a system-spanning particle network is paramount for these properties to emerge, and the density at which this occurs is the percolation threshold. We investigate percolation in two distinct models. To investigate percolation in thin film materials, we employ a two-dimensional model. Previous attempts to study percolation in two dimensions via integral equation theories have shown unsatisfactory results, hence we investigate the Percus-Yevick closure for this purpose. Secondly, we investigate how the positional order of the smectic-A phase affects the percolation threshold of perfectly aligned cylinders. We find not only that Percus-Yevick is inaccurate in two dimensions, but that it gives no indication of the presence of a percolation threshold at all for both spherical and anisometric particles. The effect of the positional order within the smectic-A phase is limited to a small shift in the percolation threshold, as compared to a nematic reference fluid. Our current method allows us to investigate the physical dimension of the particle clusters *within* the smectic layer, but not perpendicular to it. It therefore remains an open question whether a material enhanced by nanofillers could exhibit in-layer-percolation, while remaining an insulator in the third dimension, which might be relevant for technological applications.

Contents

Chapter 1

Introduction

1.1 Percolation

The mechanical and transport properties of polymeric materials can be enhanced by adding a sufficient amount of nanoparticles. The formation of a material-spanning (or percolating) network of the nanoparticles is often paramount for these properties to emerge. Highly anisometric particles, such as carbon nanotubes, have been extensively researched, and have already showcased a plethora of applications such as improving the quality of lithium ion batteries, novel sensors and printable electronics made on plastic substrates [1–3].

The critical density at which the material-spanning network is formed is generally referred to as the percolation threshold. At the percolation threshold, the electrical conductivity can improve by many orders of magnitude, as illustrated by Figure 1.1. Experimentally, the difference in conductivity just below and just above the percolation threshold for carbon nanotubes has been observed to be in the range of ten orders of magnitude, but depends sensibly on both the host material and the type of nanoparticles [4]. For many technological applications, the percolation threshold needs to be as low as possible, in particular for materials that need to remain transparent [5, 6]. Many different factors influence the formation of the percolating networks, and understanding these effects on a fundamental level can facilitate the rational design of nanocomposite materials. Effects like polydispersity, (externally tuned) particle alignment and shape defects of slender nanoparticles on the percolation threshold in bulk material are already understood [7–10]. Yet, some open questions remain on the effects of, for instance, density fluctuations, local aggregation of particles and physical constraints in thin-film materials. In this thesis, we aim to improve the understanding of two of these effects on percolation. In the first part of this thesis, we investigate percolation in thin film materials by employing a two-dimensional model. In the second part, we investigate how the spatial density modulation of a smectic-A liquid crystal phase influences network formation.

1.2 Thin Films

If a material is sufficiently thin, the regime of (quasi-)two-dimensional materials is entered and network formation can effectively behave similarly to that in a two-dimensional material [11]. The

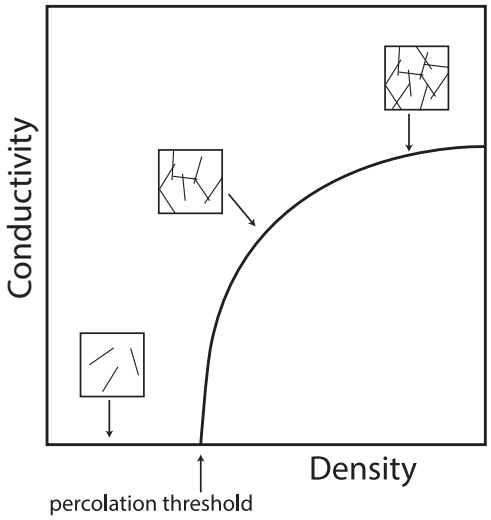

Figure 1.1: A schematic view of the conductivity of a nanocomposite as a function of the density. Below the percolation threshold, no percolating cluster exists and the material is non conductive. At the percolation threshold the conductivity increases by many order of magnitude due to the presence of a material-spanning nanoparticle network.

easiest method to model highly elongated nanofillers in two dimensions is by describing them as infinitely thin sticks that count as connected if they overlap. Various attempts have been made to theoretically describe percolation in such a two-dimensional model using integral equation theories, yet quantitative agreement with the rising number of Monte Carlo simulation results has, to our knowledge, not been achieved [12–15]. Monte Carlo simulations have indicated that particle alignment and the effect of the particle aspect ratio are equally important in two dimensions as in three dimensions. Additionally, the reduction of dimensionality limits the degrees of freedom of the particles, and therefore alignment, defects or the formation of liquid-crystalline metaphases might have different effects compared to percolation in three dimensions. In our effort to improve on previous attempts describing percolation in two dimensions, we apply Percus-Yevick theory. This theory has been extended from liquid state theory to percolation by Coniglio *et al.* [16] and has, to our knowledge, not been applied to percolation theory in two dimensions.

1.3 Liquid crystals

Anisometric particles can form liquid crystal phases, which are partially ordered metaphases between the liquid and the crystal phase. The phase behaviour of hard particles suspended in a liquid host medium is driven by density, and the resulting liquid crystal is called lyotropic. Discussing the full phase behaviour of lyotropic liquid crystals is beyond the scope of this work and we limit our treatment to the isotropic, nematic and smectic-A phase. At low particle concentration, rod-like particles form the isotropic phase, as indicated in the left diagram in Figure 1.2. The isotropic phase is a phase in which only short-range positional and rotational order is present, and the phase

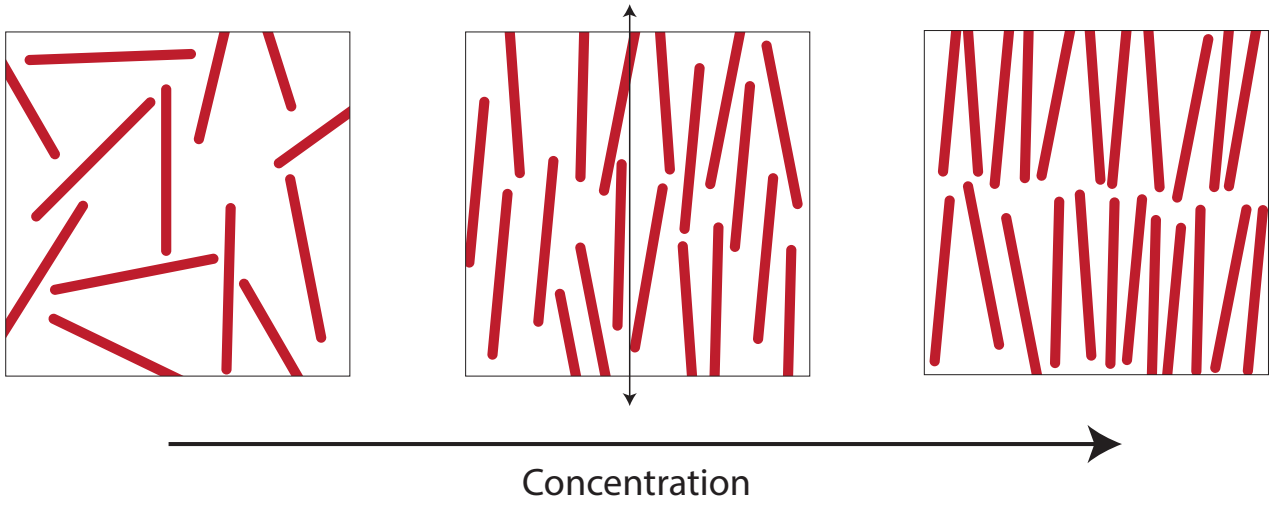

Figure 1.2: Schematic representation of the isotropic phase (left), nematic phase (middle) and smectic-A phase (right). Increasing the concentration drives the transition between the phases.

is invariant under both rotation and translation. Upon increasing the particle concentration, it is entropically favourable to break the orientational symmetry to gain translational entropy. This partly aligned phase is called the nematic phase. In the nematic phase, the rotational invariance breaks and particles align along a nematic director $\vec{n}$, indicated by the arrow in the middle diagram in Figure 1.2. This is a two-sided vector due to the top-down symmetry of rod-like particles. The rotational symmetry is only partly broken, however, since the phase is still invariant under a rotation around the director. The degree of alignment increases with the density and is usually described by the nematic order parameter

$$S = \langle P_2(\cos\theta) \rangle, \tag{1.1}$$

where $P_2(x) = \frac{3}{2}x^2 - \frac{1}{2}$ is the second order Legendre polynomial, and θ is the angle between the long axis of the particle and the local nematic director. The nematic order parameter S ranges from $-1/2$ to 1, where $S = 0$ corresponds to the isotropic phase (no alignment) and $S = 1$ indicates perfect alignment. Negative values of S correspond to alignment in the plane away from the nematic director $\vec{n}$. The isotropic-nematic transition is often described via Onsager theory, which is exact in the limit of infinitely slender rods.

Upon increasing the density even further, a transition to the smectic-A phase occurs. The translational invariance of the material breaks, as the centres of mass of the rods become located in well-defined layers. The translational invariance does not break inside the layers, as the rods still behave liquid-like inside each layer. The density-profile of a smectic-A phase is usually described by a harmonic expansion in the density

$$\rho(\vec{r}, \theta) = \rho_0(\theta) + \rho_0'(\theta)\cos(\vec{q}\cdot\vec{r}) + \cdots, \tag{1.2}$$

where $\vec{q}$ is the wave vector along which the layering occurs and which is related to the wavelength λ of the density modulation by $\lambda = \frac{2\pi}{|\vec{q}|}$.

1.4 Liquid crystal phases in two dimensions

The above description of liquid crystals is valid in three dimensions. In two dimensions, however, the behaviour of liquid crystals, especially in the smectic-A phase, is more subtle. The isotropic and the nematic phase are predicted in a two dimensional material and behave relatively similar to their three-dimensional counterparts. Theoretical predictions via the Onsager theory, while celebrated in three dimensions, should be used with caution, as the approximations that it is based on are generally not justified in two dimensions. Some extensions to Onsager theory have been proposed, such as adding higher order particle interactions or using more sophisticated theories [17, 18].

The presence of the smectic-A phase in two dimensions is difficult to establish and is a matter of definition. While in three dimension the smectic-A phase is a phase with positional order along the director and liquid-like behaviour perpendicular to the director, this liquid-like behaviour is difficult to establish in a two-dimensional fluid. The difference between a crystalline phase and a smectic phase has recently been made by associating a change in the decay of correlations between particles along a layer with a change from smectic-A (exponential decay) to crystalline (algebraic decay) behaviour [18].

1.5 Thesis outline

In this thesis, we investigate percolation in a two-dimensional model using the Percus-Yevick closure, and the influence of the positional ordering on percolation in the smectic-A phase. In chapter 2 we describe the relevant theory used to describe percolation. We have structured the remainder of this thesis in two parts. First, we investigate the Percus-Yevick closure in two dimensions. Secondly, we extend the connectedness percolation formalism to investigate the influence of a smectic-A phase on percolation in three dimensions. In detail:

Part I

- In chapter 3, we derive Percus-Yevick theory for percolation and review properties of the accuracy and a duality with liquid state theory Percus-Yevick. We demonstrate how Percus-Yevick is normally solved.
- In chapter 4, we extend Percus-Yevick theory to percolation of two dimensional anisometric particles. We discuss the accuracy of the Percus-Yevick closure by calculating pair connectedness functions and comparing it with respect to Monte Carlo simulations. Additionally, we discuss methods to improve upon the Percus-Yevick closure.

Part II

- In chapter 5, we move on to the model of hard cylinders in three dimensions in the smectic-A phase. To derive the density distribution function of the smectic-A phase in a perfectly aligned cylinder fluid, we apply a bifurcation analysis within the framework of density functional theory.

- In chapter 6, we reformulate connectedness percolation theory to investigate the effect of the spatially inhomogeneous smectic-A phase on percolation. We apply this method on the hard cylinder fluid to investigate the effects of the smectic-A phase on percolation.

- In chapter 7, we summarise the main methods and results of this study. We draw conclusions on the accuracy of Percus-Yevick closure in two dimensions and on the preliminary results on percolation in the smectic-A phase. Furthermore, we give an outlook for future research and the improvement of the methods and models used in this thesis.

Chapter 2

Continuum Connectedness Percolation

Several formalisms have been used to study percolation theoretically, *e.g.*, percolation on a lattice, a mapping between continuum percolation to a lattice and full continuum models. In this thesis, we use the connectedness percolation theory framework that was first derived by Coniglio *et al.* [16]. This chapter focusses on the necessary theoretical ingredients and tools. The theory we present here is based on the descriptions and derivations by [8, 16, 19], and we refer any interested reader to Coniglio *et al.* [16] for an in-depth derivation of connectedness percolation theory.

2.1 Clusters

One of the key concepts in percolation theory is a cluster. A cluster is a collection of particles that are somehow connected to each other. Since multiple clusters of different size can exist simultaneously, we use the weight-averaged cluster size S as a measure for cluster formation. The weight-averaged cluster size can be obtained as function of the number of clusters n_k consisting of k particles. The probability that a randomly chosen particle is part of this cluster is $s_k = kn_k/N$, where $N = \sum_k kn_k$ is the total number of particles. Hence, we can write S as

$$S = \sum_k k s_k = \frac{\sum_k k^2 n_k}{\sum_k k n_k}, \tag{2.1}$$

which can be rewritten to

$$S = \frac{\sum_k k n_k + k(k-1)n_k}{N} = 1 + \frac{\sum_k k(k-1)n_k}{N}. \tag{2.2}$$

Next, given any distribution of n_k, the total number of pairs of particles that have a direct or an indirect connection within the same cluster, N_c, is given by

$$N_c = \sum_k \binom{k}{2} n_k = \frac{1}{2}\sum_k k(k-1)n_k. \tag{2.3}$$

Inserting this definition in Equation (2.2), we obtain

$$S = 1 + \frac{2N_c}{N}, \tag{2.4}$$

where the first term on the right hand side comes from choosing a test particle, as a cluster always consists of at least one particle. The second term stems from connections that the test particle has with other particles.

The total number of pairs of particles with direct or indirect connections can be calculated from concepts from liquid state theory. For simplicity and notational convenience, we first assume spherical particles of equal size and discuss afterwards how to extend this to non-spherical particles. A useful concept from liquid state theory is the radial distribution function $g(\vec{r}_1, \vec{r}_2)$, which measures how particles locally order around a test particle [19]. The radial distribution function is defined as

$$g(\vec{r}_1, \vec{r}_2) = \frac{\rho^{(2)}(\vec{r}_1, \vec{r}_2)}{\rho^{(1)}(\vec{r}_1)\rho^{(1)}(\vec{r}_2)}, \tag{2.5}$$

where $\rho^{(2)}(\vec{r}_1, \vec{r}_2)\mathrm{d}\vec{r}_1\mathrm{d}\vec{r}_2$ is the pair density distribution. This density distribution gives the probability of finding a particle at position $\vec{r}_1$ and a particle at $\vec{r}_2$, irrespective of the position of all other particles. The singlet-density distribution $\rho^{(1)}(\vec{r}_i)$ is the local particle density at position $\vec{r}_i$.

The definition of $g(\vec{r}_1, \vec{r}_2)$ implies that it can be separated into two different contributions, one contribution that is due to particles that are connected, and one contribution that arises from particles that are not part of the same cluster. Hence, we can write

$$g(\vec{r}_1, \vec{r}_2) = P(\vec{r}_1, \vec{r}_2) + D(\vec{r}_1, \vec{r}_2), \tag{2.6}$$

where $P(\vec{r}_1, \vec{r}_2)$ is the pair connectedness function that is due to particles that are in the same cluster, irrespective of all other particles. Similarly, $D(\vec{r}_1, \vec{r}_2)$ is the contribution that arises from the particles that are *not* in the same cluster. The probability that the particles at $\vec{r}_1$ and $\vec{r}_2$ are connected is then given by $\rho^{(1)}(\vec{r}_1)\rho^{(1)}(\vec{r}_2)P(\vec{r}_1, \vec{r}_2)\mathrm{d}\vec{r}_1\mathrm{d}\vec{r}_2$. These definitions imply that we can write N_c as

$$N_c = \frac{1}{2}\int\int \mathrm{d}\vec{r}_1\mathrm{d}\vec{r}_2\rho^{(1)}(\vec{r}_1)\rho^{(1)}(\vec{r}_2)P(\vec{r}_1, \vec{r}_2), \tag{2.7}$$

where the factor $\frac{1}{2}$ compensates for double counting. Hence, the mean cluster size S, as defined in Equation (2.4), can be written as

$$S = 1 + \frac{1}{N}\int\int \mathrm{d}\vec{r}_1\mathrm{d}\vec{r}_2\rho^{(1)}(\vec{r}_1)\rho^{(1)}(\vec{r}_2)P(\vec{r}_1, \vec{r}_2). \tag{2.8}$$

This definition of the mean cluster size is exact and valid for any density distribution $\rho^{(1)}(\vec{r}_1)$. For an isotropic fluid, where $\rho^{(1)}(\vec{r}_1) = \rho$, the pair connectedness function $P(\vec{r}_1, \vec{r}_2)$ only depends on the distance $\vec{r}_{12} = |\vec{r}_1 - \vec{r}_2|$ between two particles. Hence, the isotropic mean cluster size reads

$$S = 1 + \frac{\rho^2}{N}\int\int \mathrm{d}\vec{r}_1\mathrm{d}\vec{r}_2P(|\vec{r}_1 - \vec{r}_2|). \tag{2.9}$$

Using the translational invariance of $P(|\vec{r}_1 - \vec{r}_2|)$, this can be written as

$$S = 1 + \rho\int \mathrm{d}\vec{r}_{12}P(\vec{r}_{12}) = 1 + \rho\lim_{\vec{q}\to\vec{0}}\widehat{P}(\vec{q}), \tag{2.10}$$

where the Fourier transform $\widehat{P}(\vec{q}) = \int \mathrm{d}\vec{r} P(\vec{r}) \exp(i\vec{q}\cdot\vec{r})$ is introduced, with $\vec{q}$ being the wave vector.

For particles of anisometric shape we need to introduce their orientation as an additional degree of freedom. We characterise this orientation by the unit vector $\vec{u}$, and the orientational distribution is described by the function $\psi(\vec{u})$. Extending the definition of the mean cluster size (2.10) is now straightforward by including the orientational dependency of both particles.

$$S = 1 + \rho \int \mathrm{d}\vec{u}\psi(\vec{u}) \int \mathrm{d}\vec{u}'\psi(\vec{u}') \int \mathrm{d}\vec{r}_{12} P(\vec{r}_{12}, \vec{u}, \vec{u}') = 1 + \rho \lim_{\vec{q}\to\vec{0}} \langle\langle \hat{P}(\vec{q}, \vec{u}, \vec{u}')\rangle_u\rangle_{u'}. \tag{2.11}$$

Here, the orientational average is $\langle(\dots)\rangle_u = \int \mathrm{d}\vec{u}(\dots)\psi(\vec{u})$ [8].

The onset of a material-spanning cluster takes place if the mean cluster size S diverges, which implies that, in the thermodynamic limit, at least one cluster exists with infinitely many particles. The critical density ρ_p at which this happens is called the percolation threshold.

2.2 The connectedness Ornstein-Zernike Equation

To calculate the mean cluster size S from Equation (2.11), we need a method to calculate the pair connectedness function $P(\vec{r}_1, \vec{r}_2)$. This function can be calculated from the connectedness Ornstein-Zernike equation [16], a general expression of which is given by

$$\begin{aligned} P(\vec{r}_1, \vec{r}_2, \vec{u}_1, \vec{u}_2) =& C^+(\vec{r}_1, \vec{r}_2, \vec{u}_1, \vec{u}_2) + \\ & \int \mathrm{d}\vec{u}_3\psi(\vec{u}_3) \int \mathrm{d}\vec{r}_3\rho^{(1)}(\vec{r}_3) C^+(\vec{r}_1, \vec{r}_3, \vec{u}_1, \vec{u}_3) P(\vec{r}_3, \vec{r}_2, \vec{u}_3, \vec{u}_2). \end{aligned} \tag{2.12}$$

The connectedness Ornstein-Zernike equation links the unknown pair connectedness function $P(\vec{r}_1, \vec{r}_2, \vec{u}_1, \vec{u}_2)$ to the direct connectedness function $C^+(\vec{r}_1, \vec{r}_2, \vec{u}_1, \vec{u}_2)$. The direct connectedness function $C^+(\vec{r}_1, \vec{r}_2, \vec{u}_1, \vec{u}_2)$ represents all connections between two particles that are devoid of so-called 'bottleneck particles', *i.e.*, if we were to remove an arbitrary intermediate particle from the connection, the two particles at $\vec{r}_1$ and $\vec{r}_2$ would still be connected. The pair connectedness function $P(\vec{r}_1, \vec{r}_2, \vec{u}_1, \vec{u}_2)$ represents all possible connections, including connections with one or more bottleneck particles. The second term in the Ornstein-Zernike Equation (2.12) represents all possible ways to connect the particles at $\vec{r}_1$ and $\vec{r}_2$ via these bottleneck particles. Connections that have a bottleneck particle are called *nodal* connections.

Equation (2.12) simplifies in Fourier domain for a constant density distribution $\rho^{(1)}(\vec{r}_3) = \rho$ to the algebraic equation

$$\widehat{P}(\vec{q}, \vec{u}_1, \vec{u}_2) = \widehat{C}^+(\vec{q}, \vec{u}_1, \vec{u}_2) + \rho\langle \widehat{C}^+(\vec{q}, \vec{u}_1, \vec{u}_3)\widehat{P}(\vec{q}, \vec{u}_3, \vec{u}_2)\rangle_{\vec{u}_3}, \tag{2.13}$$

where $\widehat{C}^+(\vec{q}, \vec{u}_1, \vec{u}_2)$ is the Fourier transform of the direct connectedness function. While this simplification is often not possible when the density $\rho^{(1)}(\vec{r}_3)$ is non-constant, we show a special case in chapter 6 for which it can be similarly simplified. If the angular distribution is uniform, we can simplify Equation (2.13) even further to

$$\langle\langle \widehat{P}(\vec{q},\vec{u}_1,\vec{u}_2)\rangle_{\vec{u}_1}\rangle_{\vec{u}_2} = \frac{\langle\langle \widehat{C}^+(\vec{q},\vec{u}_1,\vec{u}_2)\rangle_{\vec{u}_1}\rangle_{\vec{u}_2}}{1-\langle\langle \widehat{C}^+(\vec{q},\vec{u}_1,\vec{u}_2)\rangle_{\vec{u}_1}\rangle_{\vec{u}_2}}. \tag{2.14}$$

Hence, in an isotropic suspension the percolation threshold is obtained as

$$\rho_p = \frac{1}{\langle\langle \widehat{C}^+(0,\vec{u}_1,\vec{u}_2)\rangle_{\vec{u}_1}\rangle_{\vec{u}_2}}. \tag{2.15}$$

While the connectedness Ornstein-Zernike Equation (2.12) presents a way to calculate $P(\vec{r}_1,\vec{r}_2,\vec{u}_1,\vec{u}_2)$ from $C^+(\vec{r}_1,\vec{r}_2,\vec{u}_1,\vec{u}_2)$, $C^+(\vec{r}_1,\vec{r}_2,\vec{u}_1,\vec{u}_2)$ cannot be calculated exactly. Therefore we need a secondary (approximate) closure relation that either proposes a specific expression for $C^+(\vec{r}_1,\vec{r}_2,\vec{u}_1,\vec{u}_2)$ or a secondary equation to relate $P(\vec{r}_1,\vec{r}_2,\vec{u}_1,\vec{u}_2)$ and $C^+(\vec{r}_1,\vec{r}_2,\vec{u}_1,\vec{u}_2)$. Several percolation closure relations exists and most of them are based on corresponding ideas from liquid state theory, where several very accurate closures have been developed [19]. We discuss how to derive these closures in detail in the next section.

2.3 Closure theory

In this section we discuss several closures and what their physical basis is. Up to this point, Equation (2.13) and Equation (2.11) and the functions P and C^+ are quite abstract. To facilitate our discussion of closure relations, we use some elements from graph theory, since these functions can be neatly expanded in graphs (or diagrams). We only discuss relevant concepts of graph theory and refer any interested reader to Hansen and McDonald [19] and references therein.

We start by defining the Mayer f-function, which is a useful quantity in percolation as well as liquid state theory. The Mayer f-function is defined as

$$f(1,2) = \exp(-\beta U(1,2)) - 1, \tag{2.16}$$

where $\beta = (k_B T)^{-1}$, with k_B the Boltzmann constant and T the temperature, and $U(1,2)$ is the interaction potential between particles 1 and 2. Here, $(1,2)$ is a simplified notation for $(\vec{r}_1,\vec{u}_1,\vec{r}_2,\vec{u}_2)$. For particles with a hard core, for example, the potential and the Mayer function can have two different values: $U(1,2)=\infty$ and $f(1,2)=-1$ if the particles overlap, otherwise $U(1,2)=0$ and $f(1,2)=0$. Similar to the definition of $P(1,2)$, it turns out useful to split $f(1,2)$ into two different functions

$$f(1,2) = f^+(1,2) + f^*(1,2), \tag{2.17}$$

where

$$f^+(1,2) = \exp(-\beta u^+(1,2)) \tag{2.18}$$

is the connectedness Mayer function, and

$$f^*(1,2) = \exp(-\beta u^*(1,2)) - 1 \tag{2.19}$$

is the blocking Mayer function. Here, $u^+(1,2)$ is the connectedness potential and $u^*(1,2)$ is the blocking potential. How we determine these potentials is dependent on the connectivity criterion for particle pairs. For example in models with ideal particles, *i.e.*, $f(1,2) = 0$ everywhere, we can define *particle overlap* as the definition of connection. This means that if particles overlap we obtain

$$u^+(1,2) = 0, \qquad f^+(1,2) = 1, \qquad u^*(1,2) = \infty, \qquad f^*(1,2) = -1, \tag{2.20}$$

and if particles do not overlap we obtain

$$u^+(1,2) = \infty, \qquad f^+(1,2) = 0, \qquad u^*(1,2) = 0, \qquad f^*(1,2) = 0. \tag{2.21}$$

The connections between particles in connectedness percolation are well-described using these connectedness- and blocking-Mayer functions, which can be used to obtain a formally exact expression for the direct connectedness function $C^+(1,2)$. For this purpose we define a set of diagrams that consists of two types of particles: 'white 1-nodes', which are the labelled particles 1 and 2, and 'black ρ-nodes', which are unlabelled particles. The particles, or nodes, in these diagrams are connected via Mayer f-, f^*- or f^+-bonds. An example of a diagram with two white 1-nodes, one black ρ-node and f-bonds between the nodes is

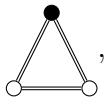
, (2.22)

which, mathematically, represents

$$\int f(1,2)f(2,3)f(1,3)\mathrm{d}3. \tag{2.23}$$

Using these definitions, we can write the formal definition of $C^+(1,2)$ as

$$\begin{aligned} C^+(1,2) =& [\text{All diagrams consisting of two white 1-nodes labelled 1 and 2,} \\ & \text{black } \rho\text{-nodes and } f\text{-bonds, which are free of connecting particles} \\ & \text{and have a continous path of } f^+\text{-bonds between the white 1-nodes}]. \end{aligned} \tag{2.24}$$

Inspecting these connections (or diagrams) is easiest by noting that we can write

$$C^+(\vec{r},\vec{u}_1,\vec{u}_2) = C_2^+(\vec{r},\vec{u}_1,\vec{u}_2) + \rho C_3^+(\vec{r},\vec{u}_1,\vec{u}_2) + \rho^2 C_4^+(\vec{r},\vec{u}_1,\vec{u}_2) + \rho^3 C_5^+(\vec{r},\vec{u}_1,\vec{u}_2) + \cdots, \tag{2.25}$$

where $C_n^+(\vec{r})$ indicates n-body connections, *e.g.*, $C_3^+(\vec{r},\vec{u}_1,\vec{u}_2)$ stands for the connection as defined by definition (2.24), consisting of three particles exclusively. The diagrams in the direct connectedness function are topologically similar to those in the direct correlation function $c(1,2)$, which are given by

$c(1,2) =$ 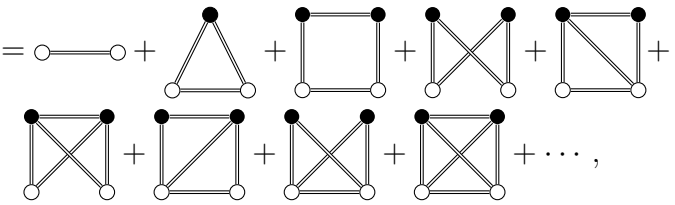 (2.26)

where the double lines represent f-bonds between the particles. The direct connectedness function is now obtained by decomposing the f-bonds in these diagrams into f^+-bonds and f^*-bonds, and selecting only those that have a continuous path of f^+-bonds between the two white particles. This expansion for the first two diagrams shown in Equation (2.26) is given by

$C^+(1,2) =$ 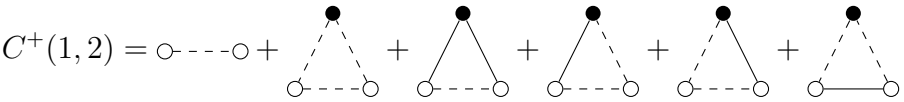 (2.27)

where the dashed lines are f^+-bonds and the solid lines are f^*-bonds.

The diagrammatic expansion of $C^+(1,2)$ allows us to insightfully demonstrate how we can make appropriate approximations on $C^+(1,2)$. Generally, closure relations ignore a set of diagrams in the infinite series of diagrams in Equation (2.27). One of the conceptually simplest closures is by simply truncating the series in Equation (2.27) and only including up to n-body connections. This closure is called the *bare sum approximation* if only the first term is included, or the virial approximation. This closure is often in qualitative agreement with simulation results, and in specific cases also in quantitative agreement. Unfortunately, for most particle shapes, only the first or the first two diagrams can be calculated (analytically), and therefore the sum is necessarily truncated somewhere after the first or second term. This closure is especially useful for strongly anisometric particles in three or more dimensions, where it is remarkably accurate. It is less accurate for particles with a small aspect ratio, or for fewer dimensions, which we illustrate in the next section.

2.4 The virial expansion closure

We have shown in Equation (2.25) that the direct connectedness function $C^+(\vec{r}, \vec{u}_1, \vec{u}_2)$ can be written as a low density expansion, where $C_n^+(\vec{r}, \vec{u}_1, \vec{u}_2)$ contains all diagrams in definition (2.24) consisting of n particles. This means that $C_2^+(\vec{r}, \vec{u}_1, \vec{u}_2)$ corresponds to

$C_2^+(\vec{r}, \vec{u}_1, \vec{u}_2) =$ (2.28)

$C_3^+(\vec{r}, \vec{u}_1, \vec{u}_2)$ corresponds to

$C_3^+(\vec{r}, \vec{u}_1, \vec{u}_2) =$ 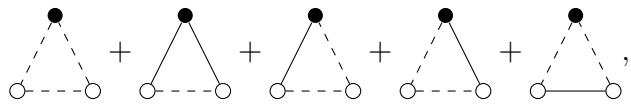 (2.29)

and so on. The virial expansion closure consists of simply truncating this expansion after term n, therefore neglecting all higher order terms. The easiest virial expansion closure is the second virial closure, in which only the first term in expression (2.25) is maintained, while all other terms are ignored.

Equation (2.28) shows that $C_2^+(\vec{r}, \vec{u}_1, \vec{u}_2) = f^+(\vec{r}, \vec{u}_1, \vec{u}_2)$. For ideal particles we have shown that $f^+(\vec{r}, \vec{u}_1, \vec{u}_2) = 1$ if the particles overlap, whereas it is zero if they do not overlap. Hence the

zero wave vector limit of the Fourier transform $\widehat{C}_2^+(0, \vec{u}_1, \vec{u}_2)$ is simply the volume integral over all possible overlap configurations for fixed $\vec{u}_1$ and $\vec{u}_2$, and is given by

$$\widehat{C}_2^+(0, \vec{u}_1, \vec{u}_2) = \hat{f}^+(0, \vec{u}_1, \vec{u}_2) = \lim_{q \to 0} \int \mathrm{d}\vec{r} \exp(i\vec{q} \cdot \vec{r}) f^+(\vec{r}, \vec{u}_1, \vec{u}_2) = V_{\text{contact}}, \tag{2.30}$$

where V_{contact} is the total 'contact volume', *i.e.*, the volume in which the two particles overlap. We are interested in very slender particles, which in two dimensions we model as infinitely thin lines. In two dimensions the contact volume reduces to a contact area A_{contact}. This contact area A_{contact} can be calculated as

$$A_{\text{contact}} = L^2 |\sin \alpha|, \tag{2.31}$$

where $\alpha = \arccos(\vec{u}_1 \cdot \vec{u}_2)$ is the angle between the two lines [12]. Hence, by Equation (2.15) and Equation (2.30) we can obtain the percolation threshold as

$$\rho_p = \frac{1}{L^2} \frac{1}{\langle \langle |\sin \alpha| \rangle_{\vec{u}_1} \rangle_{\vec{u}_2}}. \tag{2.32}$$

The orientational average over α can be carried out explicitly [12], and produces the percolation threshold

$$\rho_p = \frac{\pi}{2L^2}. \tag{2.33}$$

Comparing this predicted density of the percolation threshold with the 'exact' value obtained from Monte Carlo simulations, $\rho_p L^2 = 5.63726(2)$, we notice that it is a factor 3.6 too low [15]. This indicates that the second virial approximation is quantitatively inadequate to describe percolation in two dimensions, even for highly anisotropic particles.

The easiest improvement upon the second virial approximation can be made by including higher terms in the expansion (2.30). The second term in the expansion, $\rho \hat{C}_3^+(0, \vec{u}_1, \vec{u}_2)$, is the highest order term that can be calculated analytically. The percolation threshold obtained by including this term is given by

$$1 = \rho_p L^2 \frac{2}{\pi} - \left(\rho_p L^2\right)^2 \frac{3B_3}{\pi^2}, \tag{2.34}$$

where B_3 is the third virial coefficient given by $B_3 = 0.5142\ldots$ [12, 20]. The extracted percolation threshold is given by $\rho_p L^2 = 2.04 \pm 1.50i$, which is complex and therefore unphysical. The next term in Equation (2.30) can only be calculated numerically, and predicts

$$\rho_p L^2 = 8.87 \pm 0.06, \tag{2.35}$$

which is approximately 1.57 times higher than the value obtained from Monte Carlo studies [21][15]. While larger improvements might be obtained by including even more expansion terms, this is cumbersome. Although cluster-integrals can be obtained numerically to calculate higher order virials, there are significantly more distinct graphs present at each order in the virial expansion. For example, the fourth virial term contains 196 different graphs, whereas in the third virial approximation only five distinct graphs were present, as shown in Equation (2.29). This steep rise in the number of distinct graphs continues and is therefore unlikely to be usable.

The slow convergence of the virial closure in two dimensions is striking, considering its high accuracy in three dimensions. While slow convergence of the connectedness virial series has been observed before, it was in an unrelated model and not directly comparable [22]. For particles with a hard core, a renormalised density approach known as the Parsons-Lee approximation could be used. This approximation is often used in three dimensions, where it interpolates between the Carnahan-Starling and Onsager equation of state. Effectively, it replaces the second virial closure $C^+(1,2) = f^+(1,2)$ by $C^+(1,2) = \Gamma(\eta) f^+(1,2)$, where $\Gamma(\eta)$ is the Parsons-Lee correction factor, dependent on the volume fraction η. In three dimensions, it is given by

$$\Gamma(\eta) = \frac{1 - \frac{3}{4}\eta}{(1-\eta)^2}. \tag{2.36}$$

In two dimensions, this correction can be based on any accurate equation of state, *e.g.*, the one obtained from scaled particle theory. The correction based on the equation of state obtained via scaled particle theory, is given by

$$\Gamma(\eta) = \frac{1}{2}\left(\frac{1}{1-\eta} - \frac{1}{\eta}\ln(1-\eta)\right), \tag{2.37}$$

where η is the volume fraction of the hard-core [23]. Since this expression is only usable for hard-core anisometric particles, for which we have been unable to find Monte Carlo simulation results, it is difficult to assess its accuracy. Hence we propose to use a more sophisticated closure than the virial approximation. The best-known closures in liquid state theory that have been extended to percolation are i) the Percus-Yevick closure, ii) the generalised mean spherical approximation closure, and iii) the hypernetted chain closure.

The Percus-Yevick (PY) closure is the simplest of these closures. It ignores all connections in $C^+(\vec{r}, \vec{u}_1, \vec{u}_2)$ that extend beyond the range of a direct interaction between the two labelled nodes. Hence, all diagrams which do not have a f^+-bond or f^*-bond between the labelled nodes are ignored. Practically, of the diagrams shown in Equation (2.26), we would ignore

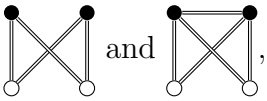 and , (2.38)

but this is done at each level in ρ, hence an infinite, but reduced, set of diagrams is included. The Percus-Yevick closure is often found to be remarkably accurate in liquid state theory, and some analytical results also exist in the context of in percolation theory [24, 25].

The generalised mean spherical approximation (GMSA-closure) is an extension of the Percus-Yevick closure. It is based on a model in which the behaviour of $C^+(\vec{r})$ beyond the range of one f-bond is modelled via analytically solvable Ansätze. The commonly used Ansatz in three dimensions is based on a Yukawa-like tail as

$$C^+(r > d) = K\frac{e^{-zr}}{r}, \tag{2.39}$$

where K and z are tunable parameters and d is the total diameter of the particles. An appropriately tuned closure of this type is analytically solvable for ideal spherical particles in three dimensions and can be remarkably accurate [26], but its extension to anisometric particles is not trivial [27].

The Hypernetted chain closure (HNC) is a closure that can not be solved analytically. It has been extended to percolation theory but has been shown to not predict a divergence in the mean cluster size. Instead, the cluster size converges to a fixed value, hence nullifying the possible use of this closure to describe percolation [28]. We note, for any reader knowledgeable with integral equation theories, that hierarchical theories such as the Born-Green hierarchy have also been extended to percolation but through a different mechanism and are therefore beyond the scope of this report [29, 30].

Since the Percus-Yevick closure is the conceptually and mathematically, simplest closure that goes beyond the virial approximation, we investigate the accuracy and capabilities of the Percus-Yevick closure in the next two sections. The next section focusses on the derivation of the Percus-Yevick closure for percolation and discusses some known results. In chapter 4, we extend it to anisometric particles.

Part I

The Percus-Yevick Closure

Chapter 3

Percus-Yevick theory in Connectedness Percolation

3.1 Introduction

In this chapter, we discuss the Percus-Yevick closure and its applicability to percolation. We start this section by deriving the formal expression for the connectedness Percus-Yevick closure and subsequently discuss some interesting properties of the closure. We briefly indicate how the Percus-Yevick closure can be solved for spherical particles and discuss results from literature. In the next chapter, we extent these methods to percolation for anisometric particles in two dimensions.

3.2 The Percus-Yevick closure

We follow the approach of Coniglio *et al.* [16] in our derivation of the connectedness Percus-Yevick closure. The liquid-state Percus-Yevick closure is given by

$$g_{\mathrm{PY}}(1,2) = e^{-\beta U(1,2)} \left(1 + \rho \int c(1,3) h(3,2) \mathrm{d}3\right), \tag{3.1}$$

where $g_{\mathrm{PY}}(1,2)$ is the radial distribution function (see Equation (2.5)), $U(1,2)$ is the interaction potential between particles 1 and 2, $c(1,3)$ is the direct correlation function between particles 1 and 3, and $h(3,2) = g(3,2) - 1$ the total correlation function [19]. As shown in the previous section, we can split $g_{\mathrm{PY}}(1,2)$ and $e^{-\beta U(1,2)} = f(1,2) + 1$ into a connectedness part and a blocking part. Similarly, we can express $c(1,3)$ as

$$c(1,2) = C^{+}(1,2) + C^{*}(1,2), \tag{3.2}$$

where $C^{+}(1,2)$ is the direct connectedness function defined in Equation (2.27) and $C^{*}(1,2)$ is the direct blocking function. We can similarly split $\rho \int c(1,3)h(3,2)\mathrm{d}3$ as

$$\rho \int c(1,3) h(3,2) \mathrm{d}3 = N^{+}(1,2) + N^{*}(1,2), \tag{3.3}$$

where $N^+(1,2) = \rho \int C^+(1,3)P(3,2)\mathrm{d}3$ is the convolution integral in the connectedness Ornstein-Zernike Equation (2.12) and represents how particles 1 and 2 can be connected via a nodal connection. $N^*(1,2)$ represents all nodal connections in which there is no continuous path of f^+-bonds between particles 1 and 2. Rewriting $e^{-\beta U(1,2)}$ in Equation (3.1) as $f^+(1,2) + f^*(1,2) + 1$, gives

$$g_{\mathrm{PY}}(1,2) = (1 + f(1,2))(1 + N(1,2)) = (1 + f^+(1,2) + f^*(1,2))(1 + N^+(1,2) + N^*(1,2)). \quad (3.4)$$

Next, we can prudently investigate which combination of these diagrams allow for a connection between the two labelled particles 1 and 2, and which ones do not. This allows one to rewrite the previous equation as

$$\begin{aligned} g_{\mathrm{PY}}(1,2) = {} & f^+(1,2) + f^+(1,2)N(1,2) + f^*(1,2)N^+(1,2) + N^+(1,2) \\ & + (\text{diagrams which contain no continuous path of } f^+ \text{ bonds between 1 and 2}). \end{aligned} \quad (3.5)$$

Hence, by use of $g(1,2) = P(1,2) + D(1,2)$ we obtain the expression

$$P_{\mathrm{PY}}(1,2) = f^+(1,2) + f^+(1,2)N(1,2) + f^*(1,2)N^+(1,2) + N^+(1,2), \quad (3.6)$$

which is the Connectedness Percus-Yevick closure in terms of N-diagrams and Mayer functions. Using the (Connectedness) Ornstein-Zernike equation and definition (3.1) gives

$$P_{\mathrm{PY}} = e^{-\beta u^+(1,2)} g_{\mathrm{PY}}(1,2) e^{\beta U(1,2)} + e^{-\beta u^*(1,2)}(P_{\mathrm{PY}}(1,2) - C^+_{PY}(1,2)). \quad (3.7)$$

3.3 Particle models

In this thesis we investigate two different types of models, which are the ideal particle model and the concentric shell, or cherry-pit model. Both particle models are shown in Figure 3.1. In the ideal particle model, the particles are non-interacting and we assume them to be connected if they overlap. In this case, the Percus-Yevick closure simplifies to

$$P(1,2) = 1 \qquad \text{Overlap}, \quad (3.8)$$

$$C^+(1,2) = 0 \qquad \text{No overlap}, \quad (3.9)$$

where the first statement is exact and only the second is an approximation. In the cherry-pit model, the Percus-Yevick closure simplifies to

$$P(1,2) = 0 \qquad \text{Hard core overlap} \quad (3.10)$$

$$P(1,2) = g_{\mathrm{PY}}(1,2) \qquad \text{Connectivity shell overlap} \quad (3.11)$$

$$C^+(1,2) = 0 \qquad \text{No overlap}, \quad (3.12)$$

where $g_{\mathrm{PY}}(1,2)$ is the Percus-Yevick radial distribution function that has to be evaluated explicitly. Since $g_{\mathrm{PY}}(1,2) = 0$ for hard core overlap, we can simplify this expression to

$$P(1,2) = g_{\mathrm{PY}}(1,2) \qquad \text{Overlap of hard cores or connectivity shells} \quad (3.13)$$

$$C^+(1,2) = 0 \qquad \text{No overlap} \quad (3.14)$$

Both the ideal and the cherry-pit model have been solved analytically or numerically for spherical particles in three dimensions. The cherry-pit model can only be solved analytically for a limited range of connectivity shell sizes [25].

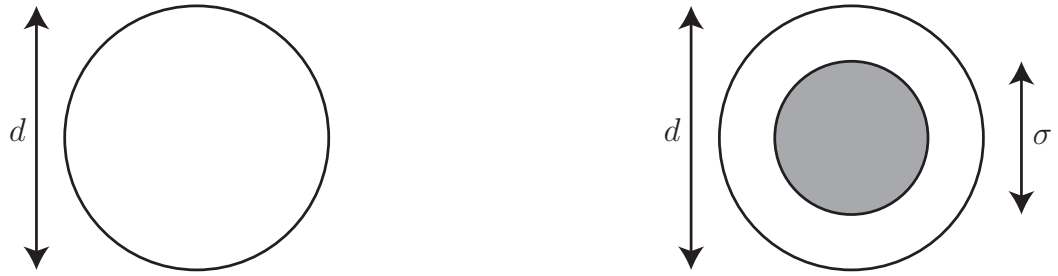

Figure 3.1: (a) The ideal particle model. Particles have a diameter d, and can freely overlap. We define these particles to be connected if they overlap. (b) The cherry-pit particle model. These particles have a hard core of diameter σ, and a shell around this hard core that has a total diameter of d.

3.4 Note on the accuracy of Percus-Yevick

Percus-Yevick is often found to be remarkably accurate for hard core particles at low to medium densities in liquid state theory, but seems to be less accurate in percolation theory [25]. To investigate the origin of this apparent difference in accuracy, DeSimone *et al.* [25] analysed the Percus-Yevick closure diagrammatically. They used a relatively simple argument that indicates why liquid state Percus-Yevick might be more accurate than Percus-Yevick applied to the percolation problem at ρ^2-level. For ideal particles, this is most evident by inspecting the direct correlation function $c(1,2)$

$$c(1,2) = c_{\mathrm{PY}}(1,2) + \quad + \quad + \cdots , \tag{3.15}$$

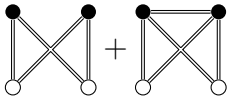

which shows that, at a ρ^2-level, the difference between the Percus-Yevick c_{PY} and the exact c are two diagrams which are of a parallel type [25]. The differences between the two disregarded diagrams is a single f-bond. Since the f-bond has a value of -1 when the particles overlap, the diagrams cancel approximately for most of their domain. For percolation, however, this turns out to not be the case, and we can write the direct connectedness function $C^{+}(1,2)$ as

$$C^{+}(1,2) = C^{+}_{\mathrm{PY}}(1,2) + \quad + \frac{1}{2} \quad + \cdots , \tag{3.16}$$

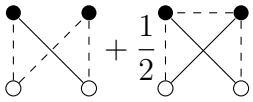

where the dashed lines represent f^{+}-bonds and the solid lines represent f^{*}-bonds. The pre-factor $1/2$ is the weight associated with the diagram. This weight stems from the expansions of f-bonds to f^{+}- and f^{*}-bonds. Due to the pre-factor $1/2$ these two diagrams do not even approximately cancel, explaining why connectedness Percus-Yevick theory is not as accurate as liquid state Percus-Yevick.

3.5 Duality in Percus-Yevick

There exists an interesting analogy between liquid-state Percus-Yevick for hard particles and percolation Percus-Yevick for ideal particles. Comparing the Percus-Yevick percolation closure for

ideal particles, Equations (3.8) and (3.9), to the equivalent closure in liquid state theory for *hard* particles

$$h(1,2) = -1 \qquad \text{Overlap,} \tag{3.17}$$

$$c(1,2) = 0 \qquad \text{No overlap,} \tag{3.18}$$

shows that a deeper connection between correlation and percolation can be made. This can be demonstrated explicitly by replacing $P(1,2)$ and $C^+(1,2)$ in the connectedness Ornstein-Zernike Equation (2.12) and the Percus-Yevick closure with $-h(1,2)$, $-c(1,2)$ and $\rho \to -\rho$, which leaves the functional form of the (connectedness) Ornstein-Zernike equation and the Percus-Yevick closure invariant. Hence, we can directly link the mean cluster size in percolation to the equation of state of the corresponding hard core particles via

$$S = \frac{1}{\beta}\left(\frac{d\rho}{dp_{\mathrm{c}}}\right)_T, \tag{3.19}$$

where p_{c} is the pressure obtained from Percus-Yevick integral equation theory via the compressibility route. This link between the mean cluster size S and the pressure p_c has been used by Torquato and Jiao [31] to study the effect of dimensionality on the percolation threshold. The pressure p_c can be expanded as $\beta\frac{p_{\mathrm{c}}}{\rho} = 1 + B_2\rho + B_3\rho^2 + \ldots$, where B_n are virial coefficients of order n. Equation (3.19) can therefore also be used to directly link Percus-Yevick virial coefficients to Percus-Yevick connectedness virial coefficients via

$$C_n^{+(PY)} = (-1)^{n-2} n B_n^{(PY)} \qquad \text{for } n \geq 2, \tag{3.20}$$

where $C_n^{+(PY)} = \langle\langle C_n^+(0,\vec{u}_1,\vec{u}_2)\rangle_{\vec{u}_1}\rangle_{\vec{u}_2}$. Since Percus-Yevick predicts the exact B_2 and B_3, we also obtain the exact values for C_2^+ and C_3^+. Incorrect values are obtained for $n \geq 4$, which is due to the fact that connectedness Percus-Yevick is only exact up to the first order in the density ρ. Interestingly, the duality between hard particle fluids and percolation of ideal particles is only exactly true for the virial approximation up to the first order in the density, and for Percus-Yevick [31]. Any closure that is correct to a higher order in the density ρ breaks this duality.

3.6 Analytical solutions

The main reason for the popularity of the Percus-Yevick closure is that analytical solutions can be obtained. The Percus-Yevick closure, combined with the connectedness Ornstein-Zernike equation, can be solved via two methods. The first method is based on Laplace transforms, while the second method is based on the Wiener-Hopf factorisation technique, and is often referred to as Baxters method [32–34]. Both methods have advantages and disadvantages, but the Wiener-Hopf factorisation is the only method that has been extended to cherry-pit models and anisometric particles. The common disadvantage of both models is, surprisingly, that they cannot be solved analytically in even dimensions [32, 34]. The reason for this is of geometrical nature, and only recently a semi-analytical solution has been derived for even dimensions [35, 36]. Analytical solutions are

available in odd dimensions $D = 1$ up to $D = 7$, while for $D \geq 9$ numerical methods are necessary [37]. Since the Wiener-Hopf technique is best suited for the problem at hand, we focus on this method only.

We derive the Wiener-Hopf factorisation method in Appendix A and only discuss the main results here. Using the Wiener-Hopf technique, we can reduce the connectedness Ornstein-Zernike equation to a coupled set of integro-differential equations

$$P_k(r) = Q(r) + \lambda \int_0^d \mathrm{d}s Q(s) P_k(|r - s|), \qquad r \geq 0 \tag{3.21}$$

and

$$C_k^+(r) = Q(r) - \lambda \int_r^d \mathrm{d}s Q(s) Q(s - r), \qquad 0 \leq r \leq d. \tag{3.22}$$

where $\lambda = \rho(2\pi)^k$, $D = 2k + 1$ is the dimension, and $Q(r)$ is an auxiliary function [37]. We define $P_k(r)$ and $C_k^+(r)$ recursively as

$$P_k(r) = \int_r^\infty \mathrm{d}s s P_{k-1}(s) \tag{3.23}$$

and

$$C_k^+(r) = \int_r^d \mathrm{d}s s C_{k-1}(s), \tag{3.24}$$

where $P_0(r) = P(r)$ and $C_0^+(r) = C^+(r)$. Equation (3.21) and Equation (3.22) can be solved for $P_0(r)$ and $C^+(r)$ by differentiating k-times with respect to r. Equation (3.21) can be solved for $Q(r)$ if $P_0(r)$ is known in the region $0 \leq r \leq d$, and therefore Equation (3.22) can be solved for $C_0^+(r)$. The mean cluster size S is given by

$$S = \frac{1}{\left(1 - \lambda \int_0^d \mathrm{d}r Q(r)\right)^2}, \tag{3.25}$$

and therefore it is only necessary to solve Equation (3.21).

We know that $P_0(r) = 1$ for $0 \leq r \leq d$ for the ideal particle connectivity criterion, and these equations are trivial to solve. Less trivial is the cherry-pit model, but a solution strategy exists nonetheless. In our effort to demonstrate the peculiarities of the Percus-Yevick closure, we review some known analytical results in the next few sections.

One dimension

First we discuss the ideal particle model in one dimension. Equation (3.21) needs to be solved for $k = 0$, in which case we obtain

$$Q(r) = Q_0 = \frac{1}{1 + \eta}, \qquad 0 \leq r \leq d \tag{3.26}$$

and the mean cluster size is therefore given by

$$S_{\mathrm{PY}} = (1+\eta)^2, \tag{3.27}$$

where $\eta = \rho d$. Here ρ is the number density and d the diameter of a sphere. We immediately extract that the percolation threshold for this model is at $\eta \to \infty$. The one-dimensional percolation model can be exactly solved as

$$S = \frac{2 - e^{-\eta}}{e^{-\eta}}, \tag{3.28}$$

which also predicts a percolation threshold at $\eta \to \infty$ [38]. We find that the Percus-Yevick results are exact up to the second order in the density, in agreement with the diagrammatic definition. Interestingly, while the Percus-Yevick closure in one dimension produces the exact equation of state in liquid state theory, it does not yield the exact mean cluster size in percolation theory [37].

Next, we focus our attention on the cherry-pit model. In this model, the radial distribution function $g_{\mathrm{PY}}(r)$ must be calculated *a priori*, since $P(r) = g_{\mathrm{PY}}(r)$ within the connectivity shell. Fortunately, $g_{\mathrm{PY}}(r)$ is known analytically [39]. The derivation for the cherry-pit model is slightly more involved, and the resulting equations can only be solved over a limited range of σ/d. For a hard core diameter of σ and total particle (*i.e.*, hard core plus connectivity shell) diameter d, we can solve the Percus-Yevick closure in the range $1/2 \leq \sigma/d \leq 1$. This derivation has been applied to a three-dimensional model by DeSimone *et al.* [25], and our derivation for the one-dimensional case is discussed in Appendix E.

The mean cluster size S for the range $\frac{1}{2} \leq \sigma/d \leq 1$ is given by

$$S_{\mathrm{PY}} = \frac{(\eta + \sigma + 2\eta\sigma)^2}{(1-\eta)^2\sigma^2}, \tag{3.29}$$

where η is the volume fraction of the hard core, σ is the diameter of the hard core and we have set $d = 1$ for convenience. Equation (3.29) shows that the mean cluster size diverges at the close-packing packing fraction $\eta_{\mathrm{cp}} = 1$ for all $1/2 \leq \sigma \leq 1$ with the critical exponent $\gamma = 2$. The exact result for the mean cluster size S is known due to Drory [40]

$$S = 2\exp\left[\frac{\rho(1-\sigma)}{1-\rho\sigma}\right] - 1, \tag{3.30}$$

and also diverges at the close packing fraction.

While these results suggest that Percus-Yevick theory provides acceptable results in one dimension, the percolation threshold is trivial for both models and the agreement is not necessarily indicative of the accuracy of Percus-Yevick theory. Secondly, it turns out that the cherry-pit model needs to be treated with care. By inspecting Equation (3.21) just inside and just outside of the connectivity shell, it can be shown that the pair connectedness function $P(1,2)$ is negatively valued just outside the connectivity shell. Since the pair connectedness function is related to the probability of finding two particles connected, it is positively valued by definition. While similar problems are

known to occur in liquid state Percus-Yevick theory, it has not been reported for Percus-Yevick in percolation. It has recently been discussed that this inconsistency might actually indicate that Percus-Yevick theory breaks down completely above the density where $g_{\mathrm{PY}}(1,2)$ develops a region that is negatively valued [41]. Therefore we argue that, while predicting the correct percolation threshold, Percus-Yevick theory is not well-suited to describe percolation in one dimension.

Three dimensions

Ideal particles in three dimensions can be treated in a similar manner as the one-dimensional case. The mean cluster size for this model is given by

$$S_{\mathrm{PY}} = \frac{(1+\eta)^4}{(2\eta-1)^2}, \tag{3.31}$$

where $\eta = \rho\pi/6d^3$. We immediately see that the percolation threshold is reached for $\eta_c = 1/2$ and the critical exponent of the mean cluster size $\gamma = 2$. This estimated percolation threshold is approximately 46% higher than Monte Carlo results for the same model [31]. The physical dimensions of a cluster can be obtained by using a small wave vector expansion of the mean cluster size and writing it in Lorentzian form [16], *i.e.*, by expanding the wave vector dependent mean cluster size

$$S(\vec{q}) = \frac{1}{1-\rho C^{+}(\vec{q})}, \tag{3.32}$$

as

$$S(\vec{q}) = \frac{S}{1+\zeta^2|\vec{q}|^2}, \tag{3.33}$$

where ζ is the correlation length. This length contains information about the spatial cluster dimensions. The correlation length can be written as

$$\zeta/d = \sqrt{\frac{\eta(16+\eta(11+4\eta))}{20(1+\eta)^4}}\sqrt{S}, \tag{3.34}$$

which diverges at the percolation threshold with the critical exponent $\nu = 1$. Hence, from hyper-scaling relations, we can deduce that the fractal dimension is $d_{\mathrm{f}} = \frac{5}{2}$ [38].

The cherry-pit particle model has been solved analytically by DeSimone *et al.* [25] for the same connectivity range as we presented for the one-dimensional case. The mean cluster size S can be calculated analytically, but its expression is not insightful. In Figure 3.2, we plot the percolation threshold obtained via Percus-Yevick theory (blue line) and the percolation threshold obtained via Monte Carlo simulations (dots) as a function of the connectivity shell thickness σ/d [25]. We observe that, qualitatively, Percus-Yevick predicts the correct dependence of the percolation threshold on σ/d, while it is quantitatively inaccurate. It can be shown that the critical exponent for the mean cluster size is $\gamma = 2$ and the critical exponent for the correlation length $\nu = 1$. Hence its critical behaviour is similar to that of ideal particles in three dimensions. We do note that, in contrast to the one-dimensional cherry-pit model, we do not find the Percus-Yevick closure to be unphysical, as $P(1,2)$ is positively valued everywhere below the percolation threshold.

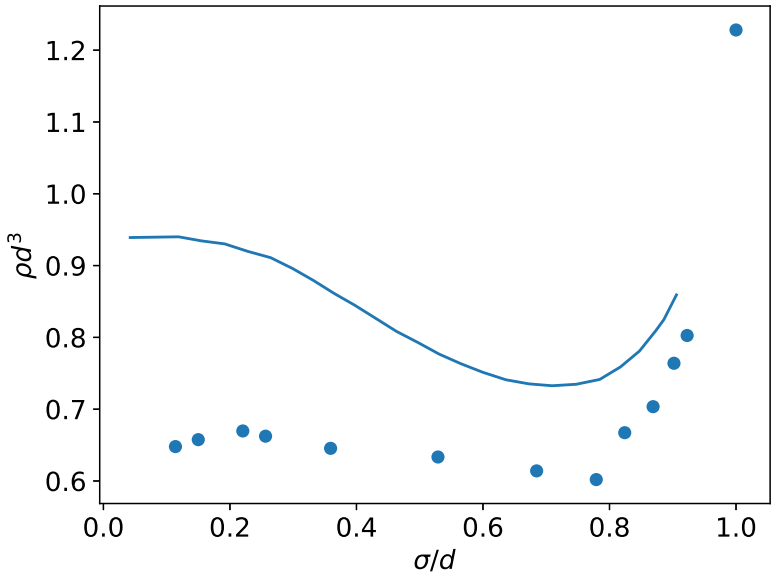

Figure 3.2: The reduced density ρd^3 as a function of the hard core fraction σ/d. The blue line indicates the percolation threshold for the cherry-pit model, obtained via the Percus-Yevick closure. The dots are Monte Carlo results for the same model. Graph reproduced from [25].

3.7 Two dimensions

These results indicate that Percus-Yevick theory is an interesting candidate to describe percolation quantitatively. The presented results are remarkably better than those obtained by the second virial approximation. While Percus-Yevick is often used for its simplicity and the existence of analytical results, this is only true for odd dimensions. In two dimensions, both the Laplace transform solution strategy and the Wiener-Hopf factorisation method cannot be used to derive analytical solutions due to geometrical reasons[1]. A method that uses the Wiener-Hopf factorisation method to rewrite the Ornstein-Zernike in a similarly coupled set of integro-differential equations has recently been derived, but does not allow for an analytical solution either [35].

Several methods have been devised to cope with this inability to analytically describe two-dimensional models within the Percus-Yevick approximation. One prominent method is based on an interpolation between a one-dimensional and a three-dimensional fluid to derive an accurate (but approximate) representation of the hard-disk correlation function in the PY approximation. These interpolations can be simply mapped onto percolation due to the duality between liquid state theory and percolation theory in the Percus-Yevick approximation [43–45]. The mapping by Baus and Colot [44] has been extended to percolation by Torquato and Jiao [31] and does not predict a percolation threshold, which is also true for the methods developed by Leutheusser [43] and Rosenfeld [45]. The semi-analytical method by Adda-Bedia *et al.* [35] could be extended to percolation.

[1]The Laplace transform technique necessarily relies on a decomposition of the convolution in the Ornstein-Zernike equation via a bipolar coordinate transform. This transform is, however, singular in two dimensions [42]. The Wiener-Hopf factorisation method is more technical in nature and is discussed in Appendix B.

While in three dimensions, the Wiener-Hopf factorisation method reduces the Ornstein-Zernike equation to two integral equations that extend only over the range of the connection, this is not true in two dimensions. One of the equations still extends over an infinite domain and it does therefore not reduce the complexity of (numerically) solving the connectedness Ornstein-Zernike equation. Using their factorisation method, the percolation threshold can be investigated via the Percus-Yevick connectedness virial coefficients, which are trivially extracted. Unfortunately, we have found the convergence of this connectedness virial series to be too slow to be of practical use.

Hence, the only method available is a direct numerical evaluation of the Percus-Yevick equations. To our knowledge no reported results exist for the Percus-Yevick closure in percolation of two-dimensional models. The numerical methods we use are discussed in Appendix F.

In Figure 3.3, we plot the mean cluster size of an ideal disk model as a function of the scaled density ρd^2. We have indicated the percolation threshold obtained from Monte Carlo simulations by Mertens and Moore [15] in orange, and the second virial approximation threshold in blue. We observe that the cluster growth is almost monotonic, only slightly deviating from an exponential growth for $\rho d^2 < 1$. At $\rho d^2 \approx 6$ we approach the edge of the region of convergence of our method as indicated by the noise present in the plot. We find no indication for the presence of a percolation threshold in Percus-Yevick theory in two dimensions.

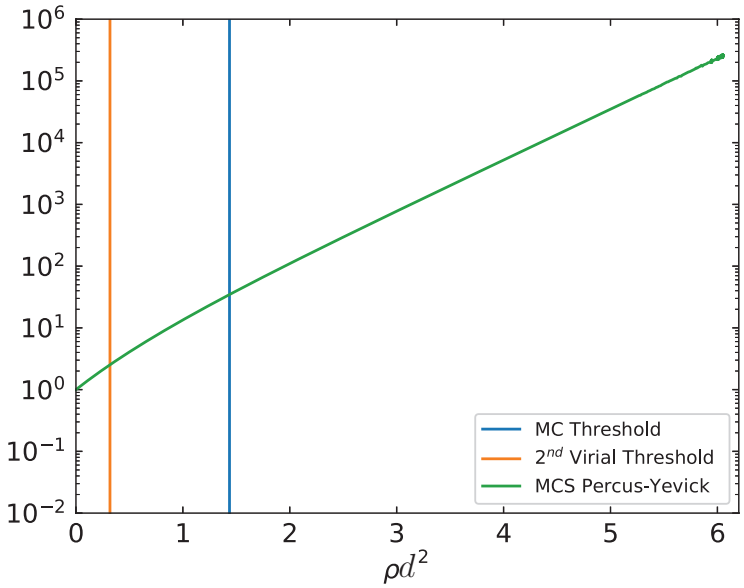

Figure 3.3: The mean cluster size S as a function of the scaled density ρd^2. The predicted threshold via both second virial approximation and Monte Carlo simulations are indicated in orange and blue, respectively. We observe a uniform exponential behaviour for all densities.

The widely different behaviour between $D = 1$ (no percolation threshold at finite densities) on one side, and $D = 3$ (percolation threshold at finite density) on the other side indicates that somewhere between $D = 1$ and $D = 3$ the connectedness Percus-Yevick closure changes its prediction. Yet, due to the limited numerical accuracy we cannot be certain that the change occurs at $D = 2$

exactly. It is possible to inspect Percus-Yevick theory at non-integer dimensions in order to gain insight if there is indeed some limiting behaviour for $D = 2$ [46]. In Figure 3.4a, we plot the mean cluster size for various fractional dimensions between $D = 1$ and $D = 3$ as a function of the D-dimensional volume fraction, defined by $\eta = 2\pi^{D/2}\rho/(D\Gamma(D/2))$, where Γ is the gamma-function [46]. In Figure 3.4b we plot the derivative of the *logarithm* of the mean cluster size with respect to the volume fraction η. This derivative indicates whether the growth is sub- or super-exponential. We obtain the analytically known results for $D = 1$ and $D = 3$ with a divergence at $\eta_c = \infty$ and $\eta_c = 1/2$, respectively. Figure 3.4b clearly indicates that for $D < 2$ we obtain sub-exponential growth, while we have super-exponential growth for $D > 2$. While this condition is in no way a measure to locate the percolation threshold, it does highlight that there is indeed a change of behaviour around $D = 2$. For $D > 2.5$ we have established the presence of a percolation threshold numerically, where the expected scaling of $S \sim |\rho - \rho_p|^{-\gamma}$ near the threshold is present. For $D < 2$ we do not obtain comparable results. This observed change of behaviour around $D = 2$ might indicate that $D = 2$ is the upper dimension for which Percus-Yevick does not predict a presence of the percolation threshold at a finite density for ideal particles.

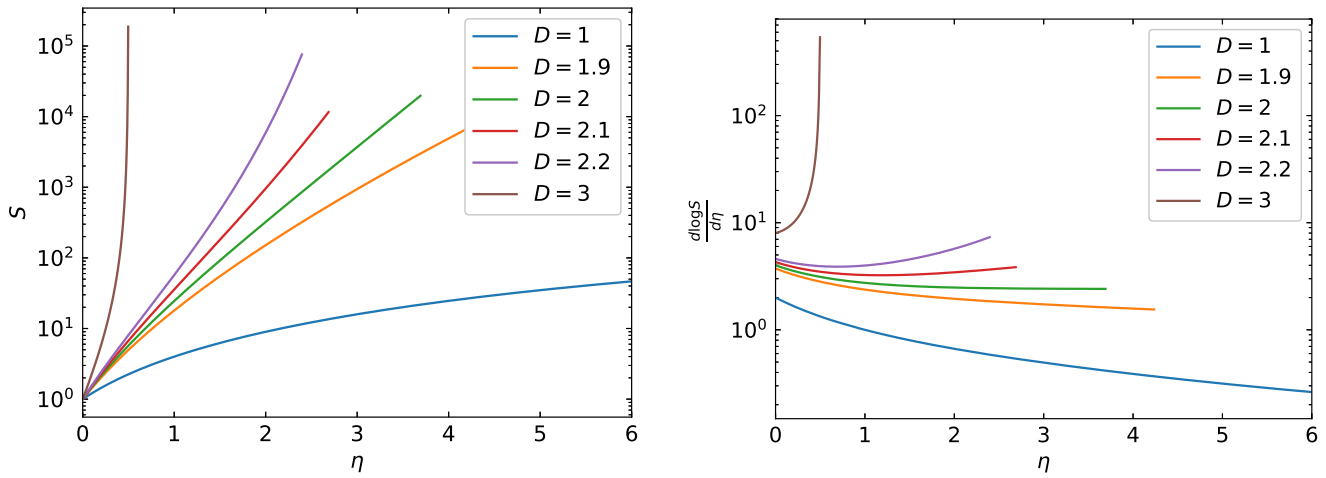

(a) (b)

Figure 3.4: (a) The mean cluster size for $D = 1$ up to $D = 3$ for various non-integer dimensions as function of the volume fraction η. (b) The derivative of $\log S$ with respect to the volume fraction η for various densities.

The cherry-pit model

The cherry-pit model in two dimensions has been investigated via Monte Carlo studies by Lee and Torquato [47, 48]. We have used a direct numerical evaluation of the Percus-Yevick equations and find that we are unable to determine the percolation transition for a large range of parameters, as we can not iterate to densities close enough to the percolation threshold to estimate its presence. While we do observe diverging behaviour in the mean cluster size S, we do not obtain the expected

universality, *i.e.*, the critical exponent is expected to be independent of σ/d, yet varies significantly in our numerical study. Secondly, we again observe that Percus-Yevick theory yields unphysical results for the cherry-pit model as indicated in Figure 3.5, where we observe a small region just outside of $r/d = 1$ in which $P_{\mathrm{PY}}(r)$ is negative. While this occurred at all $\eta \neq 0$ in the one-dimensional case, in two dimensions it only happens in a limited range of volume fractions η.

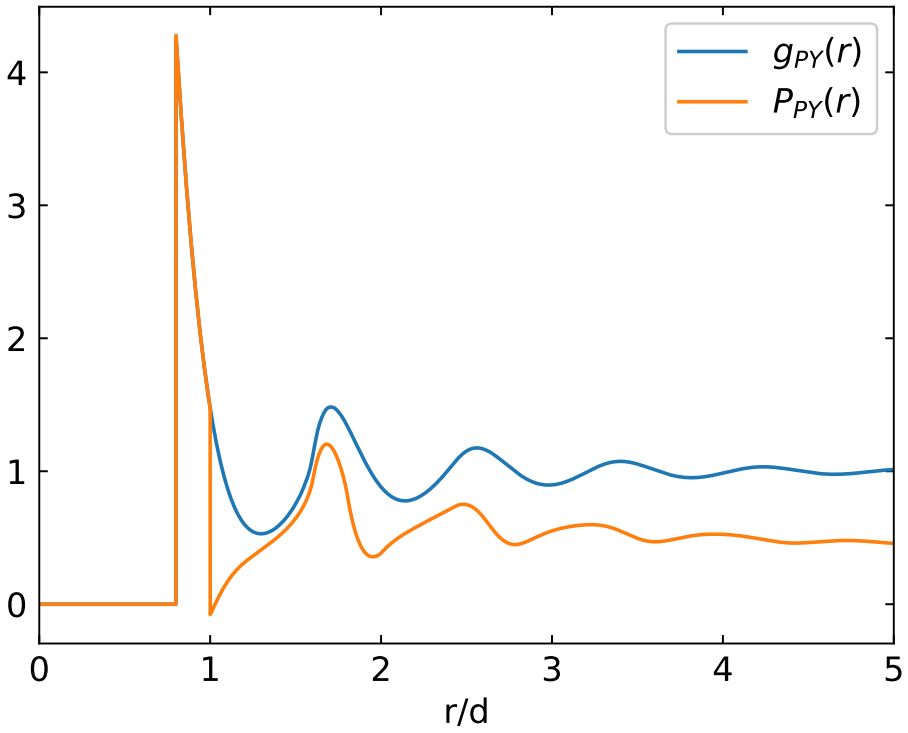

Figure 3.5: The pair connectedness function $P_{\mathrm{PY}}(r)$ and the radial distribution function $g_{\mathrm{PY}}(r)$ as a function of the distance r/d. Here $\rho d^2 = 1.21$ and $\sigma = 0.8d$. The pair connectedness function is negatively-valued around $r/d = 1$, which is not physical.

The two presented models for isotropic particles in two dimensions indicate that the Percus-Yevick closure for percolation is not an accurate closure in two dimensions, leaving us unable to find or even estimate the location of the percolation threshold. For the densities we are able to probe, we find that the relative error of Percus-Yevick theory to Monte Carlo results is larger than that of the second virial approximation, and therefore the added complexity due to the more sophisticated closure does not pay off. This holds for both the ideal particle model and the cherry-pit model. Secondly, the breakdown of Percus-Yevick theory for the cherry-pit model, with partly negative values for $P_{\mathrm{PY}}(r)$ just outside the hard core, indicates that Percus-Yevick is not well-suited to describe percolation in two dimensions.

While these results do not give much hope for the accuracy of the Percus-Yevick closure for anisometric particles, it is not necessarily problematic. The additional orientational degrees of

freedom present in a model with anisometric particles might add enough novelty that it could still be used to describe percolation in two dimensions for anisotropic nanofillers. This we address in the next chapter.

Chapter 4

Extension to anisometric particles

4.1 Introduction

In this chapter we extend the Percus-Yevick closure to anisometric particles of arbitrary shape. The two main methods to extend the (liquid state) Percus-Yevick closure to anisometric particles are the Interaction Site Model (ISM) and the basis-function expansion [49][50].

ISM

C-ISM or Connectedness-Interaction Site Model-based methods are based on the theory by Chandler and Anderson [49]. In this model it is assumed that each molecule is composed of m rigidly connected spheres, which are allowed to overlap within a molecule. Using this simplification, the pair connectedness function can be rewritten into a site-site connectedness function, which is the pair connectedness function of pairs of spheres on each molecule. This site-site connectedness function is linked to the pair connectedness function, but does constitute an irretrievable loss of information, since $P(1,2)$ cannot be reconstructed from the site-site connectedness function.

Using this formalism, it is possible to derive an Ornstein-Zernike-like relation which has to be supplied with a closure. The Percus-Yevick closure is one of the closures that has been extended to this formalism and has indicated qualitative agreement [51][52]. The C-ISM formalism has some important defects, however. First of all, the C-ISM equations are by definition pre-averaged. Hence angular correlations are not easily extracted. Secondly, the method can show an unphysical dependence on the presence of 'auxiliary' sites, which are sites that label a point in a molecule, but do not contribute to the intermolecular connectivity. Thirdly, some angular-dependent quantities are not always properly represented and this appears to be independent of the used closure [19]. The reason for this can be found mainly in the fact that ISM is not 'diagrammatically proper'. This means that the diagrammatic expansion of the ISM-Ornstein-Zernike includes diagrams that are not present in the normal Ornstein-Zernike equation. Hence, C-ISM is, by construction, not (fully) correct and caution should be taken when using these equations.

An extension to ISM has been made by Chandler, Sibley and Ladanyi (CSL) that corrects these deficiencies at the cost of increased complexity [53]. This method has been extended to connectedness percolation by Lupkowski and Monson [54]. In the low-density limit, a comparison

of the CSL and C-ISM methods with respect to an direct numerical evaluation of the involved diagrams, shows that the CSL method is significantly more accurate [54]. A comparison with Monte Carlo results has not been made, but it is likely that the CSL formalism is more accurate than the C-ISM formalism [55]. Secondly, it is possible to construct a ISM-like theory that still contains all orientational information. This can be done by not averaging over both particles, but only over one particle [56, 57]. Orientational information is still present and can be used to fully reconstruct the pair correlation functions. Whether the larger computational cost outweighs the inclusion of orientational information is questionable.

Basis-functions

The second method is based on an expansion of all functions in a basis with the appropriate symmetry, *i.e.*, a basis that is invariant under a rotation of the entire system. This method has been used by Blum [50] in liquid state theory, and extends Percus-Yevick to particles with non-spherical interactions. For an isotropic model, the commonly used basis is the rotational invariant basis, which in three dimensions is formed by spherical harmonics and in two dimensions by circular harmonics. While this method retains all orientational information and is diagrammatically proper, it rests upon the assumption that the expansion is convergent and that we can truncate it after a small number of included invariants without much loss of information. Unfortunately, this basis-set expansion has often been found to be only slowly convergent, so a large set of basis functions is necessary.

While both methods have their advantages and disadvantages, we extend connectedness Percus-Yevick closure via the basis-function expansion method, since it is diagrammatically proper and allows us to inspect all angular properties.

4.2 Percus-Yevick for anisometric nanofillers

We follow the approach of Ferreira *et al.* [58] and extend it to percolation. We expand both the pair connectedness function $P(\vec{r}, \vec{u}, \vec{u}')$ and the direct connectedness function $C^+(\vec{r}, \vec{u}, \vec{u}')$ in the rotational invariant basis

$$P(1,2) = \sum_{m,n=-\infty}^{\infty} P^{mn}(\vec{r})\Psi^{mn}(\theta_1, \theta_2) \tag{4.1}$$

where $P^{mn}(\vec{r})$ are the projections of $P(\vec{r}, \vec{u}, \vec{u}')$ on the basis and $\Psi^{mn}(\theta_1, \theta_2)$ are the rotational invariants. A similar expression is obtained for the direct connectedness function $C^+(\vec{r}, \vec{u}, \vec{u}')$. The rotational invariant basis-functions $\Psi^{mn}(\theta_1, \theta_2)$ are dependent on the reference frame. Here, we use the intermolecular frame, which we illustrate in Figure 4.1. In this frame, the rotational invariants are given by

$$\Psi^{mn}(\theta_1, \theta_2) = \exp i(m\theta_1 + n\theta_2), \tag{4.2}$$

where θ_1 is the angle between the distance vector $\vec{r}$ and the major axis of particle 1, and θ_2 is the angle between the distance vector $\vec{r}$ and the major axis of particle 2. These invariants are

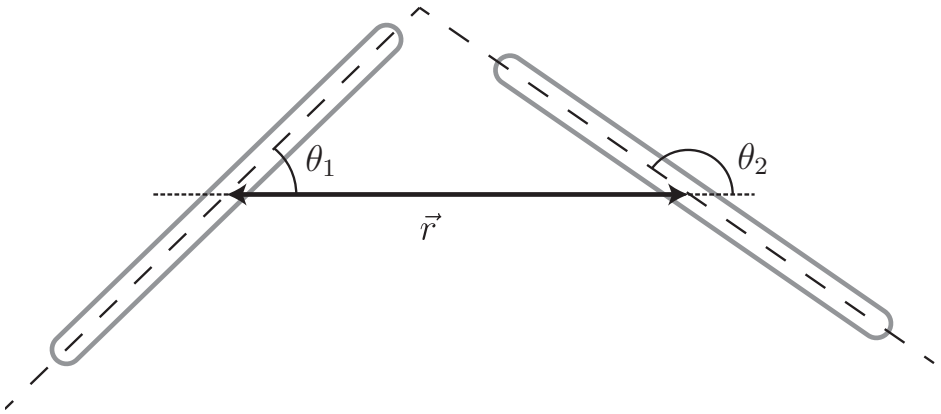

Figure 4.1: Illustration of the intermolecular frame where both particles are disco-rectangles of equal aspect ratio. In this illustration, $\vec{r}$ is the distance vector between the centres of mass of both particles, θ_1 is the angle between the major axis of particle 1 and the centre-to-centre distance vector, and θ_2 is the angle between the major axis of particle 2 and the centre-to-centre distance vector.

orthogonal, and therefore the projections $P^{mn}(\vec{r})$ are given by

$$P^{mn}(\vec{r}) = \frac{1}{4\pi^2}\int_0^{2\pi} \mathrm{d}\theta_1 \int_0^{2\pi} \mathrm{d}\theta_2 P(1,2)\Psi^{mn}(\theta_1,\theta_2). \tag{4.3}$$

We can reduce the set of basis functions by noting that the connectedness functions P and C^+ are real functions, and by using the top-down symmetry of the interactions, which reduces the set by

$$P^{mn} = P^{-m-n} = P^{nm} = P^{-n-m}. \tag{4.4}$$

Additionally, the inversion symmetry of the particles implies that $P(\vec{r},\theta_1,\theta_2) = P(\vec{r},\pi-\theta_1,\pi-\theta_2)$ and therefore both m and n must be even, reducing the total number of independent basis-functions significantly.

Next, we define the Fourier transforms of $P(1,2)$ and $C^+(1,2)$ as

$$\widehat{P}(\vec{q},\theta_{1q},\theta_{2q}) = \int \mathrm{d}\vec{r} e^{-i\vec{q}\cdot\vec{r}} P(\vec{r},\theta_1,\theta_2), \tag{4.5}$$

where θ_{1q} is the angle between the symmetry axis of molecule 1 and the direction of the vector $\vec{q}$, with a similar definition for θ_{2q}. The corresponding projections of $P(1,2)$ in Fourier space are related to the real space coefficients through the Fourier-Bessel transform

$$\widehat{P}^{mn}(q) = 2\pi i^{m+n} \int \mathrm{d}r r P^{mn}(r) J_{m+n}(qr), \tag{4.6}$$

where J_N is a Bessel function of order N defined by

$$J_N(x) = \frac{i^{-N}}{\pi}\int_0^{\pi} e^{ix\cos\theta}\cos N\theta \mathrm{d}\theta. \tag{4.7}$$

Hence, the expansion in Fourier space reads

$$\widehat{P}(q,\theta_{1k},\theta_{2k}) = \sum_{m,n} \widehat{P}^{mn}(q)\Psi^{mn}(\theta_{1k},\theta_{2k}). \tag{4.8}$$

Using these expressions, it can be shown that the Fourier transform of the orientation-dependent Ornstein-Zernike Equation (2.13) for an isotropic orientation distribution is conveniently rewritten as

$$\widehat{P}^{mn}(q) = \widehat{C}^{mn}(q) + \rho \sum_{l} \widehat{P}^{ml}(q)\widehat{C}^{-ln}(q), \tag{4.9}$$

where we have abbreviated C^+ to C for notational convenience. This 'molecular' connectedness Ornstein-Zernike equation is independent of the basis $\Psi(\theta_{1q},\theta_{2q})$, but couples an infinite number of the projections $\widehat{P}^{mn}$ and $\widehat{C}^{mn}$ in Fourier space. For this formalism to be usable, we cut off the expansions, so that $|m|,|n| < n_{\max}$, where we assume that $n_{\max}$ is large enough that the series has converged. The total number of independent projections is given by $\frac{1}{4}(n_{\max}+2)^2$. It has been found in liquid state theory, that the convergence of the expansion is low for highly anisometric particles. Hence, as line segments are the most anisometric particles in two dimensions, we expect that a large expansion is necessary.

The mean cluster size S is obtained from $P(1,2)$ as

$$S = 1 + \rho \lim_{q\to 0} \sum_{m,n=-\infty}^{\infty} \widehat{P}^{mn}(q)\langle\langle\Psi^{mn}(\theta_1,\theta_2)\rangle_{\theta_1}\rangle_{\theta_2}, \tag{4.10}$$

which, in the isotropic case, simplifies to

$$S = 1 + \rho \lim_{q\to 0} \widehat{P}^{00}(q) = \lim_{q\to 0} \frac{1}{1-\rho\widehat{C}^{00}(q)}. \tag{4.11}$$

Now that we have reduced the Ornstein-Zernike equation and the mean cluster size to a tractable form, we move on to the Percus-Yevick closure. In this formalism, we can essentially take two routes. The first route is to apply the Wiener-Hopf factorisation technique to the current problem. This method has been applied in liquid state theory in three dimensions by Blum [50, 59] and Carlevaro *et al.* [27] and might also be possible in two dimensions. However, since the Wiener-Hopf technique in two dimensions does not reduce the range of the equations involved, and was not useful for percolation for ideal disk particles, we believe that, while likely applicable and interesting for liquid state theory, it is not useful for two-dimensional percolation problems. Therefore we opt to use a second route, which is to reduce the Percus-Yevick closure (3.7) to a numerically convenient form.

The Percus-Yevick closure in rotational invariants

To reduce the Percus-Yevick closure to a numerically convenient form, we again follow the approach of Ferreira *et al.* [58]. We start by writing the Percus-Yevick closure (3.7) as

$$C^+(1,2) = g_{\mathrm{PY}}(1,2) - Z(1,2) \qquad \text{Overlap of hard cores or connectivity shells,} \tag{4.12}$$

$$C^+(1,2) = 0 \qquad \text{No overlap,} \tag{4.13}$$

where $Z(1,2) = P(1,2) - C^+(1,2)$. This form is general for both the ideal particle model (for which $g_{\mathrm{PY}}(1,2) = 1$) and the cherry-pit model. Next, we expand $C^+(1,2)$ using Equation (4.3), and split the integrals into two orientational regions, one region where molecules overlap (either hard core or connectivity shell) (OV) and one region where they do not overlap (NOV). Since we know that $C^+(1,2) = 0$ for the NOV region, this integral evaluates to zero. Hence, the projections of $C^+(1,2)$ can be obtained from the Percus-Yevick closure as

$$C^{mn}(r) = \frac{1}{(2\pi)^2} \int_{OV} \mathrm{d}\theta_1 \mathrm{d}\theta_2 \left[g_{\mathrm{PY}}(1,2) - Z(1,2) \right] \Psi^{mn}(1,2). \tag{4.14}$$

By expanding $Z(1,2)$ and $g_{\mathrm{PY}}(1,2)$ in rotational invariants, we can simplify the integrand as

$$C^{mn}(r) = \sum_{m'n'} \left[g_{\mathrm{PY}}^{m'n'}(r) - Z^{m'n'}(r) \right] A_{n-n'}^{m-m'}(r), \tag{4.15}$$

where $g_{\mathrm{PY}}^{m'n'}(r)$ are the projections of $g_{\mathrm{PY}}(r)$. For ideal particles we obtain $g_{\mathrm{PY}}^{m'n'}(r) = \delta_{m'0}\delta_{n'0}$, with $\delta_{m'0}$ the Kronecker delta. For non-ideal particles, the projections $g_{\mathrm{PY}}^{m'n'}(r)$ have to be calculated separately. The auxiliary function

$$A_{n-n'}^{m-m'}(r) = \frac{1}{(2\pi)^2} \int_{OV} \mathrm{d}\theta_1 \mathrm{d}\theta_2 \Psi^{mn}(1,2) \Psi^{m'n'}(1,2) \tag{4.16}$$

defines the so-called overlap coefficients that contain all orientational information. It can be shown that these overlap coefficients are directly linked to the connectedness Mayer f^+-function via

$$f^+(\vec{r}, \theta_1, \theta_2) = \sum_{m,n=-\infty}^{\infty} A_n^m(r) \exp(im\theta_1) \exp(in\theta_2). \tag{4.17}$$

Due to symmetry, we can reduce the number of independent components of $A_{n-n'}^{m-m'}(r)$ by

$$A_{n-n'}^{m-m'} = A_{m-m'}^{n-n'} = A_{n'-n}^{m'-m} = A_{m'-m}^{n'-n}. \tag{4.18}$$

From the orthogonality in $\Psi(1,2)$ and the definition of the overlap coefficients, we obtain

$$A_{n-n'}^{m-m'}(r) = \delta_{(m-m')0}\delta_{(n-n')0}, \tag{4.19}$$

$$C^{mn}(r) = g_{\mathrm{PY}}^{mn}(r) - Z^{mn}(r), \tag{4.20}$$

if the particles overlap (either hard core or connectivity shell) for all orientations, and

$$A_{n-n'}^{m-m'}(r) = 0, \tag{4.21}$$

$$C^{mn}(r) = 0, \tag{4.22}$$

if the connectivity criterion is not met for any orientation. The overlap coefficients are only dependent on the particle shape and can therefore be predetermined, which significantly reduces the computational effort in solving the Percus-Yevick equations. They can usually only be calculated with numerical methods.

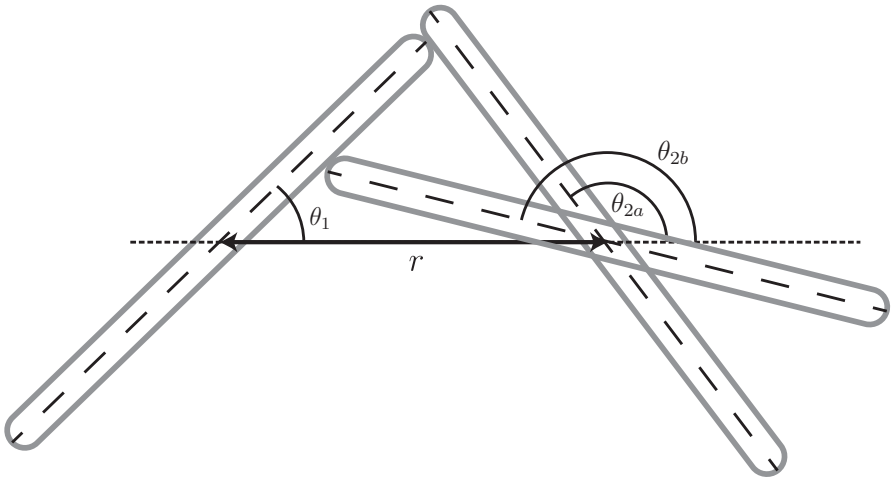

Figure 4.2: An example of the contact angles for two disco-rectangle particles, where θ_{2a} and θ_{2b} are the contact angles of the second particle. These angles depend on both θ_1 and r.

Overlap Coefficients

The formal expression for the overlap coefficients (4.16) can be rewritten as

$$A_N^M(r) = \frac{4}{\pi^2}\int_0^{\pi/2} \mathrm{d}\theta_1 \cos\left[M\theta_1 + \frac{N}{2}(\theta_{2a}+\theta_{2b})\right]\frac{\sin\left[\frac{N}{2}(\theta_{2a}-\theta_{2b})\right]}{N}, \tag{4.23}$$

where the contact angles for particle 2, $0 \leq \theta_{2a}, \theta_{2b} \leq \pi$ depend on both r and θ_1, as illustrated in Figure 4.2 [58]. These angles can, for line segments, be determined analytically as

$$\theta_{2a}(x,\theta_1) = \begin{cases} \arccos\frac{\cos\theta_1 - 2x}{\sqrt{1+4x^2-4x\cos\theta_1}}, & \text{for } \theta_1 \leq \arccos x, \\ \theta_1 + \arcsin 2x\sin\theta_1, & \text{for } \theta_1 > \arccos x, \end{cases} \tag{4.24}$$

$$\theta_{2b}(x,\theta_1) = \pi + \theta_1 - \arcsin 2x\sin\theta_1. \tag{4.25}$$

where $x = r/L$ is the centre-to-centre distance normalised by the length of a line segment, see Appendix D. In Figure 4.3, we show examples of overlap coefficients A_N^M for several values for M and N. We observe that the zeroth order term is the dominant term and the magnitude of the consecutive terms decrease with increasing M and N. The kink in the overlap coefficients at $r/L = 1/2$ is easily explained. For $r/L < 1/2$ overlap configurations exist for all θ_1. For $r/L > 1/2$ this is not the case, since particle 1 can be oriented in such a manner that the particles do not overlap for any value of θ_2. This transition from always overlapping for all θ_1 to overlapping only for $\theta_1 < \theta_{1t}$ is very sharp, causing the presence of the kink at $r/L = 1/2$.

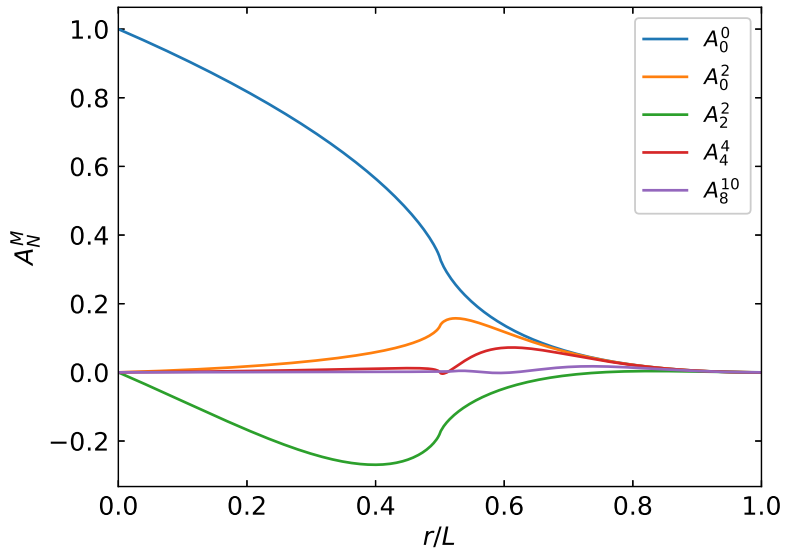

Figure 4.3: Examples of the overlap coefficients A_N^M for various values for M and N. The kink present at $r/L = 0.5$ is due to the sharp change in overlap probability, see the main text.

4.3 Ideal anisotropic nanofillers

Now that we have derived a method to describe percolation in a two-dimensional model with anisometric nanofillers within the Percus-Yevick approximation, we apply it to an ideal fluid of infinitely thin sticks. We solve the Equations (4.9) and (4.15) with the same numerical iterative solver that we have used for the two-dimensional disk fluid in section 3.7. We refer to Appendix F for details on the numerical method. Due to the projection-coupling in the Ornstein-Zernike Equation (4.9), more care needs to be taken to ensure convergence. The size of the necessary basis-set expansion is dependent on the information we want to extract. For the determination of the percolation threshold, we only demand that the mean cluster size (4.11) is converging for increasing $n_{\max}$. For the rotational invariant expansion to converge, we demand that the full orientational distribution is in agreement with Monte Carlo simulations, at least at low densities where Percus-Yevick theory is accurate.

In Figure 4.4a, we plot the mean cluster size S for various $n_{\max}$ over a limited range of the reduced density ρL^2. While we observe some variation in the actual value of the mean cluster size S, the functional behaviour for $\rho L^2 > 1$ is independent of the size of the rotational invariant expansion. Especially the zeroth order approximation significantly deviates from the other expansion sizes. We quantify this deviation in the mean cluster size as a function of $n_{\max}$ by comparing the relative deviation with respect to the largest cutoff value we have used, $n_{\max} = 20$, in Figure 4.4b. We observe that the deviation is negligible for $\rho L^2 < 1$. For $\rho L^2 > 1$, the error is especially significant for the zeroth order approximation (or the pre-averaged approximation), but for $n_{\max} > 2$ is of the order of one percent. Hence a small basis set can be used to estimate the presence of the percolation threshold (if any), and the error in the estimate can be reduced by increasing the basis-set. In

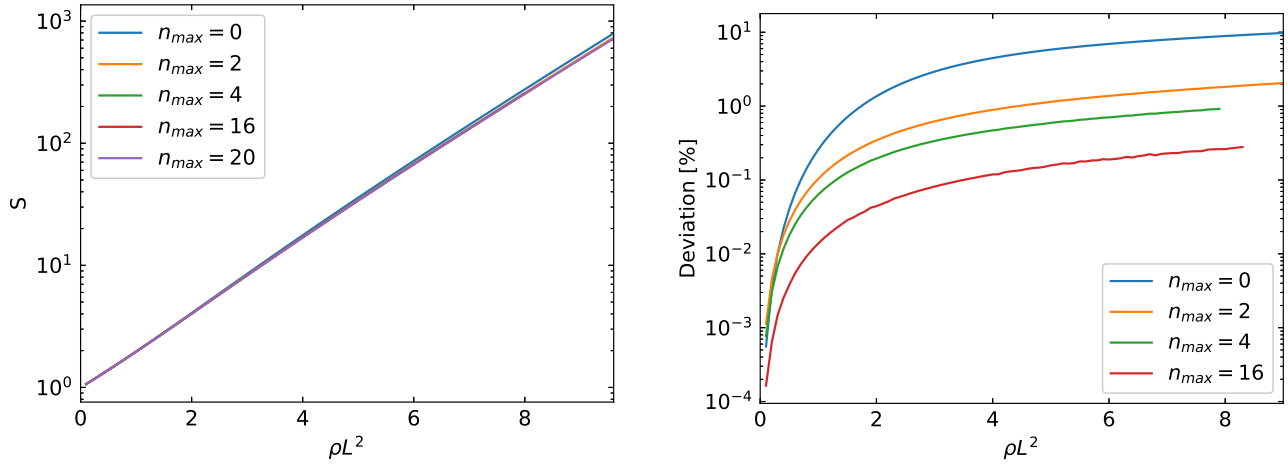

(a) (b)

Figure 4.4: (a) A plot of the mean cluster size for various cut-off sizes $n_{\max}$ as a function of the reduced density ρL^2. (b) A plot of the relative deviation with respect to the $n_{\max} = 20$ expansion, as a function of ρL^2.

Figure 4.5 we plot the mean cluster size as function of the scaled density ρL^2 for $n_{\max} = 4$ over a larger range in the scaled density ρL^2. Similarly to the ideal disk particles that we discussed in section 3.7, we observe that the mean cluster size grows exponentially and does not deviate from this growth up to the edge of the convergence region $\rho L^2 = 15.8$. While the convergence in the ideal disk case was limited by the accuracy of the method itself, here the accuracy of the initial guess for the iterative solver is the limiting factor. At this density we are 2.6 times further away from the Monte Carlo prediction of the percolation threshold than the result of the second virial approximation. This demonstrates that the Percus-Yevick closure is not useful in percolation of ideal particles in two dimensions. While being a more sophisticated closure than the second virial approximation, it turns out less accurate than the simple mean field theory for both isometric and highly anisometric particles. This shows that, at least for ideal particles, Percus-Yevick is an ill-suited choice as a closure in two dimensions.

4.4 Angular resolution

While Percus-Yevick theory is ill-qualified to describe cluster formation near the percolation threshold, we expect it to be accurate at low densities and moderately accurate at medium densities. Since the (angular resolved) pair connectedness functions have been obtained from Monte Carlo simulations, we can discuss both the accuracy of the Percus-Yevick closure at low densities and the convergence of the rotational invariant basis [21].

We first investigate the angular-averaged pair connectedness function $\bar{P} = \langle\langle P(r, \theta_1, \theta_2)\rangle_{\theta_1}\rangle_{\theta_2}$ in Figure 4.6 for various densities from $\rho L^2 = 2.5 - 5$, reminding the reader that $\rho L^2 = 5.63728(2)$ is the percolation threshold [15]. We observe good agreement for low densities, yet Percus-Yevick

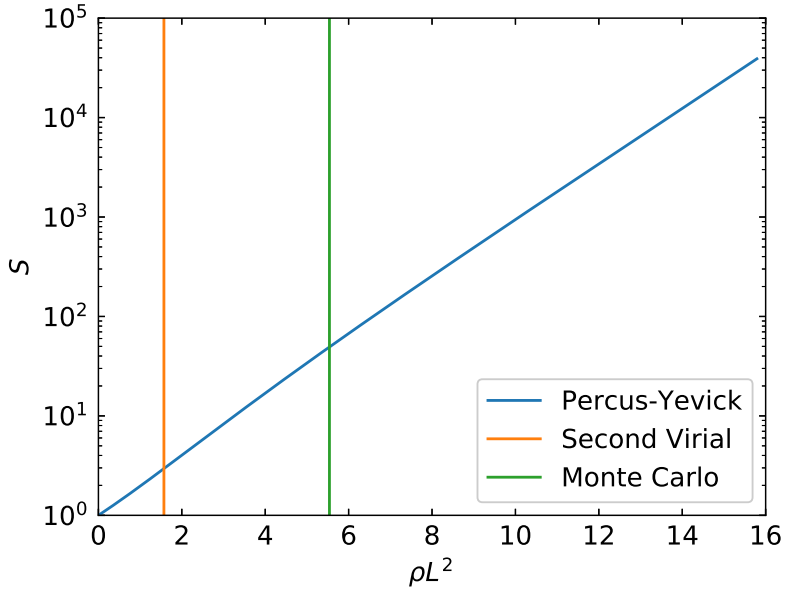

Figure 4.5: The mean cluster size obtained via the Percus-Yevick approximation is shown as a function of the scaled density ρL^2. The second virial approximation and the Monte Carlo predictions for the percolation threshold are indicated in orange and green, respectively.

slightly underestimates the connection probability. Closer to the percolation threshold we expect the agreement to become worse, which we do indeed observe in Figure 4.6c and Figure 4.6d. The shape of the pair connectedness functions for $r/L < 1$ is dominated by overlap effects, and both the Monte Carlo results and the Percus-Yevick approximation show a similar kink at $r/L = 1/2$, which is caused by the sharp change in overlap probability.

To facilitate the comparison between the angular resolved Monte Carlo results and the results from Percus-Yevick theory, we change the orientational basis from θ_1 and θ_2 to the more convenient basis shown in Figure 4.7. This change of basis consists of relabelling θ_1 to α and introducing θ as the angle between the orientation vectors of the two labelled particles. In the isotropic phase, the θ-angle is the only orientational information necessary to describe percolation for anisometric nanofillers and therefore we only discuss the dependency of this angle [10]. Using this full angular information, we are also able to inspect the convergence of the complete rotational invariant expansion. We find that for $\theta < \pi/4$ the main features are replicated for $n_{\max} > 10$ and the expansion becomes representative for $n_{\max} > 16$. For $\pi/4 < \theta < \pi/2$ the main features are present for $n_{\max} > 6$ and the agreement becomes accurate for $n_{\max} > 12$.

In Figure 4.8a, we plot the angular resolved Percus-Yevick results for θ, where we use $n_{\max} = 20$ for maximum accuracy in Percus-Yevick theory. The angular resolution for the pair connectedness function $P(1,2)$ at low densities is $\Delta\theta = 10°$, whereas at high densities $\Delta\theta = 3°$. The y-axis is normalised such that, after summation of all angular bins, we retain the angular averaged pair connectedness function $\langle\langle P(r,\theta_1,\theta_2)\rangle_{\theta_1}\rangle_{\theta_2}$. We observe that the angle-dependence of the pair connectedness function is limited to $r/L < 1$, whereas for $r/L > 1$ the functions are not dependent

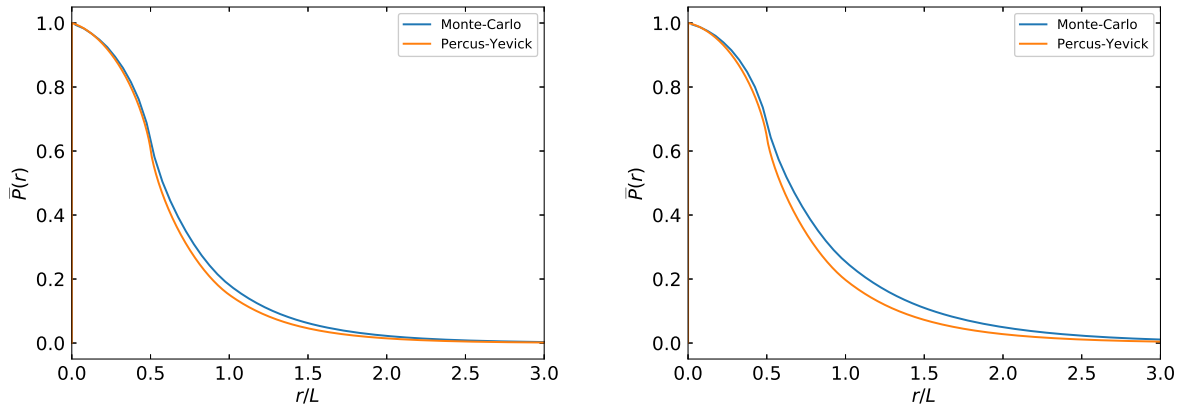

(a) $\rho L^2 = 2.5$

(b) $\rho L^2 = 3.0$

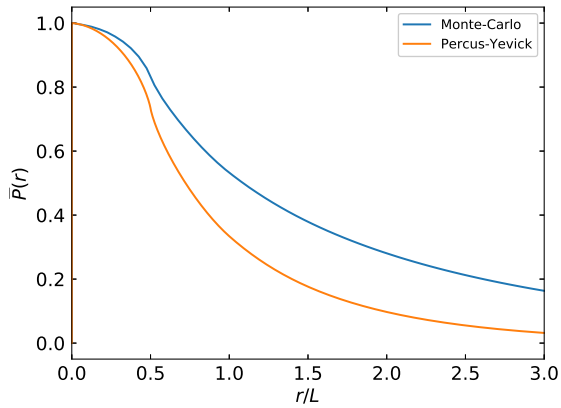

(c) $\rho L^2 = 4.5$

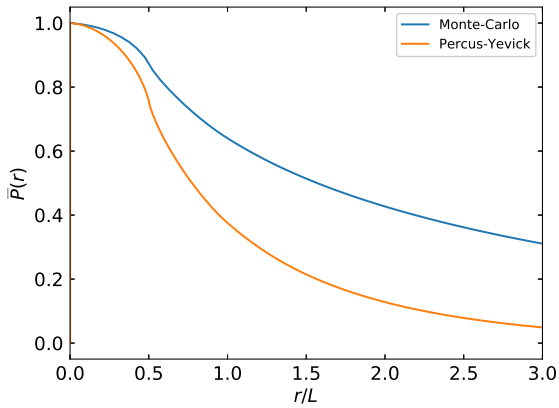

(d) $\rho L^2 = 5.0$

Figure 4.6: The angular averaged pair connectedness function $\bar{P}(r)$, both for the Percus-Yevick closure and Monte Carlo simulations [21].

on the relative orientation θ. We observe the presence of a plateau for which the particles overlap, independent of the orientation. This plateau should correspond to the Percus-Yevick condition $P(1,2) = 1$ for overlap, but small violations are present, likely due to the (limited) expansion we employ. Secondly, we observe oscillatory behaviour for $0.25 < r/L < 0.5$, which might be reduced by increasing the cutoff value $n_{\max}$. The fact that the angle-dependence is limited to $r/L < 1$ indicates that for ideal particles, the angle-dependence is essentially a matter of whether the two particles directly overlap or not.

In Figure 4.8b, we plot the comparison between the Percus-Yevick approximation and results obtained from Monte Carlo simulations for the two selected bins $0 < \theta < 10$ and $80 < \theta < 90$, with other bins being similarly accurate. We observe almost perfect agreement between Percus-Yevick theory and Monte Carlo simulations. The small differences are of oscillatory nature and can be negated by increasing the rotational invariant expansion size. This remarkable agreement is not entirely unsurprising, as Percus-Yevick is exact up to the first order in the density ρ.

Near the percolation threshold, however, the agreement is expected to decrease significantly

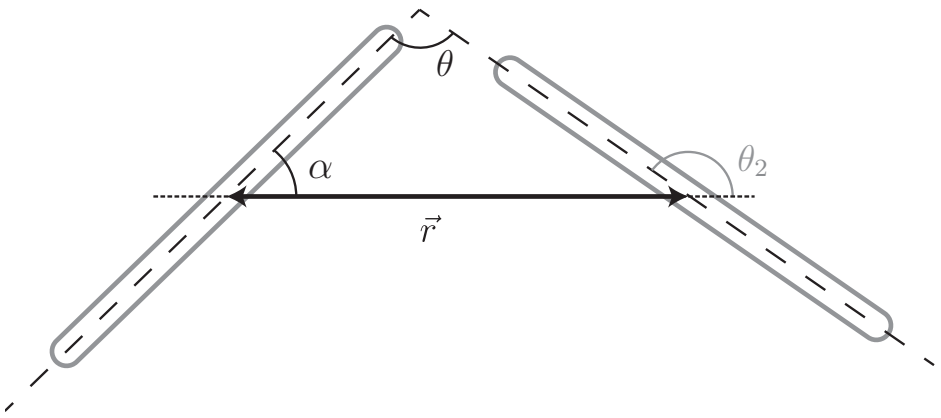

Figure 4.7: The new angular basis, where we have relabelled θ_1 as α, and labelled the angle between the two particles θ.

as shown in Figure 4.9a. Here we plot the Percus-Yevick results and the Monte Carlo results for the smallest-angle bin and the largest-angle bin. We observe a significant difference between the Percus-Yevick result and results obtained from Monte Carlo simulations. Yet, we observe that the *features* of the pair connectedness functions appear to be in good agreement. This suggests that the difference in the angular resolved pair connectedness function is mainly caused by the difference in average connectivity, *i.e.*, the orientation dependency is correct, while $\langle\langle P(r,\theta_1,\theta_2)\rangle_{\theta_1}\rangle_{\theta_2}$ is not. Indeed, by appropriately density-mapping the Percus-Yevick results onto the Monte Carlo results, we obtain similar agreement as in the low density case as shown in Figure 4.9b. We do observe a minor deviation at $r/L \ll 1$ for the small angle Monte Carlo results, which we assume to be caused by an error in the Monte Carlo data. Secondly, we observe a minor deviation at $r/L \approx 0.75$, which indicates that the mapping cannot be done exactly.

The nearly exact mapping between Percus-Yevick calculations and the Monte Carlo simulation results at high densities suggests that we might be able to extend this mapping to all densities. We discuss this possibility in the next section.

4.5 Beyond Percus-Yevick

The rescaled density approach

We can apply a mapping to the angular-averaged Monte Carlo results of Figure 4.6 that is similar to that in the angular resolved pair connectedness functions. For this purpose, it is necessary to accurately map both the short and long-ranged behaviour of the pair connectedness function. We find that this mapping can be best fitted under the assumption that the Percus-Yevick mean cluster size S scales exponentially, while the Monte Carlo mean cluster size scales like in the critical region as $S \sim |\rho_{MC} - \rho_p|^{-\gamma}$. Hence, we propose a fit of the form

$$(\rho L^2)_{\mathrm{PY}} = A - B\ln(|\rho_{\mathrm{MC}} - \rho_p|L^2), \tag{4.26}$$

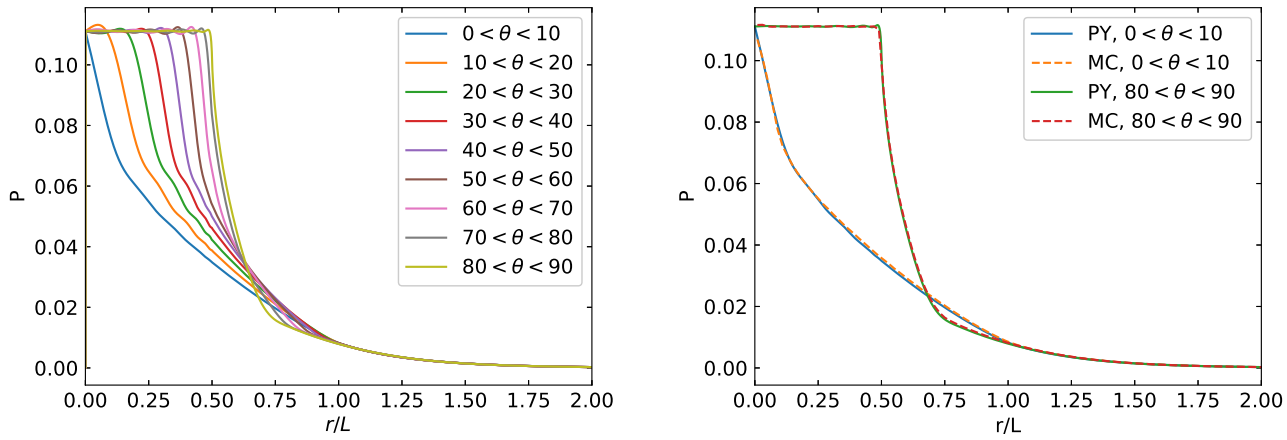

(a) $\rho L^2 = 1.5625$ (b) $\rho L^2 = 1.5625$

Figure 4.8: (a) The angular distribution of the pair connectedness function $P(r)$ obtained from Percus-Yevick theory for the inter-particle angle θ. (b) Two highlighted angular resolved pair connectedness functions $P(r)$ for $0 < \theta < 10$ and $80 < \theta < 90$ for both Percus-Yevick theory and Monte Carlo simulations.

where A and B are fit parameters. We show the density-mapping in Figure 4.10. The black dots represent the density mapping, where we have indicated an uncertainty of $\Delta(\rho L^2) = 0.1$, which is both due to the slightly imperfect mapping, and the fact that we have iterated the pair connectedness function using density increments $\Delta\rho = 0.1$. The blue line represents the fit (4.26), where $A = 7.69 \pm 0.01$ and $B = 4.26 \pm 0.02$, and the orange line indicates $(\rho L^2)_{\mathrm{PY}} = (\rho L^2)_{\mathrm{MC}}$. The fit is within the error bounds for all densities we have compared. While this fit is accurate within the data range, it cannot be used to extrapolate knowledge of S_{PY}. The usefulness of this mapping is fully dependent on the information that is to be extracted. While estimates for, *e.g.*, critical exponents can be obtained, this is likely more easily obtained from the Monte Carlo simulations themselves. Secondly, this mapping cannot be done for a cherry-pit model, since this model depends on $g_{\mathrm{PY}}(r, \theta_1, \theta_2)$, which is only accurate at low densities.

The GMSA-approach

A second heuristic method to go beyond the Percus-Yevick approximation is to functionalise the missing parts in Percus-Yevick theory with respect to the 'exact' Monte Carlo simulations. As the only assumption in Percus-Yevick theory for ideal particles is $C^+(1,2) = 0$ for non-overlapping particles, we relax this condition and use an appropriate description for $C^+(1,2)$ outside the overlap region. This treatment is therefore similar to the previously discussed Generalised Mean Spherical Approximation (GMSA). While a GMSA-like approximation has yielded satisfying results in a three dimensional model, its use was largely facilitated by the analytical solutions [26]. While it is possible to extract the missing components of $C^+(1,2)$ from the data of the Monte Carlo simulations, we find it easier to invert our Percus-Yevick solution. We use the Percus-Yevick pair connectedness function $P(1,2)$, replace the density in the Ornstein-Zernike Equation by the density

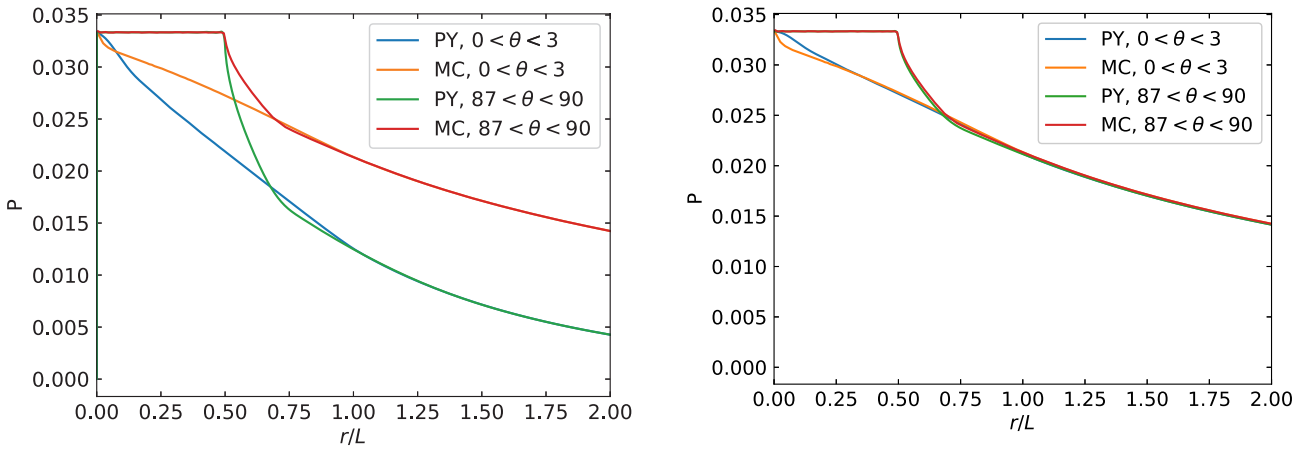

(a) $\rho L^2 = 5$ (b) $(\rho L^2)_{\mathrm{PY}} = 9.6$ and $(\rho L^2)_{\mathrm{MC}} = 5$

Figure 4.9: (a) Two highlighted angular resolved pair connectedness functions $P(r)$ for $0 < \theta < 3$ and $87 < \theta < 90$ for both Percus-Yevick theory and Monte Carlo simulations. There is a large disagreement between Percus-Yevick theory and Monte Carlo simulations. (b) The same two angular resolved pair connectedness functions $P(r)$, compared for different densities of Percus-Yevick theory and Monte Carlo simulations.

we obtain from the mapping on the Monte Carlo results, and calculate the corresponding $C^+(1,2)$. In Figure 4.11a, we plot the parts of $\langle\langle C^+(1,2)\rangle\rangle$ that the Percus-Yevick closure ignores. This suggests an Ansatz with an exponentially decaying tail for $r/L > 1$, whereas for $r/L < 1$ more care has to be taken. In Figure 4.11a we plot an example of the angular resolved direct connectedness function $C^+(r,\theta)$ for $30 \leq \theta \leq 40$. Indeed, significant oscillations are present for which an Ansatz is not readily found. Only implementing this correction for $r/L > 1$, or implementing a correction to the angular averaged component $\langle\langle C^+(1,2)\rangle\rangle$ only, yields unsatisfactory results and we have therefore not pursued this approach further. We believe that this approach is likely fruitful for particles that are only lightly anisometric, but too complex for strongly anisometric particles.

The PY-d approach

Besides these heuristic techniques to improve upon Percus-Yevick theory, a more systematic method exists also. This method is based on a correction that adds the missing diagrams in Percus-Yevick in an order-by-order approach. Since Percus-Yevick is correct to the first order in the density, but misses some diagrams in the definition of the second order (and higher) in the density, the correction includes these missing diagrams systematically. This approximation has been investigated by several authors and has been shown to be more accurate than the normal Percus-Yevick approximation for spherical particles. Generally, the predicted percolation threshold using this method is too low [28]. This systematic approach is usually referred to as the PY-d approximation [28, 60]. For the first order correction in this approach to be useful, we need to be able to calculate two specific four-particle cluster integrals. These integrals can be calculated analytically for spherical particles, and therefore it is likely that this contribution might also be

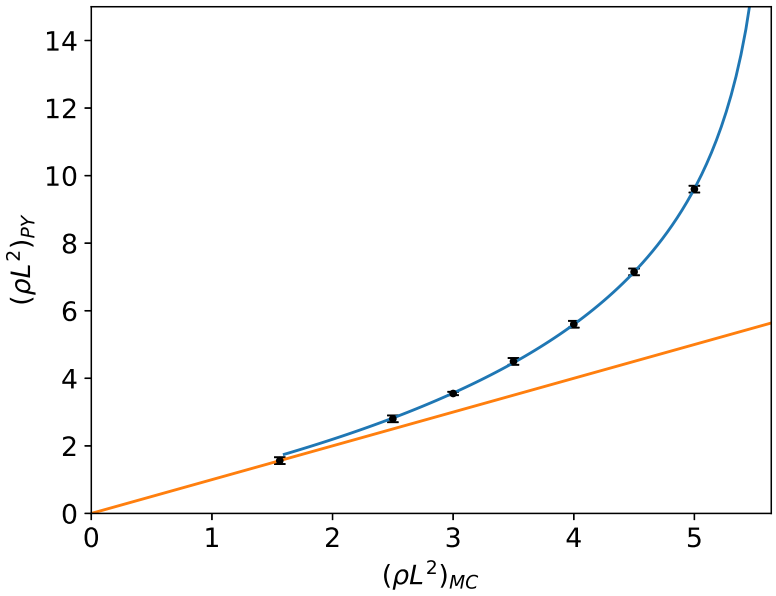

Figure 4.10: The density-mapping between the Percus-Yevick approximation and Monte Carlo simulations. The orange line indicates $(\rho L^2)_{\mathrm{PY}} = (\rho L^2)_{\mathrm{MC}}$, the black dots indicate the density mapping with an uncertainty of $\Delta(\rho L^2) = 0.1$. The blue curve is the fit (4.26) with parameters $A = 7.69 \pm 0.01$ and $B = 4.26 \pm 0.02$.

obtained analytically for disk particles in two dimensions [28, 61]. The cluster integrals for line segments, however, are more involved and to our knowledge only three particle cluster integrals have been calculated analytically, while four (or more) particle cluster integrals are usually calculated via Monte Carlo integration techniques. We prefer not to speculate on the feasibility of this method for line segments or other anisometric particles.

While more methods exist to study percolation in two dimensions, this was outside the scope of this thesis. In the next section we continue our study on the effect of the ordering due to the smectic-A phase on percolation in a three-dimensional model, and we come back to the topic of percolation in two dimensions in the Outlook.

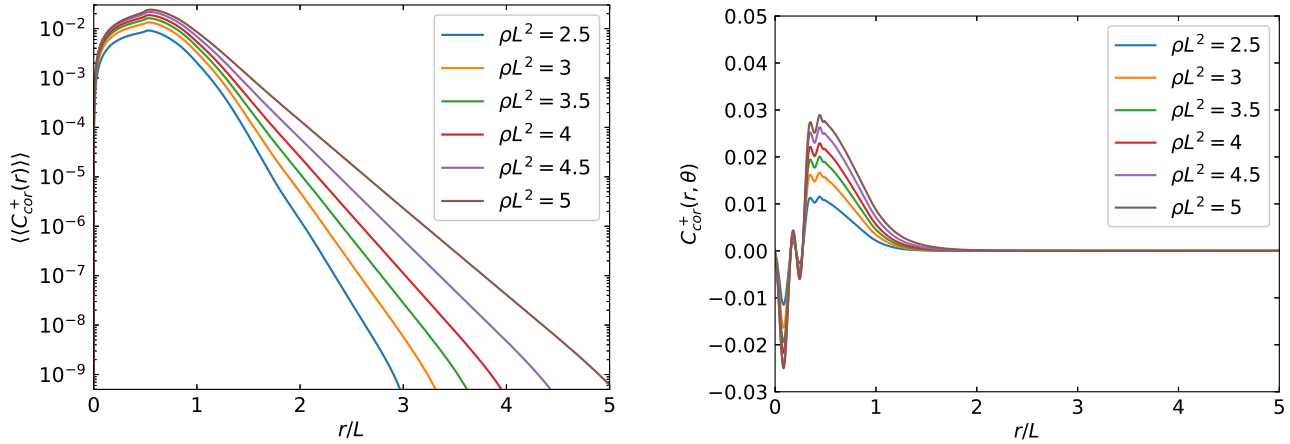

(a) (b)

Figure 4.11: (a) The angular averaged correction term that corrects the Percus-Yevick assumption $C^+(1,2) = 0$ for non-overlapping particles. The tail is an exponentially decaying function for $r/L > 1$. (b) The angular dependent correction term, for the bin $30 \leq \theta \leq 40$. Significant oscillatory behaviour for $r/L < 1$ is present.

Part II

Percolation in a non-uniform spatial density profile

Chapter 5

Smectic-A phase

5.1 Introduction

The effect of liquid-crystalline ordering on percolation in a three dimensional model of slender nanoparticles has, to our knowledge, only been studied in the isotropic and the nematic phase [62], where the local density distribution is only dependent on the particle orientations. Continuum percolation theory has, to our knowledge, not been applied to any other spatially inhomogeneous phase. The onset of the smectic-A phase in an solution is relatively sensitive to the properties of the particles, such as the polydispersity, flexibility and particle-particle interactions [63–66]. In the particular case of carbon nanotube suspensions, the smectic-A phase has not (yet) been observed experimentally [67]. Theoretically, it has been predicted that, for CNTs, the columnar phase might pre-empt the smectic-A phase due to the van der Waals interactions [64]. Also, carbon nanotubes are typically rather polydisperse, which is known to hinder the formation of a smectic-A phase [65]. Nanowires on the other hand, do exhibit smectic phases, and a fundamental question is how the positional ordering of the smectic-A phase affects the formation of particle networks [68, 69]. Since the smectic-A phase is ordered only in one direction, whereas it maintains fluid-like in the other directions, the normal Ornstein-Zernike formalism might be applicable without significant adjustments. We note that charge transport in a smectic-A phase has been studied with numerical simulations by Schrader *et al.* [70], which indicate that the formation of a smectic-A phase hinders charge transport.

Before we can investigate how the spatial inhomogeneity influences the percolation behaviour, we need to determine the density profile of the smectic-A phase. In the next sections we discuss the theoretical concepts necessary to derive an analytical expression for the smectic-A density distribution using Density Functional Theory (DFT).

5.2 Density Functional Theory

Density Functional Theory is one of the most celebrated theoretical tools to investigate inhomogeneous phases and comes in many different flavours. It is based on the mathematical concept of

functionals, which can be regarded as an extension of functions, *i.e.*, while a function maps a point x to a complex number as

$$f(x) : x \to \mathcal{C}, \tag{5.1}$$

a functional maps a function $f(x)$ onto a complex number as

$$\mathcal{F}[f] : f(x) \to \mathcal{C}. \tag{5.2}$$

The widespread use of classical DFT is based on a set of theorems that show that (1) for any choice of the volume V, the temperature T and the chemical potential μ, the Helmholtz free energy $F[\rho(\vec{r})]$ is a unique functional of the equilibrium density distribution $\rho(\vec{r})$, and (2) that a functional $\Phi[n(\vec{r})]$ of the one-particle distribution function n exists, which is minimised if $n(\vec{r})$ coincides with the equilibrium single-particle density $\rho(\vec{r})$. The value of $\Phi[n(\vec{r})]$ at this minimum coincides with the grand potential. A proof of these two theorems can be found in Hansen and McDonald [19].

These two theorems show that all relevant thermodynamics is present in the functional $\Phi[\rho(\vec{r})]$. Since the minimum of the functional $\Phi[\rho(\vec{r})]$ is the grand potential, we start by writing the grand potential in terms of the Helmholtz free energy as

$$\Omega[\rho(\vec{r})] = F[\rho(\vec{r})] - \mu \int \mathrm{d}\vec{r}\rho(\vec{r}), \tag{5.3}$$

where we have constrained the total number of particles via

$$\int \mathrm{d}\vec{r}\rho(\vec{r}) = N. \tag{5.4}$$

Since our goal is to obtain the smectic-A density distribution, we need to minimise the grand potential (5.3) with respect to the density. The extrema of a functional, analogously to the extrema of a function, are obtained by taking the functional derivative as

$$\frac{\delta\Omega[\rho(\vec{r})]}{\delta\rho(\vec{r})} = 0. \tag{5.5}$$

We refer to Engel and Dreizler [71] and references therein for an in-depth discussion on functionals and functional derivatives. The extrema of Equation (5.3) can now be obtained via

$$\frac{\delta F[\rho]}{\delta\rho(\vec{r})} - \mu = 0. \tag{5.6}$$

This indicates that the equilibrium density distribution function $\rho(\vec{r})$ is obtained from a constrained minimisation of the Helmholtz free energy. This Helmholtz free energy can be split in an ideal part and an excess part as

$$\beta F = N \ln \rho\nu - N + \beta F^{\text{excess}}, \tag{5.7}$$

where N is the number of particles, ν is a volume length scale, and βF^{excess} is the excess free energy, that depends only on the particle-particle interactions. The precise form of the volume

length scale ν is of no consequence in our model. We refer any interested reader to Allen *et al.* [72] for a discussion of it.

The Helmholtz free energy (5.7) can be written as a functional of the singlet-density distribution $\rho(\vec{r})$ as

$$\beta F[\rho(\vec{r})] = \int \mathrm{d}\vec{r}\rho(\vec{r})(\ln \rho(\vec{r})\nu - 1) + \beta F^{\text{excess}}[\rho(\vec{r})]. \tag{5.8}$$

The excess free energy functional $\beta F^{\text{excess}}[\rho(\vec{r})]$ is not known in closed-form. A formally exact expression for the excess free energy can be derived if the inter-particle potential $V(\vec{r}^N)$ depends solely on pair interactions, and consists of a sum of all n-particle cluster integrals, most of which have no analytical result [19]. Approximations for the excess free energy exist at various levels of complexity and are often the limiting factor in the accuracy of density functional theory [19].

5.3 The smectic-A density distribution

Expressions for the Smectic-A density distribution have been obtained via several different approximation for the excess free energy. Elaborate theories take the orientational distribution and inter-layer particles into account, while the simplest theories are based on perfectly aligned rods or spherocylinders [73–76]. While all these effects can have a tremendous effect on percolation in a smectic-A phase, the analytic nature of the perfectly aligned rod model is favoured over the more complex model that are only solvable numerically [76].

Therefore we follow a slightly modified approach of Mulder [76] to derive the equilibrium density distribution. In this model, the excess free energy functional is based on the first order component in the cluster integral expansion, and is given by

$$\beta F^{\text{excess}}[\rho(\vec{r})] = \frac{1}{2}\Gamma(\eta) \int \mathrm{d}\vec{r}_1 \int \mathrm{d}\vec{r}_2 \rho^{(1)}(\vec{r}_1)\rho^{(1)}(\vec{r}_2) f(\vec{r}_1, \vec{r}_2). \tag{5.9}$$

Here, $f(\vec{r}_1, \vec{r}_2)$ is the Mayer$f$-function defined by Equation (2.16), and $\Gamma(\eta)$ is the Parsons-Lee correction term given by

$$\Gamma(\eta) = \frac{1 - \frac{3}{4}\eta}{(1-\eta)^2}. \tag{5.10}$$

This correction term effectively includes higher order corrections to Equation (5.9) to account for the effects of a finite particle aspect ratio[1], where η is the global average volume fraction [77, 78]. The use of the Parsons-Lee correction term, or similar, is necessary as higher order terms in the excess free energy are not negligible for the smectic-A phase of perfectly aligned particles [76, 79]. Better results might be obtained by using a so-called smoothed density approximation, where the global volume fraction η in Equation (5.10) is replaced by a weighted local value [80].

[1]Interestingly, this correction term was derived in two completely different manners. It can be derived from a decoupling approximation, by decoupling the orientational and radial dependency of the radial correlation function, as shown by Parsons [77]. It can also be derived by a rescaling of the effective excess free energy by interpolating between that of a sphere and of an infinitely slender rod, as shown by Lee [78].

We apply the theory on uncapped cylinders with hard core interactions only, in which case the Mayer f-function is given by

$$f(\vec{r}_1, \vec{r}_2) = -\Theta(D^2 - x^2 - y^2)\Theta(L - |z|), \tag{5.11}$$

where Θ denotes the Heaviside step function, D is the diameter of particle and L is the length of the particle. Since the Smectic-A phase is a partially ordered phase that is periodic over a length λ, we can use the following Ansatz for the density distribution

$$\rho^{(1)}(\vec{r}) = \rho\psi(qz) = \rho\left(1 + \sum_{j=1} \Delta_j \cos(jqz)\right), \tag{5.12}$$

where Δ_j is the amplitude of the j^{th} coefficient of the expansion in the density wave and $q = |\vec{q}|$ is the associated wave vector, which is linked to the wavelength by $\lambda = \frac{2\pi}{q}$. Inserting Equation (5.9), (5.11) and (5.12) into Equation (5.8) and taking the thermodynamic limit (*i.e.*, $V \to \infty$, $N \to \infty$, and $N/V =$ constant) we obtain the free energy per particle

$$\mathcal{F}[\psi] = \frac{\beta F[\psi]}{N} = \ln\rho - 1 - \Lambda + \frac{1}{2\pi}\int_0^{2\pi} \mathrm{d}\zeta\psi(\zeta)\ln\psi(\zeta) + 4\eta\Gamma(\eta)\left(1 + \frac{1}{2}\sum_{m=1}^{\infty}\Delta_m^2 j_0(mQ)\right), \tag{5.13}$$

where $\zeta = qz$, $\eta = \rho\frac{\pi}{4}D^2L$ is the volume fraction of the particles, j_0 is the zeroth-order spherical Bessel function and $Q = qL$. A stable phase is described by the spatial distribution function that minimises this free energy per particle. The two control parameters for this spatial distribution function are the Smectic-A density parameter Δ_m and the wave vector Q. The solution must be stable with respect to both of these variables, hence

$$\frac{\delta\mathcal{F}[\psi]}{\delta\Delta_n} \stackrel{!}{=} 0 \qquad (n \geq 1), \qquad\qquad \frac{\delta\mathcal{F}[\psi]}{\delta Q} \stackrel{!}{=} 0. \tag{5.14}$$

Applying these two conditions to Equation (5.13) results in

$$X^{(n)}(\{\Delta_i\}, Q, \eta) = \frac{1}{2\pi}\int_0^{2\pi}\mathrm{d}\zeta\cos(n\zeta)\ln\left(1 + \sum_{k=1}^{\infty}\Delta_k\cos(k\zeta)\right) + 4\eta\Gamma(\eta)\Delta_n j_0(nQ) = 0 \tag{5.15}$$

$$Y(\{\Delta_i\}, Q, \eta) = \Gamma(\eta)\eta\sum_{m=1}^{\infty} m\Delta_m^2 j_1(mQ) = 0. \tag{5.16}$$

A one-parameter family of solutions to these equations can be obtained by using a bifurcation analysis [76]. In a bifurcation analysis we inspect the density modulation for small distances away from the critical point, which allows us to obtain the functional behaviour of the parameters η, Δ_j and Q. Hence, we expand η, Δ_j and Q in the parameter ϵ which denotes the distance from the bifurcation point, which is the critical density where the nematic phase becomes unstable with respect to density modulations. These expansions are given by

$$\begin{aligned}
\eta_\epsilon &= \eta^* + \epsilon\eta_1 + \epsilon^2\eta_2 + \ldots \\
\Delta_j &= \epsilon\Delta_j^{(1)} + \epsilon^2\Delta_j^{(2)} + \ldots \\
Q_\epsilon &= Q^* + \epsilon Q_1 + \epsilon^2 Q_2 + \ldots .
\end{aligned}$$

Since the parameter ϵ is assumed to be much smaller than one, we obtain the density distribution of the smectic-A phase near the phase transition only, which is indicated by $\epsilon = 0$.

5.3.1 Zeroth order bifurcation

The Equations (5.15) and (5.16) cannot be solved in their current state, since we have effectively linked all expansion coefficients $\{\Delta_j\}$ to Q_ϵ and η_ϵ. Yet, we can decouple them on a simple physical reasoning, as it can be expected that the fluctuations with the largest periodicities have the largest amplitudes Δ. Hence, we link the largest wave vector to Δ_1, the second largest to Δ_2 and so on. This is similar to the Ansatz by Mulder [76]. Using this decoupling, the zeroth order density distribution is given by

$$\rho(z)/\rho = 1 + \epsilon\Delta_1 \cos(Qz), \tag{5.17}$$

which leads to the bifurcation point

$$1 + 8\Gamma(\eta^*)\eta^* j_0(Q^*) = 0, \tag{5.18}$$

$$j_1(Q^*) = 0. \tag{5.19}$$

This show that the critical density at which the bifurcation occurs is $\eta^* = 0.338$ and the associated wave vector is $Q^* = 4.493$, corresponding to the wavelength $\lambda \approx 1.39L$. The critical volume fraction $\eta^* = 0.338$ is below the Monte Carlo result of $\eta^*_{\mathrm{MC}} \approx 0.36$, whereas the wavelength is too high compared to the Monte Carlo result $\lambda_{\mathrm{MC}} = 1.27L$ [81]. We note that Δ_1 is a free parameter and can be arbitrarily set, as all higher order parameters are scaled to Δ_1.

Although Equation (5.17) is valid for small ϵ, it does not contain information how ϵ evolves as function of the volume fraction. To obtain ϵ as function of the volume fraction, it is necessary to extend the bifurcation analysis to at least the second order in the volume fraction η.

5.3.2 Higher order bifurcations

While we have only developed the density around the bifurcation point up to the first order in ϵ, it is fairly straightforward, though involved, to extend it to higher orders. We do not discuss the extension here, as a full derivation is presented by Mulder [76]. It turns out to be useful to define $\omega_0 = \Gamma(\eta_0)\eta_0 = 0.575$ due to our slightly modified excess free energy by inclusion of the Parsons-Lee correction. Table 5.1 shows the results up to second order in ϵ.

Table 5.1: Summary of the higher order bifurcation coefficients up to second order in ϵ with $\omega_0 = 0.575$.

0^{th} order	1^{st} order	2^{nd} order
$\eta_0 = 0.33774$	$\eta_1 = 0$	$\eta_2 = \frac{1}{8j_0(Q_0)}[\frac{1}{2}\Delta_2 - \frac{1}{4}]$
$Q^* = 4.493$	$Q_1 = 0$	$Q_2 = -2\Delta_2^2 j_1(2Q_0)/j_0(Q_0)$
$\Delta_1 = 1$	$\Delta_2 = \frac{1}{4(1+8\omega_0 j_0(2Q_0))}$	$\Delta_3 = \frac{\frac{1}{2}\Delta_2 - \frac{1}{12}}{1+8\omega_0 j_0(3Q_0)}$

Using the coefficients up to second order in ϵ, we can write the density distribution $\rho^{(1)}(z)$ as

$$\rho^{(1)}(z)/\rho = 1 + \sum_{j=1}^{3} \Delta_j \epsilon^j \cos\left((Q^* + \epsilon Q_1 + \epsilon^2 Q_2) j \frac{z}{L}\right). \tag{5.20}$$

We can express ϵ as a function of η at the level of the second order bifurcation as

$$\epsilon \sim \sqrt{\frac{\Gamma(\eta)\eta}{\Gamma(\eta_0)\eta_0} - 1}. \tag{5.21}$$

In Figure 5.1 we plot the density distribution $\rho^{(1)}(z)/\rho$ obtained by the second order bifurcation analysis (5.20). We plot both the leading order term in the smectic-A density distribution (*i.e.*, $\rho^{(1)}(z)/\rho = 1 + \epsilon\cos(Q^* z/L)$), and Equation (5.20). While the leading order term misses the sharpening of the distribution, it is a good approximation of the general shape of the distribution for $\epsilon \ll 1$. Figure 5.1b indicates the expansion for $\epsilon = 1$, where the condition that $\epsilon \ll 1$ breaks down and is therefore not necessarily an accurate representation of the singlet-density $\rho^{(1)}(z)$. Larger volume fractions cannot be shown without either going to higher orders in ϵ or numerically evaluating the coefficients Δ_j, Q_j and η_j.

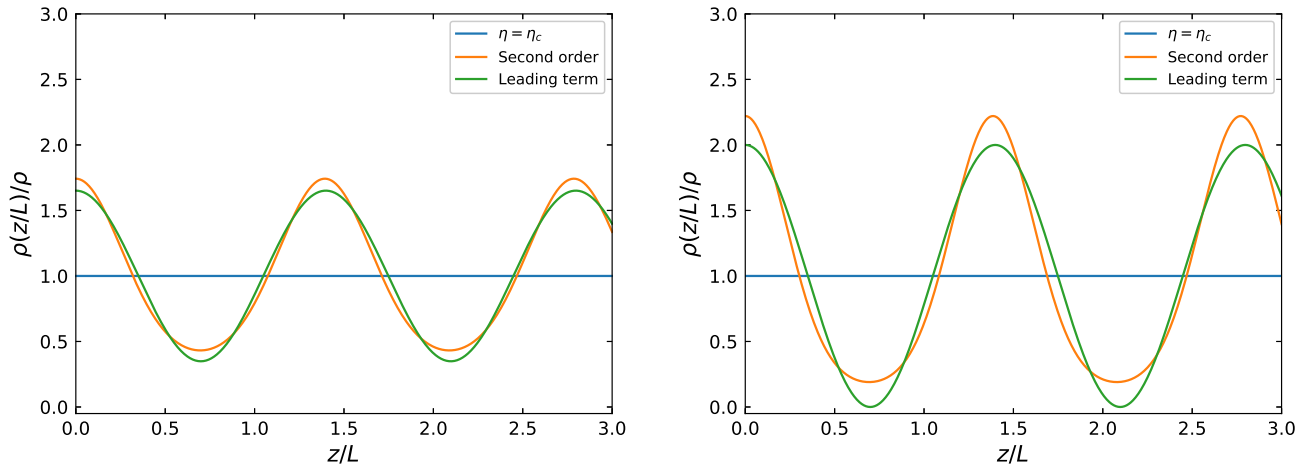

(a) volume fraction $\eta = 0.35$

(b) volume fraction $\eta = 0.3657$

Figure 5.1: Plot of the normalised density distribution function as a function of the position z/L. We plot both the distribution based on the leading order term Δ_1, and on the second order bifurcation density distribution.

The uncapped cylinders approach is the simplest density functional approach, but ignores many aspects that are important. While not necessarily intuitive, the onset of a smectic phase in perfectly aligned particles depends heavily on the particle morphology. For example, it can be shown that a parallel hard ellipsoid (PHE) model cannot exhibit a smectic phase. The reason for this is simple:

a perfectly aligned PHE model can be obtained as an affine transform of a hard sphere model, and a hard sphere model does not exhibit smectic phases. Hence, as nanofillers rarely are perfectly uncapped cylinders, the theory is likely only accurate in the slender rod limit $L/D \to \infty$.

More sophisticated methods are necessary for finite aspect ratios if end caps are present, as it has been found to have a noticeable influence on the wave vector Q and the critical density η^*. This must arguably have a significant influence on the formation of a percolating network [81].

Chapter 6

Continuum percolation in the smectic-A phase

The smectic-A phase is a spatially inhomogeneous phase, hence we require connectedness percolation theory in an inhomogeneous form. While not immediately obvious, this does significantly complicate the possibility to derive analytical results. This is most evident from the Ornstein-Zernike equation, as it is no longer possible to use the convolution theorem to reduce it to an algebraic equation in Fourier space. The theoretical knowledge on spatial inhomogeneities in continuum percolation is limited. Some results exist using the Percus-Yevick closure, as it can be solved analytically near a hard wall [82]. Furthermore, spatial inhomogeneities have been investigated by Chatterjee and Grimaldi [83] using a lattice mapping to study both the effect of local volume fraction fluctuations of cylinders, and the effect of phase separation [83, 84].

Considerably more effort has been devoted to integral equation theory of inhomogeneous fluids [85]. Since the equations in inhomogeneous percolation are similar to those for inhomogeneous fluids, we can use methods specifically developed for inhomogeneous fluids and apply them to percolation theory. While we are interested in an externally applied density distribution and derive the resulting percolation properties, most of these models use a completely coupled set of equations, in which both the pair correlation functions and the singlet-density are extracted from the governing equations [85]. Numerically studying inhomogeneous fluids via integral equation theories is known to be computationally demanding, since the solutions depend on the position of all particles, not just relative distances. An efficient numerical approach was recently discussed by Lado [86]. Since none of methods known to us are straightforwardly applied to our model, we develop a novel and analytical method to describe percolation in a partially ordered phase. While this method is developed specifically for the smectic-A phase, it is likely that it can be extended to any (partially) ordered phase.

In this chapter, we appropriately reformulate connectedness percolation theory, such that we can obtain analytical results in an inhomogeneous model. Secondly, we derive results for the parallel cylinder model discussed in chapter 5.

6.1 Clusters

We start from definition (2.8) of the mean cluster size in an inhomogeneous form

$$S = 1 + \frac{1}{N} \int \int \mathrm{d}\vec{r}_1 \mathrm{d}\vec{r}_2 \rho^{(1)}(\vec{r}_1)\rho^{(1)}(\vec{r}_2)P(\vec{r}_1, \vec{r}_2). \tag{6.1}$$

The translational invariance of $P(\vec{r}_1, \vec{r}_2)$ is partially conserved, since the density distribution $\rho^{(1)}(\vec{r}_1)$ is only dependent on the coordinate z along the nematic director and independent of the radial component $\vec{R}_1$. Hence the radial component only depends on the distance between two particles, while in the direction along the nematic director both positions have to be considered explicitly. This translates to

$$P(\vec{r}_1, \vec{r}_2) = P(|\vec{R}_1 - \vec{R}_2|, z_1, z_2). \tag{6.2}$$

Using this property, we can simply pre-integrate the radial component in Equation (6.1) to obtain

$$S = 1 + \lim_{q_r \to 0} \frac{A}{N} \int_{-\infty}^{\infty} \rho^{(1)}(z_2)\mathrm{d}z_2 \left[\int_{-\infty}^{\infty} \rho^{(1)}(z_1)\widehat{P}(q_r, z_1, z_2)\mathrm{d}z_1 \right], \tag{6.3}$$

where we use the Fourier notation already employed in chapter 2. Next, we write the density distribution function as $\rho^{(1)}(z) = \rho\psi(z)$, where $\psi(z)$ is a non-normalised density distribution function, which we assume to be an even function of z for convenience. One integral in Equation (6.3) can be limited to one full wavelength $\frac{2\pi}{q}$ due to the periodicity of the smectic distribution function $\psi(z)$, so that

$$S = 1 + \lim_{q_r \to 0} \frac{A}{N} \frac{qL_z}{2\pi} \rho^2 \int_{-\frac{\pi}{q}}^{\frac{\pi}{q}} \mathrm{d}z_2 \int_{-\infty}^{\infty} \psi(z_1)\psi(z_2)\widehat{P}(q_r, z_1, z_2)\mathrm{d}z_1, \tag{6.4}$$

where the integration boundaries of z_2 must represent the symmetry of $\psi(z_2)$. Here, L_z is defined such that AL_z is the total volume V of the system. Therefore $\frac{q}{2\pi}L_z$ is the total number of smectic-A wavelengths in the model. Next, noting that $\rho = \frac{N}{AL_z}$, we can simplify this expression to

$$S = 1 + \lim_{q_r \to 0} \rho \frac{q}{2\pi} \int_{-\frac{\pi}{q}}^{\frac{\pi}{q}} \mathrm{d}z_2 \int_{-\infty}^{\infty} \psi(z_1)\psi(z_2)\widehat{P}(q_r, z_1, z_2)\mathrm{d}z_1. \tag{6.5}$$

We note that, under the symmetry constraints on the model, $\int_{-\frac{\pi}{q}}^{\frac{\pi}{q}} \mathrm{d}z_2 \psi(z_2)\widehat{P}(q_r, z_1, z_2)$ must be an even function of z_1. This holds, as $\psi(z_i)$ is an even function and the integral over z_2 is symmetric around the origin, hence the change of $z_1 \to -z_1$ must leave this integral invariant. We now define an auxiliary function $\widehat{K}(q_r, z_1)$ as

$$\widehat{K}(q_r, z_1) = \frac{q}{2\pi} \int_{-\frac{\pi}{q}}^{\frac{\pi}{q}} \psi(z_2)\widehat{P}(q_r, z_1, z_2)\mathrm{d}z_2, \tag{6.6}$$

where

$$\frac{q}{2\pi} \int_{-\frac{\pi}{q}}^{\frac{\pi}{q}} \psi(z_2)\mathrm{d}z_2 = 1. \tag{6.7}$$

This implies that $\widehat{K}(q_r, z_1)$ can be seen as the pair connectedness function averaged over the position z_2 of one of the particles. A recently proposed solution strategy for percolation in the nematic phase uses a similar strategy, by pre-averaging over the orientational distribution function of one of the particles [62]. Combining Equation (6.4) with Equation (6.6), we obtain

$$S = 1 + \lim_{q_r \to 0} \rho \int_{-\infty}^{\infty} \psi(z_1) \widehat{K}(q_r, z_1) \mathrm{d}z_1. \tag{6.8}$$

This expression is valid for any liquid under the assumption that it is periodic in only one direction, while remaining liquid-like in all other directions. In chapter 5, we show that the density distribution function $\psi(z)$ for parallel aligned particles can be expressed as a harmonic expansion as

$$\psi(z) = 1 + \sum_j \Delta_j \cos(jqz), \tag{6.9}$$

where Δ_j is the amplitude and q is the associated wave vector. Note that the ϵ^j of the previous section is now absorbed in Δ_j. Inserting $\psi(z)$ into Equation (6.8) and writing the cosine in complex form gives

$$S = 1 + \lim_{q_r \to 0} \rho \int_{-\infty}^{\infty} \hat{K}(q_r, z_1) \mathrm{d}z_1 + \lim_{q_r \to 0} \frac{\rho}{2} \sum_j \Delta_j \int_{-\infty}^{\infty} \left(e^{i(jqz_1)} + e^{-i(jqz_1)} \right) \hat{K}(q_r, z_1) \mathrm{d}z_1. \tag{6.10}$$

This expression indicates that the mean cluster size S contains both a homogeneous term, given by the second term on the right, and an inhomogeneous contribution, given by the third term on the right. The inhomogeneous contribution is simply a Fourier transform of $\widehat{K}(q_r, z_1)$ over z_1, which allows us to rewrite this expression in the compact form

$$S = 1 + \lim_{q_r, q_z \to 0} \rho \widehat{\widehat{K}}(q_r, q_z) + \lim_{q_r \to 0} \rho \sum_j \Delta_j \widehat{\widehat{K}}(q_r, jq). \tag{6.11}$$

Here, $\widehat{\widehat{K}}$ denotes that the function K has been Fourier transformed twice. We have used the fact that $\widehat{K}(q_r, z_1)$ is an even function and therefore the Fourier Transform is invariant under the change $q \to -q$. This definition is consistent with the homogeneous mean cluster size, Equation (2.10), by setting $\Delta_j = 0$ for all j, which gives

$$S = 1 + \lim_{q_r, q_z \to 0} \rho \widehat{\widehat{K}}(q_r, q_z) = 1 + \lim_{q_r, q_z \to 0} \rho \widehat{\widehat{P}}(q_r, q_z). \tag{6.12}$$

The mean cluster size as defined by Equation (6.11) turns out to be convenient for percolation in the inhomogeneous model, as it allows us to reduce the Connectedness Ornstein-Zernike equation to an analytically solvable form, which we derive in the next section.

6.2 The Inhomogeneous Ornstein-Zernike Equation

Now that we have obtained a usable expression for the mean cluster size, we are in the position to rewrite the Ornstein-Zernike Equation (2.12) in an appropriate form. We start with the known

formulation of the connectedness Ornstein-Zernike Equation (2.12)

$$P(|\vec{R}_1 - \vec{R}_2|, z_1, z_2) = C^+(|\vec{R}_1 - \vec{R}_2|, z_1, z_2) + \int \mathrm{d}z_3 \int \mathrm{d}\vec{R}_3 \rho^{(1)}(z_3) C^+(|\vec{R}_1 - \vec{R}_3|, z_1, z_3) P(|\vec{R}_3 - \vec{R}_2|, z_3, z_2), \tag{6.13}$$

where $\vec{R}_i$ represents the radial position of particle i, and z_i the position in the direction along the nematic director. We can use the convolution theorem for the radial vector $|\vec{R}_1 - \vec{R}_2|$ since $\rho^{(1)}(z_3)$ only depends on z_3, so that

$$\widehat{P}(q_r, z_1, z_2) = \widehat{C}^+(q_r, z_1, z_2) + \int_{-\infty}^{\infty} \rho^{(1)}(z_3) \widehat{C}^+(q_r, z_1, z_3) \widehat{P}(q_r, z_3, z_2) \mathrm{d}z_3. \tag{6.14}$$

Next, we multiply both sides by $\frac{q}{2\pi}\psi(z_2)$, integrate over z_2 from $-\frac{\pi}{q}$ to $\frac{\pi}{q}$ and obtain

$$\widehat{K}(q_r, z_1) = \widehat{D}^+(q_r, z_1) + \int_{-\infty}^{\infty} \rho^{(1)}(z_3) \widehat{C}^+(q_r, z_1, z_3) \widehat{K}(q_r, z_3) \mathrm{d}z_3, \tag{6.15}$$

where $\widehat{K}(q_r, z_1)$ is defined via Equation (6.6) and $\widehat{D}^+(q_r, z_1)$ is defined as

$$\widehat{D}^+(q_r, z_1) = \frac{q}{2\pi} \int_{-\frac{\pi}{q}}^{\frac{\pi}{q}} \psi(z_2) \widehat{C}^+(q_r, z_1, z_2) \mathrm{d}z_2. \tag{6.16}$$

Equation (6.15) can only be solved analytically for a few special cases. Notably, we need to assume that the direct connectedness function C^+ remains isotropic in the z coordinates, *i.e.*, it only depends on the distance between two particles in the z direction $\widehat{C}^+(q_r, z_1, z_2) = \widehat{C}^+(q_r, |z_1 - z_2|)$. This essentially limits the use of closures to the second virial approximation only. This is, however, not a severe limitation for our model, since the second virial approximation is usually accurate for slender nanoparticles in three dimensions. Under this assumption, the remaining integral in Equation (6.15) can be seen as a convolution integral of $\widehat{C}^+(q_r, |z_1 - z_2|)$ with $\rho^{(1)}(z_3)\widehat{K}(q_r, z_3)$. Hence, we obtain

$$\begin{aligned}\widehat{\widehat{K}}(q_r, q_z) =& \widehat{\widehat{D}}^+(q_r, q_z) + \rho \widehat{\widehat{C}}^+(q_r, q_z) \widehat{\widehat{K}}(q_r, q_z) + \\ & \rho \widehat{\widehat{C}}^+(q_r, q_z) \frac{1}{2} \sum_j \Delta_j \left(\widehat{\widehat{K}}(q_r, q_z + jq) + \widehat{\widehat{K}}(q_r, q_z - jq) \right),\end{aligned} \tag{6.17}$$

or

$$\widehat{\widehat{K}}(q_r, q_z) = \frac{\widehat{\widehat{D}}^+(q_r, q_z)}{1 - \rho \widehat{\widehat{C}}^+(q_r, q_z)} + \frac{\rho \widehat{\widehat{C}}^+(q_r, q_z)}{1 - \rho \widehat{\widehat{C}}^+(q_r, q_z)} \frac{1}{2} \sum_j \Delta_j \left(\widehat{\widehat{K}}(q_r, q_z + jq) + \widehat{\widehat{K}}(q_r, q_z - jq) \right), \tag{6.18}$$

where we inserted the definition of $\rho^{(1)}(z_3)$. The form of Equation (6.18) is similar to that of the isotropic Ornstein-Zernike equation with an additional term coupling $\widehat{\widehat{K}}(q_r, q_z)$ to contributions of different wave vectors.

The definition of the mean cluster size (6.11) indicates that we only need to evaluate Equation (6.17) for $q_z = nq$ for integer values of n. This means that the Ornstein-Zernike equation is a hierarchical set of infinitely many equations in the wave vector q_z, coupled by the last term in Equation (6.17). To solve these equations, we need to truncate this hierarchy at a certain $n = n_{\max}$, which necessarily introduces some error. It can be expected, both from a physics perspective and from the definition of the mean cluster size, that all relevant information is contained in the wave vectors present in the density distribution (6.9). Hence, we choose $n_{\max}$ such that all terms present in the density distribution function (6.9) are included. We have numerically checked this assumption by setting $n_{\max}$ larger than the largest contribution in the bifurcation density. We find that the assumption is valid, as it introduces a negligible error of the order of $\mathcal{O}(10^{-6} - 10^{-3}\%)$.

6.3 The model

In order to actually use Equation (6.11) and Equation (6.17) we first need to calculate $\hat{\hat{C}}^+(q_r, q_z)$ and $\hat{\hat{D}}^+(q_r, q_z)$. Here, we employ the renormalised second virial approximation

$$C^+(1,2) = \Gamma(\eta) f^+(1,2), \tag{6.19}$$

where $\Gamma(\eta)$ is the Parsons-Lee correction term, and $f^+(1,2)$ is the connectedness Mayer f-function Both $\hat{\hat{C}}^+(q_r, q_z)$ and $\hat{\hat{D}}^+(q_r, q_z)$ are now completely determined by the connectedness criterion imposed on the particles, and by the particle shape. Here, we use the cherry-pit model for uncapped cylinders, as is schematically shown in Figure 6.1. This is a model in which particles possess a hard core as well as a connectivity shell, which defines particle connections. The size of this connectivity shell is λ_r in the radial direction and λ_z in the z-direction.

The direct connectedness function $\hat{\hat{C}}^+(q_r, q_z)$ and the auxiliary function $\hat{\hat{D}}^+(q_r, q_z)$ are derived and calculated in Appendix C, and are given by

$$\begin{aligned}\hat{\hat{C}}^+(q_r, q_z) = \Gamma(\eta) 8 v_0 j_0(q_z L) &\left[\left(1 + \frac{\lambda_r}{D}\right)^2 \frac{J_1(q_r D(1 + \frac{\lambda_r}{D}))}{\frac{1}{2} q_r D(1 + \frac{\lambda_r}{D})} - \frac{J_1(q_r D)}{\frac{1}{2} q_r D} \right] \\ &+ \Gamma(\eta) 8 v_0 \left(1 + \frac{\lambda_r}{D}\right)^2 \frac{J_1(q_r D(1 + \frac{\lambda_r}{D}))}{\frac{1}{2} q_r D(1 + \frac{\lambda_r}{D})} \left[\left(1 + \frac{\lambda_z}{L}\right) j_0 \left[q_z L \left(1 + \frac{\lambda_z}{L}\right)\right] - j_0(q_z L) \right],\end{aligned} \tag{6.20}$$

where v_0 is the volume of a single particle, j_0 is the spherical bessel function of zeroth order, J_1 is the Bessel function of first order, L is the length of a particle, D is the diameter of a particle, λ_r is the size of the connectedness shell in the radial direction and λ_z is the size of the connectedness shell in the z direction. Taking the limit $q_r, q_z \to 0$ gives

$$\hat{\hat{C}}^+(0,0) = 8 v_0 \Gamma(\eta) \left[\left(1 + \frac{\lambda_r}{D}\right)^2 - 1 + \left(1 + \frac{\lambda_r}{D}\right)^2 \frac{\lambda_z}{L} \right], \tag{6.21}$$

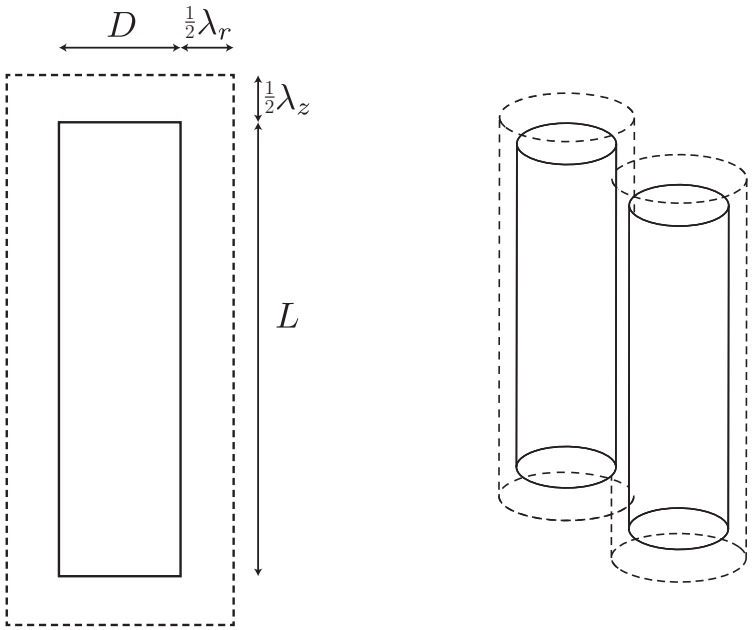

(a) (b)

Figure 6.1: (a) Schematic image of the connectedness-shell criterion. Here, D is the diameter of the cylinders and L the length. λ_r is the thickness of the connectedness shell in the radial direction and λ_z is the thickness of the connectedness shell in the z direction. (b) If the connectivity shells of the cylinders overlap, we define them to be connected.

which is equal to the volume in which two particles are connected. The auxiliary function $\hat{\hat{D}}^+(q_r, q_z)$ only needs to be evaluated for $q_z = nq$, for which it reduces to

$$\hat{\hat{D}}^+(q_r, 0) = \hat{\hat{C}}^+(q_r, 0) \tag{6.22}$$

$$\hat{\hat{D}}^+(q_r, nq) = \frac{\Delta_n}{2}\hat{\hat{C}}^+(q_r, nq) \qquad \text{for } n \geq 1. \tag{6.23}$$

With these expressions, we have all ingredients to investigate the effect of the smectic-A phase ordering on percolation.

6.4 Effects of a periodic density modulation

To investigate the effect of the onset of the smectic-A phase on percolation, we start with the zeroth order density distribution function

$$\rho^{(1)}(z) = \rho\left(1 + \Delta_1 \cos(qz)\right). \tag{6.24}$$

In this section we keep Δ_1 as an independent parameter, hence ignoring its dependence on the volume fraction η. Using the results from the previous section allows us to write Equation (6.17)

as

$$\hat{\hat{K}}(q_r,0) = \frac{\hat{\hat{C}}^+(q_r,0)}{1-\rho\hat{\hat{C}}^+(q_r,0)} + \Delta_1\rho\frac{\hat{\hat{C}}^+(q_r,0)}{1-\rho\hat{\hat{C}}^+(q_r,0)}\hat{\hat{K}}(q_r,q), \tag{6.25}$$

$$\hat{\hat{K}}(q_r,q) = \frac{\Delta_1}{2}\frac{\hat{\hat{C}}^+(q_r,q)}{1-\rho\hat{\hat{C}}^+(q_r,q)} + \frac{\Delta_1\rho}{2}\frac{\hat{\hat{C}}^+(q_r,q)}{1-\rho\hat{\hat{C}}^+(q_r,q)}\left(\hat{\hat{K}}(q_r,0)+\hat{\hat{K}}(q_r,2q)\right), \tag{6.26}$$

$$\hat{\hat{K}}(q_r,nq) = \frac{\Delta_1\rho}{2}\frac{\hat{\hat{C}}^+(q_r,n\cdot q)}{1-\rho\hat{\hat{C}}^+(q_r,nq)}\left(\hat{\hat{K}}(q_r,0(n-1)q)+\hat{\hat{K}}(q_r,(n+1)q)\right). \tag{6.27}$$

We truncate the set of equations at $n=1$, hence we set $\hat{\hat{K}}(q_r,nq)=0$ for $n>1$. The mean cluster size S can now be obtained from Equation (6.11) as

$$S = \frac{1+(\frac{\Delta_1^2}{2}-1)\rho\hat{\hat{C}}^+(0,q))}{(1-\rho\hat{\hat{C}}^+(0,0))(1-\rho\hat{\hat{C}}^+(0,q)) - \frac{1}{2}(\Delta_1\rho)^2\hat{\hat{C}}^+(0,0)\hat{\hat{C}}^+(0,q)}. \tag{6.28}$$

For $\Delta_1=0$ this reduces to the nematic mean cluster size, which diverges at $\rho_p = 1/\hat{\hat{C}}^+(0,0)$. We observe in the denominator of this equation that the point of divergence shifts for $\Delta_1\neq 0$, indicating that the smectic-A phase indeed influences the percolation threshold. The percolation threshold for this case is given by

$$\rho_p = \frac{\hat{\hat{C}}^+(0,0)+\hat{\hat{C}}^+(0,q) - \sqrt{2\Delta_1^2\hat{\hat{C}}^+(0,0)\hat{\hat{C}}^+(0,q)+\hat{\hat{C}}^+(0,q)^2 - 2\hat{\hat{C}}^+(0,0)\hat{\hat{C}}^+(0,q)+\hat{\hat{C}}^+(0,0)^2}}{2\hat{\hat{C}}^+(0,0)\hat{\hat{C}}^+(0,q) - \Delta_1^2\hat{\hat{C}}^+(0,0)\hat{\hat{C}}^+(0,q)}. \tag{6.29}$$

While this expression is not immediately insightful, the expansion close to the N-SmA phase transition $\Delta_1 \ll 1$ is. It is given by

$$\rho_p = \frac{1}{\hat{\hat{C}}^+(0,0)}\left(1-\frac{\Delta_1^2}{2}\frac{\hat{\hat{C}}^+(0,q)}{\hat{\hat{C}}^+(0,0)-\hat{\hat{C}}^+(0,q)}\right) + \mathcal{O}(\Delta_1^4), \tag{6.30}$$

where only even orders in Δ_1 are present due to symmetry. This expression is accurate only close to the N-SmA phase transition, which is also true for the density distribution we imposed Equation (6.24). Equation (6.30) shows that the onset of the smectic-A phase shifts the percolation threshold in a continuous manner, and can be written as a perturbation on the percolation threshold in the nematic phase. Since $\hat{\hat{C}}^+(0,0) > \hat{\hat{C}}^+(0,q)$ for all $q\neq 0$, the shift to higher or lower densities is completely dependent on the sign of $\hat{\hat{C}}^+(0,q)$. In the slender rod limit, where the connectivity shell size $\lambda_z/L\to 0$, the influence of the smectic-A phase is fully captured within the wave vector Q as

$$\frac{\hat{\hat{C}}^+(0,q)}{\hat{\hat{C}}^+(0,0)-\hat{\hat{C}}^+(0,q)} = \frac{\sin Q}{Q-\sin Q}, \tag{6.31}$$

where $Q = qL$. This constant is approximately -0.178 for the critical density modulation Q^* which indicates that the smectic-A phase transition inhibits percolation in the slender rod limit. We note that this dependence on Q only holds for all orders in Δ_1 in Equation (6.30). Whether it is possible that the onset of the smectic-A phase destroys a percolating cluster that was present in the nematic phase is now fully dependent on the density dependence of Δ_1, which we discuss in a later point in this report, in section 6.5.

For finite aspect ratios, we expect Equation (6.29) to be dependent on both shell sizes λ_r/D and λ_z/L and the wave vector Q. In Figure 6.2 we plot $\hat{\hat{C}}^+(0,q)/(\hat{\hat{C}}^+(0,0) - \hat{\hat{C}}^+(0,q))$ as a function of both connectivity shell sizes, indicating the shift in the percolation threshold. Here, we observe that the connectivity shell size λ_z/L has a large influence on the shift of the percolation threshold, whereas the effect of λ_r/D is limited. Only for $\lambda_r/D \ll 1$, the influence is non-negligible. The oscillatory behaviour as function of λ_z indicates that percolation-inhibiting or -facilitating effects can be tuned by tuning λ_z/L. This effect is quite intuitive, and relies solely on the average number of particles a test particle at position $\vec{r}_1$ is directly connected to. For a homogeneous density model, a test particle at position $\vec{r}_1$ can be connected with a particle at position $\vec{r}_2$ in its connectivity shell, and the weight of this connection is proportional to the density. In the smectic-A phase this weight associated with the connection is still proportional to the density, but the density is now a local, not a global, property. If the average density in the connectivity shell is higher than the average density in a nematic reference fluid at the same global density, we expect that the formation of a percolation network is more likely. The reverse is identically true. That this holds is best observed in the ideal particle limit (*i.e.*, for $\lambda_r/D \to \infty$). Here, this average connectivity argument translates to the condition that the total particle size $L + \lambda_z$ is equal to the wavelength for the effect of the density modulation to be completely compensated. The periodicity of the smectic-A layers is given by $\frac{2\pi}{q} \approx 1.39L$ for uncapped cylinders[1]. Therefore it is expected that the percolation threshold is shifted to lower densities for $\frac{\lambda_z}{L} > 0.39$, as compared to the a nematic reference fluid. This transitions between percolation-inhibiting and -facilitating effects can be extracted from the condition

$$\frac{\hat{\hat{C}}^+(0,q)}{\hat{\hat{C}}^+(0,0) - \hat{\hat{C}}^+(0,q)} = 0. \tag{6.32}$$

The first of these transition lines is given by

$$\frac{\lambda_z}{L} = \frac{2\pi}{Q} - 1 + \frac{1}{Q}\arcsin\left[\frac{\sin(Q)}{(1+\frac{\lambda_r}{D})^2}\right], \tag{6.33}$$

where Q is the smectic-A wave vector. The asymptote $\frac{\lambda_r}{D} \to \infty$ is given by $\frac{\lambda_z}{L} = \frac{2\pi}{Q} - 1$, or $\lambda_z + L = \frac{2\pi}{Q}L$. This is in agreement with our expectation that the average connectivity is the key control parameter for the smectic-A phase. For non-negligible hard core diameter of the particles, the transition occurs at smaller shell size λ_z/L. Apparently, the presence of the hard core increases the effect that λ_z/L has on the percolation threshold.

[1]For capped cylinders, the periodicity obtained by Monte Carlo simulations is $\frac{2\pi}{q} \approx 1.23L$ for $L/D = 5$, and limits to $\frac{2\pi}{q} \approx 1.27L$ in the infinite aspect ratio limit [81].

If we increase λ_z/L beyond the first maximum in Figure 6.2, a competition is entered where the larger connectivity shell is compensated by the presence of low-density regions or enhanced by high-density regions. Apparently, the additional connection with a low-density region can largely counteract the effect of high-density region, which is in agreement with the average connectivity argument. Here, we observe regions where the smectic-A phase shifts the critical density to higher densities, effectively blocking percolation. These connectivity sizes, however, are largely unphysical as, for example, the distance between carbon nanotubes to facilitate electron hopping is much smaller than the linear size L of the particles. Therefore only effects associated with $\lambda_z/L \ll 1$ are physically relevant.

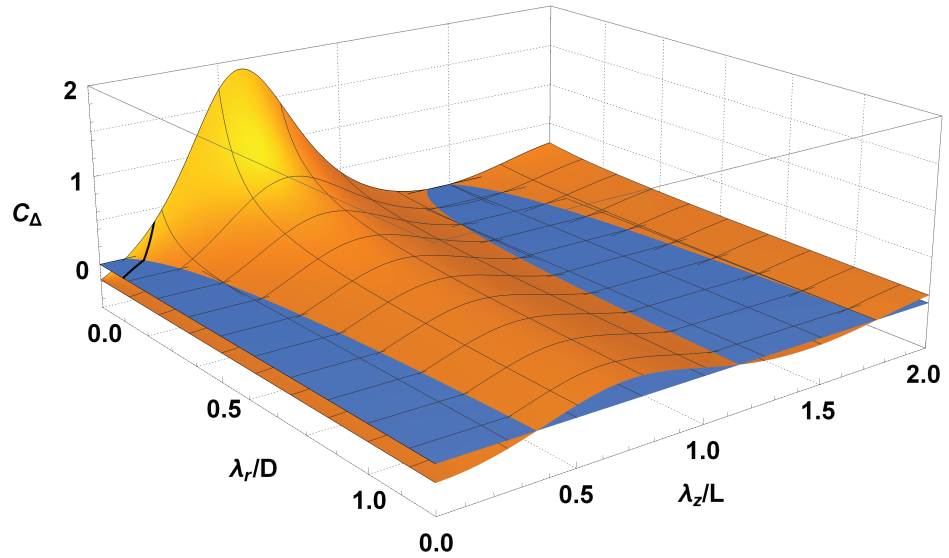

Figure 6.2: Orange: A plot of $C_\Delta = \widehat{C}^+(0,q)/(\widehat{C}^+(0,0) - \widehat{C}^+(0,q))$ as a function of the connectedness shell sizes λ_r/D and λ_z/L. Blue: surface indicating $C_\Delta = 0$. For $C_\Delta < 0$, the percolation threshold shifts to higher densities, whereas for $C_\Delta > 0$ the percolation threshold shifts to lower densities. The black curve corresponds to the minimum values of λ_z/L and λ_r/D to have percolation at the critical density of the smectic-A phase transition $\eta_c \approx 0.338$.

6.5 Percolation in the smectic-A phase

In the previous section, we have investigated the effects of the onset of the smectic-A phase by inspecting the $\Delta_1 \ll 1$ limit. We have used Δ_1 as a free parameter for simplicity, but it is, in fact, a function of the volume fraction η. In this section we investigate the effect of including the density dependency on Δ_1 on percolation in the smectic-A phase. The density dependency of Δ_1 is introduced at the level of the second order bifurcation, and is therefore not exact. A more accurate description can be obtained by developing the bifurcation analysis of chapter 5 to higher orders. To investigate the effects of the onset of the smectic-A phase, we investigate the minimum connectivity-shell thickness in both directions, λ_r/D and λ_z/L, that enables percolation.

Percolation threshold

In Figure 6.3a, we plot the percolation threshold in terms of the minimum required λ_z/L as a function of λ_r/D for $\eta = 0.34$, for both the smectic-A phase and the nematic reference fluid. The N-SmA phase transition occurs at $\eta = 0.338$ for our model. As predicted in the previous section, we observe both percolation-inhibiting and percolation-facilitating effects. For small values of λ_z/L, the smectic-A phase makes the formation of a percolation network slightly more difficult, whereas for larger sizes of this shell, it makes the formation of a percolating network slightly easier. In Figure 6.3b we plot a similar diagram, only at a higher volume fraction $\eta = 0.365$, where $\Delta_1 \approx 1$. Here, we observe the same qualitative behaviour as in the lower density case, though the effect is more pronounced. Even though the effect of the smectic ordering is noticeable, it is relatively small compared with the effect of the isotropic-nematic phase transition [62].

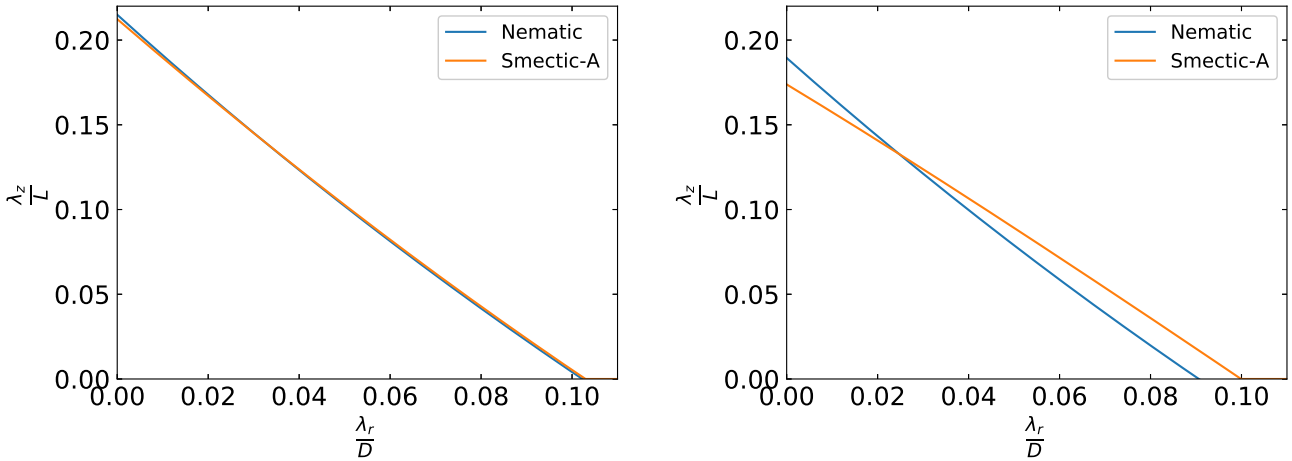

(a) $\eta = 0.34$ (b) $\eta = 0.365$

Figure 6.3: The minimum required connectivity shell for percolation in the smectic-A phase and a perfectly aligned nematic phase. No percolation is present below the curves, while a percolating particle cluster is present above the curves.

While this indicates that in the smectic-A phase the connectivity shell λ_z can be used to switch between percolation-inhibiting and percolation-facilitating effects, the large difference in shell sizes necessary to switch between these effects are unphysical. Under the assumption that $\lambda_z \approx \lambda_r$, the aspect ratio L/D of the particles becomes important. The actual size of λ_z and λ_r is dependent on the electron tunnelling length, or the Debye-length in charge-stabilised suspensions [87]. We have found no literature that discusses whether λ_z and λ_r are different, but it is reasonable to assume that these length scales are of the same order of magnitude. As we have shown in Figure 6.3, the smectic-A phase only facilitates percolation if $\lambda_z/L \gg \lambda_r/D$. Hence for $L/D > 1$ we expect, *a priori*, that the effect of the smectic ordering is limited to inhibiting the formation of a percolating network. In Figure 6.4, we plot the percolation threshold in terms of the connectivity shell λ/D, where $\lambda_r = \lambda_z = \lambda$, as a function of the volume fraction η of the nanoparticles for various aspect

ratios L/D for the smectic-A phase and the nematic reference fluid. Indeed we find that for all plotted aspect ratios the minimum shell size is larger in the smectic-A phase, as compared to the nematic phase. Still, it remains a monotonically decreasing function for $\eta \geq \eta_c$. The connectivity shell λ/D is continuous at the N-SmA phase transition, indicating that the smectic ordering does not destroy a percolating network that is already formed in the nematic phase. It is likely, however, that the cluster structure in the smectic-A phase significantly deviates from that in the nematic phase, which we investigate in the next section.

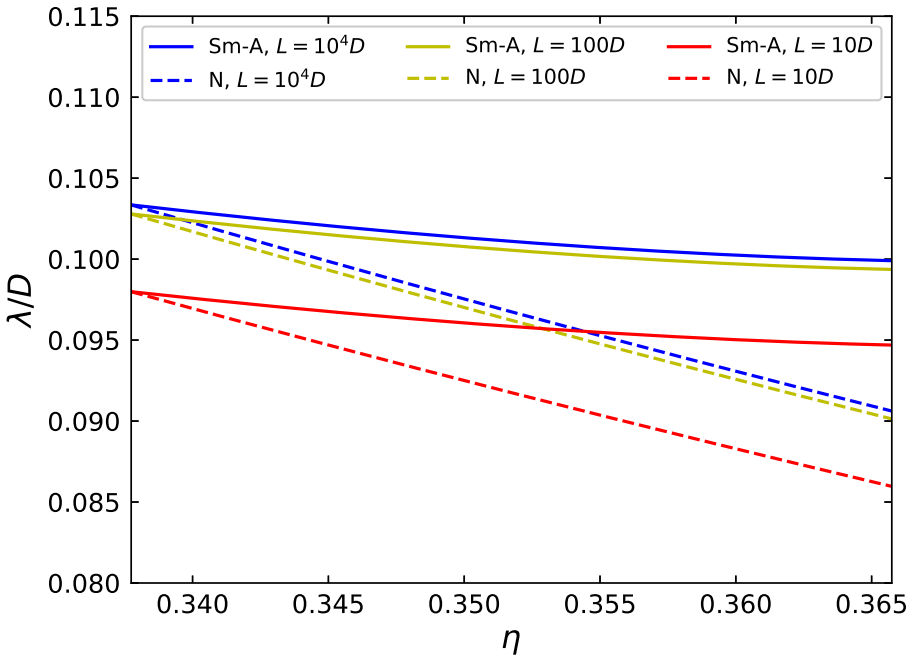

Figure 6.4: The percolation threshold in terms of the minimum required shell size λ/D for various values of the aspect ratio L/D. We include data for the smectic-A phase, and a nematic reference fluid.

Correlation length

The physical dimensions of the cluster can be probed via the correlation lengths ζ_r, perpendicular to the nematic director, and ζ_z, parallel to the nematic director. If the density modulation is sharply peaked in the smectic-A phase, it might be possible that an infinitely large cluster has formed in the radial direction, while it remains finite in the other direction. The mean cluster size S is too crude of a measure to extract information on the physical cluster dimension, as any cluster consisting of an infinitely many particles (in any direction) causes the mean cluster size S to diverge. The correlation length within the smectic layers ζ_r and the correlation length scale along the nematic director ζ_z, however, might contain this information. It is possible that the cluster grows differently perpendicular or parallel to the nematic director, *i.e.*, the critical exponents of the correlation length $\nu_\perp$ and $\nu_\parallel$ are different. We do note that a discrete layered model has been investigated by Dayan *et al.* [88], who found that $\nu_\perp$ and $\nu_\parallel$ are different only for a random

multilayer model, where each layer had a random site density. The correlation lengths can be extracted from the $\vec{q}$-dependent mean cluster size $S(q_r, q_z)$ in the small $\vec{q}$ limit, by writing it in a Lorentzian form as

$$S(q_r, q_z) = \frac{S}{1 + \zeta_r^2 q_r^2 + \zeta_z^2 q_z^2}, \tag{6.34}$$

where ζ_r is the correlation length in the radial direction and ζ_z is the correlation length in the direction parallel to the rods [62].

Unfortunately, the method outlined in this report does not allow for the possibility to extract the parallel correlation length ζ_z. In our derivation of the inhomogeneous mean cluster size S, we have pre-averaged the position over a single particle z_1, while keeping the other particle fixed at z_2. In order to calculate the correlation length ζ_z, information about $z = |z_1 - z_2|$ is necessary. Therefore we only discuss the correlation length scale perpendicular to the nematic director ζ_r, as it can be obtained straightforwardly. The radial correlation length ζ_r is averaged over one smectic-A layer, and can for the zeroth order density distribution be obtained analytically as

$$\left(\frac{\zeta_r}{D}\right)^2 = f(\eta, \lambda_r, \lambda_z) S, \tag{6.35}$$

where $f(\eta, \lambda_r, \lambda_z)$ is a complicated function dependent on η, λ_r and λ_z, see Appendix C. This function itself diverges if

$$\left[1 - 4\left(\Delta_1^2 - 2\right)\eta\Gamma(\eta)\left(j_0(Q) - (\lambda_r + 1)^2(\lambda_z + 1) j_0((\lambda_z + 1)Q)\right)\right]^2 = 0. \tag{6.36}$$

The divergence only occurs at a volume fraction above the percolation threshold, hence the cluster size diverges at the percolation threshold according to $\zeta_r \sim \sqrt{S}$ with the critical exponent of $\nu_\perp = \frac{1}{2}$.

We have plotted the correlation length ζ_r/D in Figure 6.5 for two parameter choices of λ_r and λ_z, to illustrate the change in growth caused by the nematic-smectic phase transition. The blue line indicates the correlation length for a nematic reference fluid. The growth of the correlation length does change suddenly at the nematic-smectic transition, but diverges similarly to the nematic correlation length. Hence, aside from the shift in the percolation threshold, the smectic-A phase does not functionally change the lateral growth of the cluster as measured by ζ_r.

Second order density distribution

While we have used the simple zeroth-order density distribution up to this point, we have ignored two key-aspects that can have a significant effect on the percolation threshold. First of all, we have neglected the change of the smectic wave vector Q as a function of the density. Secondly, the peaks in the density distribution become sharper with increasing density, which influences the average number of particles that a random test particle is connected to. We investigate the effects of these simplifications in this section. While the mean cluster size S can still be obtained

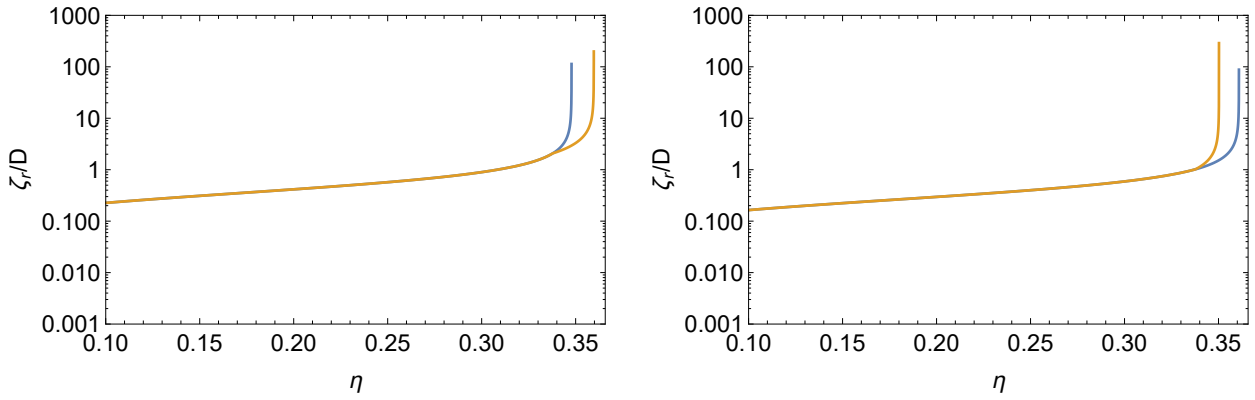

(a) $\lambda_r/D = 0.065$, $\lambda_z/L = 0.065$ (b) $\lambda_r/D = 0.001$, $\lambda_z/L = 0.18$

Figure 6.5: The radial correlation length scale ζ_r as a function of the volume fraction η for two different choices of connectivity shell sizes. Blue: nematic reference fluid. Orange: the correlation length for a nematic fluid for $\eta < \eta_c$ and a smectic fluid for $\eta > \eta_c$. At the N-SmA phase transition, the correlation length, and therefore the lateral dimension, changes continuously.

analytically, it becomes intractable for a second and higher order density expansion. Hence, we have used Mathematica to solve for the mean cluster size S. It is reasonable to expect that the first order term Δ_2 is non-negligible for $\Delta_1 \to 1$, as it is only one order of magnitude smaller than the zeroth order term. The second order term is two orders of magnitude smaller than the zeroth order term and is therefore likely negligible.

As shown in Figure 6.6, however, the effect of including higher order terms in the density distribution function $\rho^{(1)}(z_1)$ is negligible. Here we have included the nematic reference fluid, as well as the zeroth, first and second order smectic density distribution. Minor differences emerge only for $\eta \approx 0.365$ as shown in Figure 6.6a. In Figure 6.6b, we zoom in on a specific part of this diagram. The first and second order density distribution curves are indistinguishable, while the zeroth order density expansion only predicts a slightly higher percolation threshold. The crossing point with the nematic reference fluid is slightly shifted due to the shift in the wave vector Q. Hence the effect of the smectic-A ordering on percolation is, at least close to the phase transition, almost completely captured within the zeroth order density distribution and only weakly dependent on the exact shape of the distribution.

We plot the percolation threshold in form of the required connectedness shell size under the assumption that $\lambda_r = \lambda_z = \lambda$ in Figure 6.7. Here, the nematic reference fluid, the zeroth order density distribution and the second order density distribution curves are included for $L/D = 100$. Indeed, we find that the zeroth order density distribution accurately describes the effect of the smectic-A phase over the whole plot range, and higher order contributions emerge only for $\Delta_1 \to 1$.

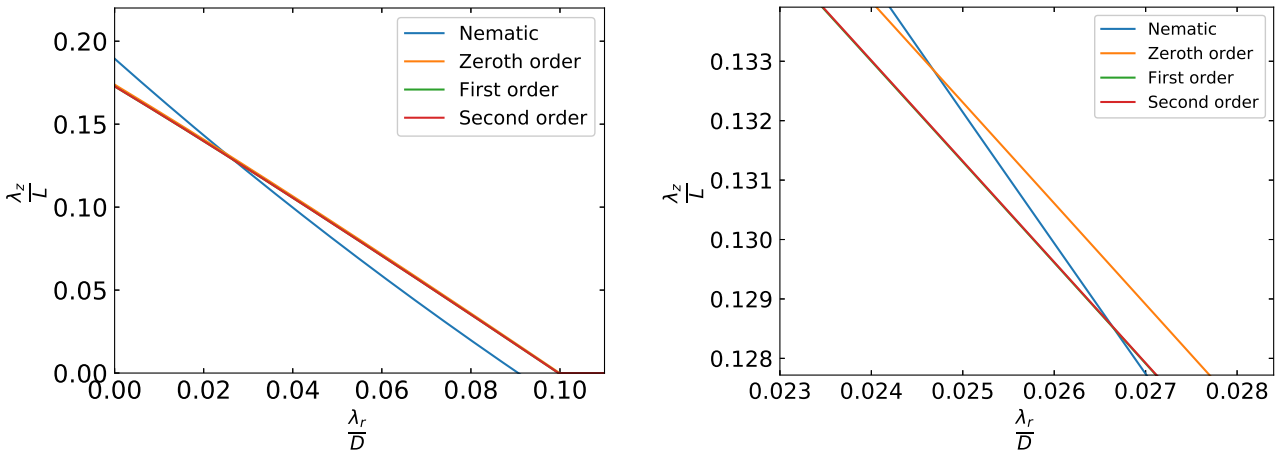

(a) (b)

Figure 6.6: (a) The percolation threshold in terms of the minimum connectivity shell for $\eta = 0.365$. Here, we include a nematic reference fluid and the smectic-A fluid, using the zeroth, first and second order density distributions. (b) Same as (a), zoomed in to illustrate the difference between the zeroth order and first or second order density distribution functions.

6.6 Deeper in the smectic-A phase

Up to now we have only considered the effect of smectic-A ordering near the phase transition where the bifurcation expansion for $\rho^{(1)}(z)$ is valid. Although the main effect of the smectic-A phase is captured, a significant non-zero density is present everywhere. Deeper in the smectic-A phase this is no longer true, and the high density regions are alternated by regions with near zero density [80, 81]. These regions of zero or near zero density can, in fact, have a significant influence on the percolation properties. If the contact between two high density regions is nearly impossible, cluster formation can essentially become an in-layer phenomena only. If this layer is small enough, the in-layer cluster formation behaves as in a quasi-two-dimensional model.

To inspect the effect of sharply peaked layers with zero or near-zero density between the layers, we employ a delta-wave density distribution function $\rho^{(1)}(z) = \rho\psi(z)$, where $\psi(z)$ is given by

$$\psi(z) = \sum_{l=1}^{n} \alpha\delta(z - l\alpha). \tag{6.37}$$

Here α is the inter-layer spacing, or lattice constant, which is equivalent to $\alpha = \frac{2\pi}{q}$, as shown in Figure 6.8. This density distribution function effectively transforms our model into combined a lattice-continuum model. Here, it is a continuum percolation model in two-dimensional planes, which are connected to other planes in a lattice-like fashion. Hence, it is convenient to fully rewrite the mean cluster size S and the Ornstein-Zernike equation in lattice-continuum form, see Appendix G for details. We employ the second virial approximation, equivalent to the approximation we have employed in the previous parts of this chapter. Under appropriate conditions we

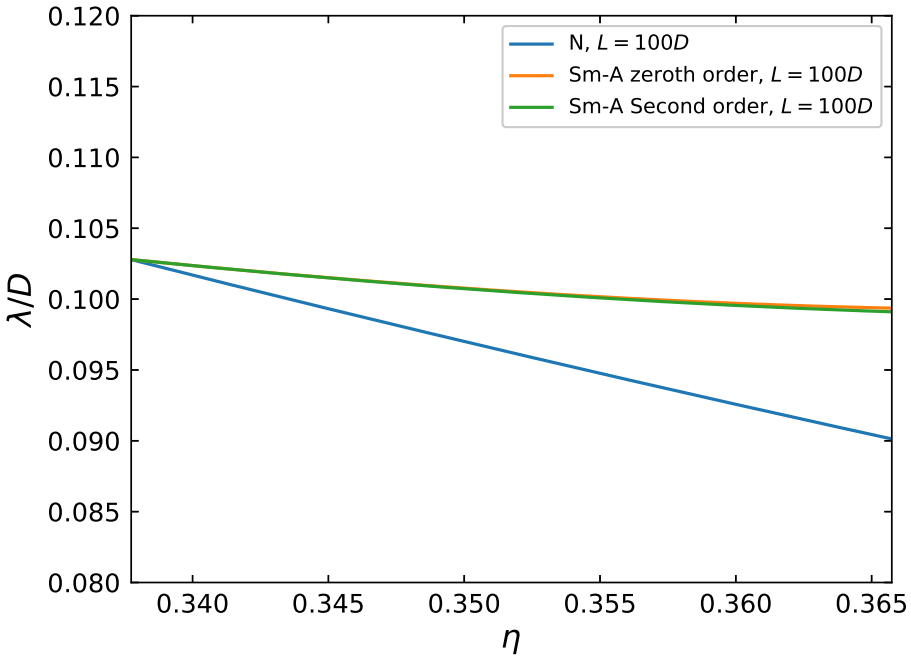

Figure 6.7: The effect of higher order terms in the density modulation of the smectic-A phase transition for the aspect ratio $L/D = 100$. We observe only a small difference for η near the volume fraction where the bifurcation analysis breaks down.

can obtain the mean cluster size S in the thermodynamic limit as

$$S = \frac{1}{1 - \rho\alpha\left(\widehat{C}^{+}(0,0) + 2\widehat{C}^{+}(0,\alpha)\right)}, \tag{6.38}$$

where we note that due to the lattice-like structure in the z direction, the direct connectedness function $\widehat{C}^{+}(0,\alpha)$ is only Fourier transformed in one direction. The z direction depends on the lattice spacing only, hence $\widehat{C}^{+}(0,0)$ represents the direct connectedness function within a layer, whereas $\widehat{C}^{+}(0,\alpha)$ represents the direct connectedness function between layers. For hard cylinders the dependence of these functions on α is limited to an discontinuous 'on/off'-switch of the connections between layers. For a model with capped spherocylinders this on/off-switch is continuous. In absence of inter-layer connections, the mean cluster size is simply the two-dimensional mean cluster size S. In this case, we obtain percolation inside each layer, while no percolating cluster is present between layers. For the uncapped cylinder model, the change in the inter-layer spacing results in a discontinuous change in the mean cluster size, where we can instantaneously transition from no percolation to percolation. This means that if connections between neighbouring planes are present, $\widehat{C}^{+}(0,\alpha)$ is a constant, independent of α. For capped cylinders, this is not the case, as the end caps overlap first, causing this transition to be continuous. Similarly to the fully continuous model described in the previous sections, we are unable to extract the correlation length parallel to the nematic director.

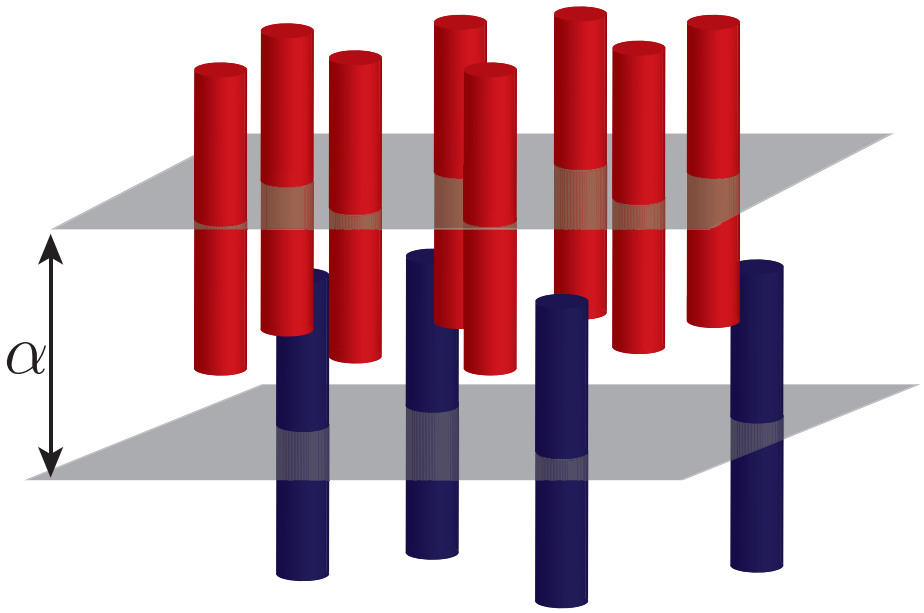

Figure 6.8: Schematic view of the delta-wave density distribution model. The centres of mass of the particles are positioned perfectly within the planes. The distance between the planes is predefined as α.

One interesting possibility of the delta-wave approach is that it enables us to inspect the effect of a finite number of connected planes. Moreover, a simple closed-form expression for the mean cluster size S, as a function of the total number of included planes k, can be obtained [89]. This finite-layer mean cluster size is given by

$$S = \frac{1}{1 - \rho\alpha \left(\widehat{C}^{+}(0,0) + 2\cos\left(\frac{1}{k+1} \cdot \pi\right) \widehat{C}^{+}(0,1) \right)}, \tag{6.39}$$

where $k \geq 2$ is the number of planes in the model. Indeed, the infinite layer mean cluster size Equation (6.38) is obtained in the limit $k \to \infty$. Equation (6.39) predicts that the percolation threshold ρ_p is dependent on all layers via

$$\rho_p \alpha = \frac{1}{\widehat{C}^{+}(0,0) + 2\cos\left(\frac{1}{k+1} \cdot \pi\right) \widehat{C}^{+}(0,1)}. \tag{6.40}$$

This does actually suggest that the infinite cluster that appears at the percolation threshold, is also infinite in size in the z-direction. If the cluster remained finite in the z direction at the percolation threshold, we should be able to obtain an infinite cluster in the centre of the model, which should remain unaffected by minor changes at the z-boundaries. The fact that this is not the case suggests that the cluster must become infinitely large in all directions.

Chapter 7

Conclusion

In the first part of this thesis, we have investigated the Percus-Yevick closure for connectedness percolation theory in two dimensions. We have applied the Percus-Yevick closure in two dimensions both for ideal and cherry-pit disk particles, as well as for ideal anisometric particles. While analytical results can be obtained in odd dimensions, this is not true for even dimensions. Hence we have used a direct numerical evaluation of the governing equations to obtain a solution for the Percus-Yevick closure. We found that the Percus-Yevick closure for connectedness percolation is accurate for low densities, but inaccurate at high densities for all particle models. The Percus-Yevick closure does not predict a percolation threshold within the density range that we have investigated. For the cherry-pit model for disks, we have found that the Percus-Yevick closure appears to become inconsistent at lower densities than the percolation threshold.

The apparent breakdown of the Percus-Yevick closure in two dimensions, where the pair connectedness function becomes locally negative, has, to our knowledge, not been reported before. This breakdown of Percus-Yevick theory for cherry-pit disks is a second indicator that Percus-Yevick cannot be used to obtain meaningful results for percolation at high densities in two dimensions. For anisometric ideal particles in two dimensions, we find a similar exponential scaling behaviour in the mean cluster size as for ideal disk particles. We have compared our pair connectedness functions with those available from Monte Carlo simulations and find remarkable quantitative agreement at low densities, while at high densities the agreement is only qualitative. Similarly, excellent agreement is found for the angular dependent pair connectedness function at low densities. We have shown that an effective density rescaling is accurate. An extrapolation of this scaling indicates that the equations need to be solved up to infinite density to get arbitrarily close to the percolation threshold, which limits the practical usability of this method. Hence, the Percus-Yevick closure is not well-suited to describe percolation in two dimensions, and the second virial approximation turns out to be more accurate.

In the second part of this thesis, we have investigated the effect of the smectic-A ordering of perfectly aligned nanoparticles on percolation in three dimensions. We have derived the density distribution function via density functional theory using a bifurcation analysis, and derived an method to calculate its effect on percolation. We have used a renormalised second virial closure

to compensate for both the effect of finite aspect ratios and the perfect alignment of the particles. The two important control parameters are the connectivity shell size along the nematic director and the wavelength of the smectic-A phase. We have indicated that, within the region in which the bifurcation analysis is accurate, the zeroth order bifurcation expansion completely captures the effect of the smectic-A phase on percolation. While we have been able to obtain the correlation length in the in-layer direction, our method fails to predict the correlation length in the direction along the nematic director. It remains an open question what the physical dimensions of a cluster in the smectic phase are.

At higher densities the smectic density distribution becomes sharply peaked, and a bifurcation analysis does no longer suffice. We have investigated this limit by assuming perfectly localised layers. The percolation threshold is then governed by the connections inside each layer and to neighbouring layers. We have indicated that the percolation threshold for a finite number of layers depends on the total number of layers in the model, suggesting that the correlation length at the percolation threshold in the thermodynamic limit is the same within and perpendicular to the layers. In general, we can conclude that close to the smectic-A phase transition, ordering of the smectic-A phase inhibits the formation of a percolating cluster, but does not destroy an already present cluster.

Chapter 8

Outlook

The Percus-Yevick closure is not well suited to describe percolation in two dimensions. More closures exists with various degrees of complexity. In section 4.5, we have already briefly introduced two possible routes to improve upon the Percus-Yevick closure. In the future, we believe that the PY-d closure is likely the easiest to implement numerically, at least for ideal disk particles.

On the topic of the smectic-A phase, significant work is still necessary. Since we were unable to obtain an expression for the correlation length along the nematic director, we are not able to inspect the change in cluster dimensions in the direction along the director. In the future, methods put forward in Jaiswal *et al.* [90] might be of use to solve this deficiency of our method. Furthermore, we have limited our investigation of the effects of the smectic-A ordering on percolation close to the phase transition and very deep in the smectic phase (with the delta-wave model) only. As the positional ordering increases significantly deeper in the smectic-A phase, it is to be expected that the influence of the wave vector and the connectivity shell in the direction along the nematic director increase. Lastly, we have limited our investigation to a relatively simple model of perfectly aligned cylinders. This can be extended to a more realistic description of the smectic-A phase, which also includes effects as orientational freedom, end-caps and the presence of inter-layer particles. We note that the description of the smectic-A phase is found to be quite sensitive to coupling between orientational and positional degrees of freedom. The sensitivity of the onset of percolation in the smectic-A phase on the wave vector Q, indicates that especially the dependence of Q on the end caps can have significant implications for the conclusions, especially at small aspect ratios. Secondly, it has been predicted that the columnar phase pre-empts the smectic-A phase in certain slender nanoparticles [64]. Hence our method could be extended to investigate this phase as well.

Finally, our theoretical method also provides the possibility to study finite size systems by using a density modulation that behaves as a block-wave, *i.e.*, a density modulation representing periodically spaced layers of finite thickness, where the spacing (and density) between the layers is appropriately chosen to prevent interactions between separate layers. This might especially be useful for the investigation of thin films, as standard methods for connectedness percolation seem to be inaccurate in two dimensions. Whether it is actually feasible to study these finite size models with our newly proposed method remains to be seen.

Bibliography

[1] B. J. Landi, M. J. Ganter, C. D. Cress, R. A. DiLeo, and R. P. Raffaelle. Carbon nanotubes for lithium ion batteries. *Energy & Environmental Science*, 2(6):638, 2009. doi:10.1039/b904116h.

[2] C. S. Boland, U. Khan, G. Ryan, S. Barwich, R. Charifou, A. Harvey, C. Backes, Z. Li, M. S. Ferreira, M. E. Mobius, R. J. Young, and J. N. Coleman. Sensitive electromechanical sensors using viscoelastic graphene-polymer nanocomposites. *Science*, 354(6317):1257–1260, 2016. doi:10.1126/science.aag2879.

[3] P. H. Lau, K. Takei, C. Wang, Y. Ju, J. Kim, Z. Yu, T. Takahashi, G. Cho, and A. Javey. Fully Printed, High Performance Carbon Nanotube Thin-Film Transistors on Flexible Substrates. *Nano Letters*, 13(8):3864–3869, 2013. doi:10.1021/nl401934a.

[4] A. V. Kyrylyuk, M. C. Hermant, T. Schilling, B. Klumperman, C. E. Koning, and P. van der Schoot. Controlling electrical percolation in multicomponent carbon nanotube dispersions. *Nature Nanotechnology*, 6(6):364–369, 2011. doi:10.1038/nnano.2011.40.

[5] M. H. Andrew Ng, L. T. Hartadi, H. Tan, and C. H. Patrick Poa. Efficient coating of transparent and conductive carbon nanotube thin films on plastic substrates. *Nanotechnology*, 19(20):205703, 2008. doi:10.1088/0957-4484/19/20/205703.

[6] D. S. Hecht, D. Thomas, L. Hu, C. Ladous, T. Lam, Y. Park, G. Irvin, and P. Drzaic. Carbon-nanotube film on plastic as transparent electrode for resistive touch screens. *Journal of the Society for Information Display*, 17(11):941, 2009. doi:10.1889/JSID17.11.941.

[7] S. P. Finner, M. I. Kotsev, M. A. Miller, and P. van der Schoot. Continuum percolation of polydisperse rods in quadrupole fields: Theory and simulations. *The Journal of Chemical Physics*, 148(3):034903, 2018. doi:10.1063/1.5010979.

[8] R. H. J. Otten. *Self-organisation of anisometric particles: statistical theory of shape, confinement and external-field effects*. Phd, 2011.

[9] T. Drwenski, R. van Roij, and P. van der Schoot. Connectedness percolation of hard convex polygonal rods and platelets. *The Journal of Chemical Physics*, 149(5):054902, 2018. doi:10.1063/1.5040185.

[10] T. Drwenski, S. Dussi, M. Dijkstra, R. van Roij, and P. van der Schoot. Connectedness percolation of hard deformed rods. *The Journal of Chemical Physics*, 147(22):224904, 2017. doi:10.1063/1.5006380.

[11] Y.-B. Yi, C.-W. Wang, and A. M. Sastry. Two-Dimensional vs. Three-Dimensional Clustering and Percolation in Fields of Overlapping Ellipsoids. *Journal of The Electrochemical Society*, 151(8):A1292, 2004. doi:10.1149/1.1769272.

[12] P. Bult. *Percolation of penetrable lines in two dimensions*. Bachelor thesis, Eindhoven University of Technology, 2017.

[13] I. Balberg, C. H. Anderson, S. Alexander, and N. Wagner. Excluded volume and its relation to the onset of percolation. *Physical Review B*, 30(7):3933–3943, 1984. doi:10.1103/PhysRevB.30.3933.

[14] Y. Y. Tarasevich and A. V. Eserkepov. Percolation of sticks: Effect of stick alignment and length dispersity. *Physical Review E*, 98(6):062142, 2018. doi:10.1103/PhysRevE.98.062142.

[15] S. Mertens and C. Moore. Continuum percolation thresholds in two dimensions. *Physical Review E*, 86(6):061109, 2012. doi:10.1103/PhysRevE.86.061109.

[16] A. Coniglio, U. De Angelis, and A. Forlani. Pair connectedness and cluster size. *Journal of Physics A: General Physics*, 10(7):1123–1139, 1977. doi:10.1088/0305-4470/10/7/011.

[17] X. Xiao and P. Sheng. Generalized Onsager theory of liquid crystals. *Physical Review E*, 88(6):062501, 2013. doi:10.1103/PhysRevE.88.062501.

[18] R. Wittmann, C. E. Sitta, F. Smallenburg, and H. Löwen. Phase diagram of two-dimensional hard rods from fundamental mixed measure density functional theory. *The Journal of Chemical Physics*, 147(13):134908, 2017. doi:10.1063/1.4996131.

[19] J.-P. Hansen and I. R. McDonald. Inhomogeneous Fluids. In *Theory of Simple Liquids*, pages 203–264. 2013. doi:10.1016/B978-0-12-387032-2.00006-4.

[20] G. Tarjus, P. Viot, S. Ricci, and J. Talbot. New analytical and numerical results on virial coefficients for 2-D hard convex bodies. *Molecular Physics*, 73(4):773–787, 1991. doi:10.1080/00268979100101541.

[21] M. A. Miller. Private Communication. 2019.

[22] E. M. Sevick and P. A. Monson. Cluster integrals for square well particles: Application to percolation. *The Journal of Chemical Physics*, 94(4):3070–3082, 1991. doi:10.1063/1.459830.

[23] S. Varga and I. Szalai. Parsons-Lee theory and a simulation-based study of two-dimensional hard-body fluids. *Journal of Molecular Liquids*, 85(1-2):11–21, 2000. doi:10.1016/S0167-7322(99)00160-9.

[24] Y. C. Chiew and E. D. Glandt. Percolation behaviour of permeable and of adhesive spheres. *Journal of Physics A: Mathematical and General*, 16(11):2599–2608, 1983. doi:10.1088/0305-4470/16/11/026.

[25] T. DeSimone, S. Demoulini, and R. M. Stratt. A theory of percolation in liquids. *The Journal of Chemical Physics*, 85(1):391–400, 1986. doi:10.1063/1.451615.

[26] J. Xu and G. Stell. An analytic treatment of percolation in simple fluids. *The Journal of Chemical Physics*, 89(2):1101–1111, 1988. doi:10.1063/1.455217.

[27] C. M. Carlevaro, L. Blum, and F. Vericat. Generalized mean spherical approximation for a model of water with dipole, quadrupole, and short-range potential of tetrahedral symmetry. *The Journal of Chemical Physics*, 119(10):5198–5215, 2003. doi:10.1063/1.1597475.

[28] S. Maran and L. Reatto. Integral equations for continuum percolation. *The Journal of Chemical Physics*, 89(8):5038–5043, 1988. doi:10.1063/1.455648.

[29] J. A. Given and W. Klein. Born-bogoliubov-green-kirkwood-yvon hierarchy for continuum percolation. *Physical Review B*, 38(16):11874–11877, 1988. doi:10.1103/PhysRevB.38.11874.

[30] J. A. Given and W. Klein. Born-Green hierarchy for continuum percolation. *The Journal of Chemical Physics*, 90(2):1116–1127, 1989. doi:10.1063/1.456166.

[31] S. Torquato and Y. Jiao. Effect of dimensionality on the continuum percolation of overlapping hyperspheres and hypercubes. II. Simulation results and analyses. *The Journal of Chemical Physics*, 137(7):074106, 2012. doi:10.1063/1.4742750.

[32] R. Ishizuka, S.-H. Chong, and F. Hirata. An integral equation theory for inhomogeneous molecular fluids: The reference interaction site model approach. *The Journal of Chemical Physics*, 128(3):034504, 2008. doi:10.1063/1.2819487.

[33] M. S. Wertheim. Exact Solution of the Percus-Yevick Integral Equation for Hard Spheres. *Physical Review Letters*, 10(8):321–323, 1963. doi:10.1103/PhysRevLett.10.321.

[34] R. J. Baxter. Percus-Yevick Equation for Hard Spheres with Surface Adhesion. *The Journal of Chemical Physics*, 49(6):2770–2774, 1968. doi:10.1063/1.1670482.

[35] M. Adda-Bedia, E. Katzav, and D. Vella. Solution of the Percus-Yevick equation for hard disks. *The Journal of Chemical Physics*, 1281(10):184508–144506, 2008. doi:10.1063/1.2919123.

[36] M. Adda-Bedia, E. Katzav, and D. Vella. Solution of the Percus-Yevick equation for hard hyperspheres in even dimensions. *The Journal of Chemical Physics*, 129(14):144506, 2008. doi:10.1063/1.2991338.

[37] E. Leutheusser. Exact solution of the Percus-Yevick equation for a hard-core fluid in odd dimensions. *Physica A: Statistical Mechanics and its Applications*, 127(3):667–676, 1984. doi:10.1016/0378-4371(84)90050-5.

[38] S. Torquato. *Random Heterogeneous Materials*. 2002. doi:10.1007/978-1-4757-6355-3.

[39] Z. W. Salsburg, R. W. Zwanzig, and J. G. Kirkwood. Molecular Distribution Functions in a OneDimensional Fluid. *The Journal of Chemical Physics*, 21(6):1098–1107, 1953. doi:10.1063/1.1699116.

[40] A. Drory. Exact solution of a one-dimensional continuum percolation model. *Physical Review E*, 55(4):3878–3885, 1997. doi:10.1103/PhysRevE.55.3878.

[41] E. Katzav, R. Berdichevsky, and M. Schwartz. Random close packing from hard-sphere Percus-Yevick theory. *Physical Review E*, 99(1):012146, 2019. doi:10.1103/PhysRevE.99.012146.

[42] E. D. Glandt and D. D. Fitts. Percus-Yevick equation of state for the two-dimensional Lennard-Jones fluid. *The Journal of Chemical Physics*, 66(10):4503–4508, 1977. doi:10.1063/1.433702.

[43] E. Leutheusser. On the Percus-Yevick equation for a rigid disk fluid. *The Journal of Chemical Physics*, 84(2):1050–1051, 1986. doi:10.1063/1.450594.

[44] M. Baus and J. L. Colot. Theoretical structure factors for hard-core fluids. *Journal of Physics C: Solid State Physics*, 19(28):L643–L648, 1986. doi:10.1088/0022-3719/19/28/002.

[45] Y. Rosenfeld. Distribution function of two cavities and PercusYevick direct correlation functions for a hard sphere fluid in D dimensions: Overlap volume function representation. *The Journal of Chemical Physics*, 87(8):4865–4869, 1987. doi:10.1063/1.452797.

[46] M. Heinen, S. K. Schnyder, J. F. Brady, and H. Löwen. Classical Liquids in Fractal Dimension. *Physical Review Letters*, 2015. doi:10.1103/PhysRevLett.115.097801.

[47] S. B. Lee and S. Torquato. Monte Carlo study of correlated continuum percolation: Universality and percolation thresholds. *Physical Review A*, 41(10):5338–5344, 1990. doi:10.1103/PhysRevA.41.5338.

[48] S. B. Lee and S. Torquato. Pair connectedness and mean cluster size for continuum-percolation models: Computer-simulation results. *The Journal of Chemical Physics*, 89(10):6427–6433, 1988. doi:10.1063/1.455411.

[49] H. C. Andersen and D. Chandler. Optimized Cluster Expansions for Classical Fluids. I. General Theory and Variational Formulation of the Mean Spherical Model and Hard Sphere PercusYevick Equations. *The Journal of Chemical Physics*, 57(5):1918–1929, 1972. doi:10.1063/1.1678512.

[50] L. Blum. Invariant expansion. II. The Ornstein-Zernike equation for nonspherical molecules and an extended solution to the mean spherical model. *The Journal of Chemical Physics*, 57(5):1862–1869, 1972. doi:10.1063/1.1678503.

[51] D. Lara and F. Vericat. Percolation behavior of long permeable objects: A reference interaction-site-model study. *Physical Review B*, 40(1):353–360, 1989. doi:10.1103/PhysRevB.40.353.

[52] K. Leung and D. Chandler. Theory of percolation in fluids of long molecules. *Journal of Statistical Physics*, 63(5-6):837–856, 1991. doi:10.1007/BF01029986.

[53] D. Chandler, R. Silbey, and B. M. Ladanyi. New and proper integral equations for site-site equilibrium correlations in molecular fluids. *Molecular Physics*, 46(6):1335–1345, 1982. doi:10.1080/00268978200101971.

[54] M. Lupkowski and P. A. Monson. An interaction site approach to clustering and percolation phenomena in systems of nonspherical particles. *The Journal of Chemical Physics*, 89(5):3300–3307, 1988. doi:10.1063/1.454936.

[55] A. O. Weist and E. D. Glandt. Clustering and percolation for dimerizing penetrable spheres. *The Journal of Chemical Physics*, 95(11):8365–8373, 1991. doi:10.1063/1.461264.

[56] C. M. Cortis, P. J. Rossky, and R. A. Friesner. A three-dimensional reduction of the Ornstein-Zernicke equation for molecular liquids. *The Journal of Chemical Physics*, 107(16):6400–6414, 1997. doi:10.1063/1.474300.

[57] K. M. Dyer, J. S. Perkyns, and B. M. Pettitt. A site-renormalized molecular fluid theory. *The Journal of Chemical Physics*, 127(19):194506, 2007. doi:10.1063/1.2785188.

[58] P. G. Ferreira, A. Perera, M. Moreau, and M. M. Telo da Gama. The hard ellipse liquid: An integral equation study. *The Journal of Chemical Physics*, 95(10):7591–7602, 1991. doi:10.1063/1.461385.

[59] L. Blum. Invariant expansion III: The general solution of the mean spherical model for neutral spheres with electostatic interactions. *The Journal of Chemical Physics*, 58(8):3295–3303, 1973. doi:10.1063/1.1679655.

[60] G. Stell. Exact equation for the pair-connectedness function. *Journal of Physics A: Mathematical and General*, 17(15):L855–L858, 1984. doi:10.1088/0305-4470/17/15/007.

[61] P. C. Hemmer. Virial Coefficients for the HardCore Gas in Two Dimensions. *The Journal of Chemical Physics*, 42(3):1116–1118, 1965. doi:10.1063/1.1696049.

[62] S. P. Finner, T. Schilling, and P. van der Schoot. Connectivity, Not Density, Dictates Percolation in Nematic Liquid Crystals of Slender Nanoparticles. *Physical Review Letters*, 122(9):097801, 2019. doi:10.1103/PhysRevLett.122.097801.

[63] P. van der Schoot. The Nematic-Smectic Transition in Suspensions of Slightly Flexible Hard Rods. *Journal de Physique II*, 6(11):1557–1569, 1996. doi:10.1051/jp2:1996147.

[64] A. M. Somoza, C. Sagui, and C. Roland. Liquid-crystal phases of capped carbon nanotubes. *Physical Review B*, 63(8):081403, 2001. doi:10.1103/PhysRevB.63.081403.

[65] A. M. Bohle, R. Hołyst, and T. Vilgis. Polydispersity and Ordered Phases in Solutions of Rodlike Macromolecules. *Physical Review Letters*, 76(8):1396–1399, 1996. doi:10.1103/PhysRevLett.76.1396.

[66] M. A. Bates and D. Frenkel. Influence of polydispersity on the phase behavior of colloidal liquid crystals: A Monte Carlo simulation study. *The Journal of Chemical Physics*, 109(14):6193–6199, 1998. doi:10.1063/1.477248.

[67] C. Zakri. Carbon nanotubes and liquid crystalline phases. *Liquid Crystals Today*, 16(1):1–11, 2007. doi:10.1080/14645180701514426.

[68] D. A. Triplett, L. M. Quimby, B. D. Smith, D. Hernández Rodríguez, S. K. St. Angelo, P. González, C. D. Keating, and K. A. Fichthorn. Assembly of Gold Nanowires by Sedimentation from Suspension: Experiments and Simulation. *The Journal of Physical Chemistry C*, 114(16):7346–7355, 2010. doi:10.1021/jp909251v.

[69] B. D. Smith, K. A. Fichthorn, D. J. Kirby, L. M. Quimby, D. A. Triplett, P. González, D. Hernández, and C. D. Keating. Asymmetric van der Waals Forces Drive Orientation of Compositionally Anisotropic Nanocylinders within Smectic Arrays: Experiment and Simulation. *ACS Nano*, 8(1):657–670, 2014. doi:10.1021/nn405312x.

[70] M. Schrader, C. Körner, C. Elschner, and D. Andrienko. Charge transport in amorphous and smectic mesophases of dicyanovinyl-substituted oligothiophenes. *Journal of Materials Chemistry*, 22(41):22258, 2012. doi:10.1039/c2jm34837c.

[71] E. Engel and R. M. Dreizler. Density Functional Theory. In *Theoretical and Mathematical Physics*, Theoretical and Mathematical Physics, chapter Appendix A. Springer Berlin Heidelberg, Berlin, Heidelberg, 2011. doi:10.1007/978-3-642-14090-7.

[72] M. P. Allen, G. T. Evans, D. Frenkel, and B. M. Mulder. Hard Convex Body Fluids. *Advances in chemical physics*, 86(1):1–166, 2007. doi:10.1002/9780470141458.ch1.

[73] M. D. Lipkin and D. W. Oxtoby. A systematic density functional approach to the mean field theory of smectics. *The Journal of Chemical Physics*, 79(4):1939–1941, 1983. doi:10.1063/1.445973.

[74] A. Poniewierski and R. Holyst. Density-functional theory for systems of hard rods. *Physical Review A*, 41(12):6871–6880, 1990. doi:10.1103/PhysRevA.41.6871.

[75] Y. Martínez-Ratón, J. A. Cuesta, R. Roij, and B. Mulder. Nematic to Smectic: A Hard Transition. In *New Approaches to Problems in Liquid State Theory*, pages 139–150. Springer Netherlands, Dordrecht, 1999. doi:10.1007/978-94-011-4564-0_9.

[76] B. Mulder. Density-functional approach to smectic order in an aligned hard-rod fluid. *Physical Review A*, 35(7):3095–3101, 1987. doi:10.1103/PhysRevA.35.3095.

[77] J. D. Parsons. Nematic ordering in a system of rods. *Physical Review A*, 19(3):1225–1230, 1979. doi:10.1103/PhysRevA.19.1225.

[78] S. Lee. A numerical investigation of nematic ordering based on a simple hardrod model. *The Journal of Chemical Physics*, 87(8):4972–4974, 1987. doi:10.1063/1.452811.

[79] R. Holyst and A. Poniewierski. Nematic-smectic-A transition for perfectly aligned hard spherocylinders: Application of the smoothed-density approximation. *Physical Review A*, 39(5):2742–2744, 1989. doi:10.1103/PhysRevA.39.2742.

[80] A. M. Somoza and P. Tarazona. Density functional approximation for hardbody liquid crystals. *The Journal of Chemical Physics*, 91(1):517–527, 1989. doi:10.1063/1.457487.

[81] A. Stroobants, H. N. W. Lekkerkerker, and D. Frenkel. Evidence for one-, two-, and three-dimensional order in a system of hard parallel spherocylinders. *Physical Review A*, 36(6):2929–2945, 1987. doi:10.1103/PhysRevA.36.2929.

[82] L. A. Pugnaloni and F. Vericat. Clustering and continuum percolation of hard spheres near a hard wall: Monte Carlo simulation and connectedness theory. *The Journal of Chemical Physics*, 110(8):4028–4034, 1999. doi:10.1063/1.478284.

[83] A. P. Chatterjee and C. Grimaldi. A lattice model for the impact of volume fraction fluctuations upon percolation by cylinders. *The Journal of Chemical Physics*, 147(17):174902, 2017. doi:10.1063/1.5001068.

[84] A. P. Chatterjee and C. Grimaldi. Relation between a heterogeneous percolation model for cylinders and phase separation in the lattice fluid problem. *Physical Review E*, 98(6):062125, 2018. doi:10.1103/PhysRevE.98.062125.

[85] D. Henderson. Integral Equations for Inhomogeneous Fluids. In *Condensed Matter Theories*, pages 427–433. Springer US, Boston, MA, 1993. doi:10.1007/978-1-4615-2934-7_37.

[86] F. Lado. An efficient procedure for the study of inhomogeneous liquids. *Molecular Physics*, 107(4-6):301–308, 2009. doi:10.1080/00268970802603531.

[87] A. V. Kyrylyuk and P. van der Schoot. Continuum percolation of carbon nanotubes in polymeric and colloidal media. *Proceedings of the National Academy of Sciences*, 105(24):8221–8226, 2008. doi:10.1073/pnas.0711449105.

[88] I. Dayan, J. F. Gouyet, and S. Havlin. Percolation in multi-layered structures. *Journal of Physics A: Mathematical and General*, 24(6):L287–L293, 1991. doi:10.1088/0305-4470/24/6/007.

[89] G. Y. Hu and R. F. O'Connell. Analytical inversion of symmetric tridiagonal matrices. *Journal of Physics A: Mathematical and General*, 29(7):1511–1513, 1996. doi:10.1088/0305-4470/29/7/020.

[90] A. Jaiswal, A. S. Bharadwaj, and Y. Singh. Communication: Integral equation theory for pair correlation functions in a crystal. *The Journal of Chemical Physics*, 140(21):211103, 2014. doi:10.1063/1.4881420.

[91] B. Noble. *Methods based on the Wiener-Hopf technique for the solution of partial differential equations*. Chelsea Pub Co, 1988.

[92] A. J. Hamilton. Uncorrelated modes of the non-linear power spectrum. *Monthly Notices of the Royal Astronomical Society*, 312(2):257–284, 2000. doi:10.1046/j.1365-8711.2000.03071.x.

[93] J. D. Talman. Numerical Fourier and Bessel transforms in logarithmic variables. *Journal of Computational Physics*, 29(1):35–48, 1978. doi:10.1016/0021-9991(78)90107-9.

[94] V. Boţan, F. Pesth, T. Schilling, and M. Oettel. Hard-sphere fluids in annular wedges: Density distributions and depletion potentials. *Physical Review E*, 79(6):061402, 2009. doi:10.1103/PhysRevE.79.061402.

[95] G. P. Agrawal and M. Lax. End correction in the quasi-fast Hankel transform for optical-propagation problems. *Optics Letters*, 1981. doi:10.1364/ol.6.000171.

[96] A. Kovalenko, S. Ten-no, and F. Hirata. Solution of three-dimensional reference interaction site model and hypernetted chain equations for simple point charge water by modified method of direct inversion in iterative subspace. *Journal of Computational Chemistry*, 20(9):928–936, 1999. doi:10.1002/(SICI)1096-987X(19990715)20:9<928::AID-JCC4>3.0.CO;2-X.

Appendix A

Wiener-Hopf Factorisation

In this Appendix we discuss the solution strategy for the Percus-Yevick integral equation and how it can be solved via the so-called Wiener-Hopf factorisation. We discuss only the necessary parts of the theory of Wiener-Hopf factorisations, and refer any interested reader to the extensive book by Noble [91]. To avoid cumbersome notation, we discuss the mathematical aspects of Fourier transforms in three dimensions only, but note that it can be generalised to any odd dimension [37].

We start by considering the connectedness Ornstein-Zernike equation in Fourier space, which can be conveniently written as

$$[1 - \rho\widehat{C}^{+}(q)][1 + \rho\widehat{P}(q)] = 1, \tag{A.1}$$

where ρ is the number density, $\widehat{C}^{+}(q)$ is the Fourier transform of direct connectedness function $C^{+}(r)$ and $\widehat{P}(q)$ is the Fourier transform of pair connectedness function $P(r)$. We can rewrite Equation (A.1) as

$$1 + \rho\widehat{P}(q) = \widehat{A}(q)^{-1} \tag{A.2}$$

where we define

$$\widehat{A}(q) = 1 - \rho\widehat{C}^{+}(q), \tag{A.3}$$

The choice of writing $\widehat{A}(q)$ as function of C^{+} appears arbitrary, but is not. Since C^{+} is short-ranged in the Percus-Yevick closure, the Fourier transform in Equation (A.3) can be truncated at the particle diameter d. This enables us to rewrite Equation (A.3) as

$$\widehat{A}(q) = 1 - 4\pi\rho \int_0^d \cos(qr) S(r) \mathrm{d}r, \tag{A.4}$$

where

$$S(r) = \int_r^d t C^{+}(t) \mathrm{d}t. \tag{A.5}$$

If we assume that $\widehat{P}(q)$ is finite for any q, which holds below the percolation threshold, $\widehat{A}(q)$ has no zeroes on the real q-axis [34]. In order to derive the functional factorised form, we need to inspect the behaviour of $\widehat{A}(q)$ in the complex q-plane. Therefore we set $q = x + iy$ in the rest of

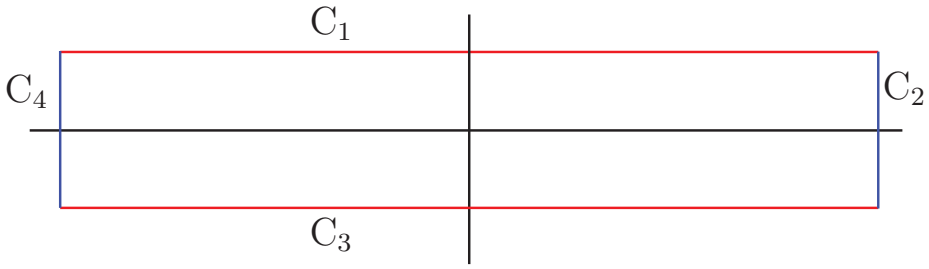

Figure A.1: A schematic view of the contour for the contour integration over $\log \widehat{A}(q)$. The x-axis corresponds to the real axis, whereas the y-axis corresponds to the imaginary axis.

this Appendix. Since $\widehat{A}(q)$, as given in Equation (A.4), is a Fourier transform over a finite interval, it is *regular* throughout the complex plane, *i.e.*, it is differentiable at every point in the complex plane. In Equation (A.1), we observe that $\widehat{A}(q)$ goes uniformly to zero as $|x| \to \infty$ in any strip $y_0 \leq y \leq y_1$. Hence, a strip must exists where $|y| \leq \varepsilon$ about the real axis within which $\widehat{A}(q)$ has no zeros. Next, we will make use of Cauchy's integral formula

$$f(\alpha) = \frac{1}{2\pi i} \oint \mathrm{d}z \frac{f(z)}{\alpha - z}, \tag{A.6}$$

where α and z are coordinates in the complex plane. We integrate around $\log \widehat{A}(q)$ with a contour as shown in Figure A.1, where C_1 is the contour from $-\infty + i\varepsilon$ to $\infty + i\varepsilon$, and C_3 is the contour from $-\infty - i\varepsilon$ to $\infty - i\varepsilon$. Since $\log \widehat{A}(q) \to 0$ for $|x| \to \infty$, the contours C_2 and C_4 have no net contribution. Hence, we can write

$$\log \widehat{A}(q) = \log \widehat{Q}(q) + \log \widehat{L}(q), \tag{A.7}$$

where

$$\log \widehat{Q}(q) = \frac{1}{2\pi i} \int_{-i\varepsilon-\infty}^{-i\varepsilon+\infty} \mathrm{d}q' \frac{\log \widehat{A}(q)}{q' - q} \tag{A.8}$$

$$\log \widehat{L}(q) = -\frac{1}{2\pi i} \int_{i\varepsilon-\infty}^{i\varepsilon+\infty} \mathrm{d}q' \frac{\log \widehat{A}(q)}{q' - q}. \tag{A.9}$$

From Equation (A.4) we know that $\widehat{A}(q)$ is an even function and therefore, by negating q' in Equation (A.9) we obtain

$$\log \widehat{L}(q) = \log \widehat{Q}(-q). \tag{A.10}$$

Next, we can show that $\log \widehat{Q}(q)$ is an analytical regular function by writing

$$\log \widehat{Q}(x + iy) = \frac{1}{2\pi i} \int_{-\infty}^{\infty} \mathrm{d}t \frac{\log \widehat{A}(t - i\varepsilon)}{(t - x) + i(\varepsilon - y)}, \tag{A.11}$$

which satisfies the conditions of an regular function in the domain $y > -\varepsilon$. Hence, it follows that for $|y| < \varepsilon$ we obtain

$$\widehat{A}(q) = \widehat{Q}(q)\widehat{Q}(-q), \tag{A.12}$$

where $\widehat{Q}(q)$ is also regular and has no zeros in the domain $y > -\varepsilon$ [91]. Equation (A.12) is the Wiener-Hopf factorisation of $\widehat{A}(q)$.

We continue by inspecting the behaviour of $Q(q)$ to derive some useful properties. By inspecting Equation (A.8) we note that when $|x| \to \infty$ within the strip $|y| < \varepsilon$, it follows that $\log \widehat{Q}(q) \sim x^{-1}$ and hence $\widehat{Q}(q) \sim 1 - \mathcal{O}(x^{-1})$. The function $1 - \widehat{Q}(q)$ is therefore Fourier-integrable along the real axis, and a function $Q(r)$ can be defined as

$$2\pi\rho Q(r) = \frac{1}{2\pi} \int_{-\infty}^{\infty} \exp(-iqr) \left[1 - \widehat{Q}(q)\right] \mathrm{d}q. \tag{A.13}$$

By inspecting Equation (A.8), we observe that if q is real, the complex conjugate of $\widehat{Q}(q)$ is $\widehat{Q}(-q)$, *i.e.*, $\widehat{Q}(q)$ is Hermitian. Hence, $Q(r)$ must be a real function. Next, we can calculate Equation (A.13) for $r < 0$. We do this by using a contour integral and Jordan's lemma. Let us define the following function

$$f(z) = e^{iaz} g(z), \tag{A.14}$$

where a is a positive parameter and z is defined on a semicircular contour R in the upper half-plane $z \in \{Re^{i\theta} | \theta \in 0, \pi|\}$. Jordan's Lemma then states that the upper bound for this contour integral is given by

$$\left| \int f(z) \mathrm{d}z \right| \leq \frac{\pi}{a} M_R, \tag{A.15}$$

where M_R is the maximum value for $|g(Re^{i\theta})|$. Hence, if $M_R \to 0$, the contour integral along R is zero.

For $r < 0$ we can close the contour for Equation (A.13) around the upper half-plane, where $\widehat{Q}(q)$ is regular. This shows that

$$Q(r) = 0 \qquad \text{for } r < 0. \tag{A.16}$$

We also wish to close $Q(r)$ for $r > d$. The analytic continuation of $\widehat{Q}(q)$ into the lower half-plane is given by

$$Q(q) = A(q)/Q(-q). \tag{A.17}$$

By Equation (A.9) we know that $\widehat{Q}(-q) \to 1$ for $y \to -\infty$. Hence, by the previous equation and by Equation (A.4), we know that for large and negative y, $\widehat{A}(q)$ and $\widehat{Q}(q)$ grow as $\exp iqd$. This allows us to close Equation (A.13) around the lower half plane for $r > d$, giving

$$Q(r) = 0 \qquad \text{for } r > d. \tag{A.18}$$

With these bounds on $Q(r)$, we can simply invert Equation (A.13) to obtain

$$\widehat{Q}(q) = 1 - 2\pi\rho \int_0^d \mathrm{d}r e^{iqr} Q(r). \tag{A.19}$$

This expression for $\widehat{Q}(q)$ can be used to simplify the connectedness Ornstein-Zernike Equation. Combining Equations (A.4), (A.12) and (A.19) gives

$$\left(1-2\pi\rho\int_0^d \mathrm{d}r e^{iqr}Q(r)\right)\left(1-2\pi\rho\int_0^d \mathrm{d}r e^{-iqr}Q(r)\right)=1-4\pi\rho\int_0^d \cos(qr)S(r)\mathrm{d}r. \tag{A.20}$$

Multiplying both sides by $e^{-iqr'}$ and integrating over q from $-\infty$ to ∞ gives

$$S(r)=Q(r)-2\pi\rho\int_r^d \mathrm{d}t Q(t)Q(t-r) \qquad 0<r<d, \tag{A.21}$$

which, upon taking the derivative with respect to r, gives

$$rC^+(r)=-Q'(r)-2\pi\rho\int_r^d \mathrm{d}t Q'(t)Q(t-r) \qquad 0<r<d. \tag{A.22}$$

Using the same technique for $P(r)$ we obtain

$$rP(r)=-Q'(r)+2\pi\rho\int_0^d \mathrm{d}t (r-t)P(|r-t|)Q(t) \qquad r>0. \tag{A.23}$$

The equations (A.22) and (A.23) are the connectedness Ornstein-Zernike equation in factorised form. In this derivation we have assumed two things, namely that $\widehat{P}(q)$ is finite for all q on the real axis, and that $C^+(r)$ is of finite range. This does mean that any closure that has $C^+(r)$ to be of finite range in r can be written in an equivalent finite form. This simplifies the solution of the connectedness Ornstein-Zernike equation significantly as we do no longer need to solve the connectedness Ornstein-Zernike equation over an infinite range, but only require knowledge of the function over a small range.

Appendix B

The Percus-Yevick equation for disks

In Appendix A, we derived the Wiener-Hopf factorisation for the three dimensional case, and it can be extended to any odd dimension D. For even dimensions, however, this is not the case. In this Appendix we show why even dimensions are troublesome by using the example of $D = 2$ case. We indicate one possible method to circumvent this problem at the end of this Appendix, and also show that solving the equations after factorisation still requires knowledge of a function over infinite space.

We start again from the Ornstein-Zernike equation given by

$$[1 - \rho\widehat{C}^{+}(q)][1 + \rho\widehat{P}(q)] = 1, \tag{B.1}$$

where ρ is the number density, $\widehat{C}^{+}(q)$ is the Fourier transform of direct connectedness function $C^{+}(r)$ and $\widehat{P}(q)$ is the Fourier transform of the pair connectedness function $P(r)$. We can then rewrite Equation (B.1) where we similarly define $\widehat{A}(q)$ as

$$\widehat{A}(q) = 1 - \rho\widehat{C}^{+}(q), \tag{B.2}$$

where $\widehat{A}(q)$ is still given by

$$\widehat{A}(q) = \widehat{Q}(q)\widehat{Q}(-q). \tag{B.3}$$

As shown in Appendix A, we can write

$$\widehat{Q}(q) = 1 - \rho\int_0^d Q(r)e^{iqr}\mathrm{d}r. \tag{B.4}$$

The Fourier transform of $C^{+}(r)$ is now given by

$$\widehat{C}^{+}(q) = 2\pi\int_0^d rJ_0(qr)C^{+}(r)\mathrm{d}r, \tag{B.5}$$

where J_0 is the zeroth order Bessel function. This transform is related to a zeroth order Hankel transform. The inverse Fourier transform is given by

$$C^{+}(r) = 2\pi\int_0^\infty qJ_0(qr)\widehat{C}^{+}(q)\mathrm{d}q. \tag{B.6}$$

Inserting $\widehat{A}(q)$ and $C^+(r)$ in the Ornstein-Zernike Equation (B.1) gives

$$\left(1-\rho\int_0^d Q(r)e^{iqr}\mathrm{d}r\right)\left(1-\rho\int_0^d Q(r)e^{iqr}\mathrm{d}r\right)=1-2\pi\rho\int_0^d rJ_0(qr)C^+(r)\mathrm{d}r. \tag{B.7}$$

Following through with the same procedure by multiplying both sides with $\exp(-iqt)$ and integrating over q from $-\infty$ to ∞, we obtain

$$2\pi\int_r^d \frac{2t}{\sqrt{r^2-t^2}}C^+(t)\mathrm{d}t=2Q(r)-2\rho\int_r^d Q(t)Q(t-r)\mathrm{d}t. \tag{B.8}$$

This integral is of similar form as Equation (A.21) of Appendix A, which in odd dimensions we consequently simplified by differentiating it with respect to r. While we could naively attempt the same strategy in two dimensions, we immediately notice that this cannot be used to simplify the term on the left hand side. Moreover, the term on the left hand side diverges if we attempt this. Hence this is the end station of this strategy.

A method that can be used to factorise the Ornstein-Zernike equations has recently been derived by Adda-Bedia *et al.* [35]. We provide an outline only, and refer for the full derivation to the references [35, 36]. Equation (B.6) can be used to show that $\widehat{C}^+(q)$ can be written as

$$\widehat{C}^+(q)=\frac{1}{q}\int_0^1 \phi(t)\sin(qt)\mathrm{d}t, \tag{B.9}$$

where $\phi(t)$ is a real function [35]. Then, using Equation (B.6), $C^+(r)$ is written as

$$C^+(r)=\int_r^1 \frac{\phi(t)}{\sqrt{t^2-r^2}}\frac{\mathrm{d}t}{2\pi}, \tag{B.10}$$

where appropriate conditions on $\phi(t)$ are necessary, as $C^+(r)$ does not diverge if we approach $r=1$ from below. In this particular case, it is useful to use the normal Wiener-Hopf factorisation. This allows us to link $\phi(t)$ to $Q(r)$ via

$$\phi(t)=-2Q'(t)+2\rho\int_t^1 Q'(s)Q(s-t)\mathrm{d}s, \qquad 0\le t\le 1, \tag{B.11}$$

with boundary condition $Q(1)=0$. Hence, if $Q(t)$ is known, it allows us to determine $\phi(t)$ and $C^+(r)$. Since $\widehat{P}(q)=\widehat{P}(-q)$ we may write without loss of generality

$$q\widehat{P}(q)=\int_0^\infty \psi(t)\sin qt\mathrm{d}t, \tag{B.12}$$

where $\psi(t)$ is a real function and $P(r)$ is given in terms of $\psi(t)$ by

$$P(r)=\int_r^\infty \frac{\psi(t)}{\sqrt{t^2-r^2}}\frac{\mathrm{d}t}{2\pi}. \tag{B.13}$$

After some algebra, this can be written as

$$\psi(t) = \frac{-4t}{\sqrt{1-t^2}} \left[\int_1^\infty \frac{\sqrt{s^2-1}}{s^2-t^2} \psi(s) \frac{\mathrm{d}s}{2\pi} - 1 \right]. \tag{B.14}$$

This equation fixes $\psi(t)$ for $0 < t < 1$ as a function of $t > 1$. Next, we can link $\psi(t)$ and $Q(t)$ as

$$2Q'(t) + \psi(t) = \rho \int_0^t Q(s)\psi(t-s)\mathrm{d}s - \rho \int_t^1 Q(s)\psi(s-t)\mathrm{d}s, \tag{B.15}$$

which is valid for $0 < t < 1$ and

$$\psi(t) = \rho \int_0^1 Q(s)\psi(t-s)\mathrm{d}s, \tag{B.16}$$

for $t > 1$. While this factorisation limits $\phi(t)$ and $Q(t)$ over the interaction range of the particles only, this is not true for $\psi(t)$. $\psi(t)$ for $t < 1$ is dependent on $t > 1$, so that it cannot be used to obtain analytical solutions for the mean cluster size S or other quantities. While the numerical solution proposed by Adda-Bedia *et al.* [35] is simple and does not have the troublesome divergence that is present at $q \to 0$ in the normal Ornstein-Zernike equation, it is only slowly convergent. Since we expect the mean cluster size S to diverge for $\eta > 1$ for ideal particles, and the solution method proposed by Adda-Bedia *et al.* [35] is an order-by-order solution in the density ρ, it can be expected that the solution does not converge fast enough for a low density expansion in ρ to give accurate predictions. Indeed we observe that for the first twenty orders in the density, the solution does not seem to converge.

Appendix C

Calculations for the smectic-A phase

Evaluating $C^+(q_r, q_z)$

The Fourier transform of $C^+(\vec{r}, z)$ is given by

$$\hat{\hat{C}}^+(\vec{q}_r, q_z) = \int \mathrm{d}\vec{r} e^{\vec{q}_r \cdot \vec{r}} \int \mathrm{d}z e^{q_z z} C^+(\vec{r}, z). \tag{C.1}$$

We employ the renormalised second virial approximation, which is given by

$$C^+(\vec{r}, z) = \Gamma(\eta) f^+(\vec{r}, z), \tag{C.2}$$

where $\Gamma(\eta)$ is the Parsons-Lee correction term, and $f^+(\vec{r}, z)$ is the connectedness Mayer f-function. The precise definition of $f^+(\vec{r}, z)$ is dependent on the particle shape and connectedness criterion. Here we use the cherry-pit model, where $f^+(\vec{r}, z) = 0$ for hard-core overlap and no overlap, and $f^+(\vec{r}, z) = 1$ if the connectivity shells overlap. This connectivity shell consists of three separate integrals that determine the contact volume: one due to cylinder-cylinder overlap and two due to cap-cap overlap. Cylinder-cap contribution are not present, as the particles are perfectly aligned. Hence, we obtain $\hat{\hat{C}}^+(\vec{q}_r, q_z) = \Gamma(\eta)\hat{\hat{f}}^+(\vec{q}_r, q_z)$, where $\hat{\hat{f}}^+(\vec{q}_r, q_z)$ is given by

$$\begin{aligned}\hat{\hat{f}}^+(\vec{q}_r, q_z) = &\int_D^{D+\lambda_r} \mathrm{d}\vec{r} \int_{-L}^{L} \mathrm{d}z e^{i\vec{q}_r \cdot \vec{r}} e^{iq_z z} + \int_0^{D+\lambda_r} \mathrm{d}\vec{r} \int_L^{L+\lambda_z} \mathrm{d}z e^{i\vec{q}_r \cdot \vec{r}} e^{iq_z z} + \\ &\int_0^{D+\lambda_r} \mathrm{d}\vec{r} \int_{-L}^{-L-\lambda_z} \mathrm{d}z e^{i\vec{q}_r \cdot \vec{r}} e^{iq_z z}\end{aligned} \tag{C.3}$$

These integrals can be carried out to give

$$\begin{aligned}\hat{\hat{f}}^+(q_r, q_z) = &8v_0 j_0(q_z L) \left(\left[1 + \frac{\lambda_r}{D}\right]^2 \frac{J_1(q_r D(1 + \frac{\lambda_r}{D}))}{\frac{1}{2} q_r D(1 + \frac{\lambda_r}{D})} - \frac{J_1(q_r D)}{\frac{1}{2} q_r D} \right) \\ &+ 8v_0 \left[1 + \frac{\lambda_r}{D}\right]^2 \frac{J_1(q_r D(1 + \frac{\lambda_r}{D}))}{\frac{1}{2} q_r D(1 + \frac{\lambda_r}{D})} \left(\left[1 + \frac{\lambda_z}{L}\right] j_0 \left(q_z L \left[1 + \frac{\lambda_z}{L}\right] \right) - j_0(q_z L) \right),\end{aligned} \tag{C.4}$$

where J_1 is the Bessel function of order 1, j_0 is the zeroth order spherical Bessel function, and $v_0 = 1/4\pi LD^2$ is the volume of the hard core of a single cylinder. In the limit $q_r, q_z \to 0$ this reduces to

$$\hat{\hat{f}}^+(0,0) = 8v_0\left((1+\frac{\lambda_r}{D})^2 - 1\right) + 8v_0(1+\frac{\lambda_r}{D})^2\frac{\lambda_z}{L}. \tag{C.5}$$

Evaluating $D^+(q_r, q_z)$

Next, we evaluate $\hat{\hat{D}}^+(q_r, q_z)$ for the connectivity shell criterion. The full expression for $\hat{\hat{D}}^+(q_r, q_z)$ is given by

$$\hat{\hat{D}}^+(\vec{q}_r, q_z) = \frac{q}{2\pi}\int_0^\infty \mathrm{d}\vec{r}\int_{-\infty}^{\infty}\mathrm{d}z_1\int_{-\frac{\pi}{q}}^{\frac{\pi}{q}}\mathrm{d}z_2(1+\sum_j \Delta_j\cos(jqz_2))C^+(r,z_1,z_2)e^{i\vec{q}_r\cdot\vec{r}}e^{iq_z\cdot z_1}, \tag{C.6}$$

The radial integrals in $\hat{\hat{D}}^+(\vec{q}_r, q_z)$ are the same integrals as for $C^+(\vec{q}_r, q_z)$ and can therefore be pre-integrated as

$$\hat{\hat{D}}^+(q_r, q_z) = \sum_{i=1}^{3} c_i(q_r)\frac{q}{2\pi}\int_{-\frac{\pi}{q}}^{\frac{\pi}{q}}\mathrm{d}z_2\int_{-\infty}^{\infty}\mathrm{d}z_1(1+\sum_j \Delta_j\cos(jqz_2))f_i^+(z_1,z_2)e^{iq_z z_1}. \tag{C.7}$$

Here, the functions $c_i(q_z)$ are the placeholders for the radial pre-integrated parts, and $f_i^+(z_1, z_2)$ represents the z-dependency of the Connectedness Mayer-f function. We have to sum three separate contribution due to the two additional connectivity shells around the head and tail of the cylinder. The three z_1 integrals of $f_i^+(z_1, z_2)$ need to be evaluated for fixed z_2 from $z_2 - L$ to $z_2 + L$ for the cylinder and from $z_2 \pm L$ to $z_2 \pm (L + \lambda_z)$ for the end parts. Hence we split $\hat{\hat{D}}^+(q_r, q_z)$ in three integrals as

$$\hat{\hat{D}}_1^+(q_r, q_z) = c_1(q_r)\frac{q}{2\pi}\int_{-\frac{\pi}{q}}^{\frac{\pi}{q}}\mathrm{d}z_2\int_{z_2-L}^{z_2+L}\mathrm{d}z_1(1+\sum_j \Delta_j\cos(jqz_2))e^{iq_z(z_1)}, \tag{C.8}$$

and

$$\hat{\hat{D}}_2^+(q_r, q_z) = c_2(q_r)\frac{q}{2\pi}\int_{-\frac{\pi}{q}}^{\frac{\pi}{q}}\mathrm{d}z_2\int_{z_2-L}^{z_2-L-\lambda_z}\mathrm{d}z_1(1+\sum_j \Delta_j\cos(jqz_2))e^{iq_z(z_1)}, \tag{C.9}$$

and

$$\hat{\hat{D}}_3^+(q_r, q_z) = c_3(q_r)\frac{q}{2\pi}\int_{-\frac{\pi}{q}}^{\frac{\pi}{q}}\mathrm{d}z_2\int_{z_2+L}^{z_2+L+\lambda_z}\mathrm{d}z_1(1+\sum_j \Delta_j\cos(jqz_2))e^{iq_z(z_1)}. \tag{C.10}$$

Comparing these expressions with the integrals in Equation (C.3), we immediately observe that the z_1 integrals are the same integrals, only shifted by a constant term z_2. Hence, we can write the complete $\hat{\hat{D}}^+(q_r, q_z)$ as

$$\hat{\hat{D}}^+(q_r, q_z) = \hat{\hat{C}}^+(q_r, q_z)\frac{q}{2\pi}\int_{-\frac{\pi}{q}}^{\frac{\pi}{q}}\mathrm{d}z_2(1+\sum_j \Delta_j\cos(jqz_2))e^{iq_z z_2}. \tag{C.11}$$

The only remaining task is to calculate the last integral. This is easily evaluated by writing the cosine in complex form

$$\frac{q}{2\pi}\int_{-\frac{\pi}{q}}^{\frac{\pi}{q}} \mathrm{d}z_2 \left[1+\sum_j \frac{\Delta_j}{2}\left(e^{ijqz_2}+e^{-ijqz_2}\right)\right] e^{iq_z z_2}, \tag{C.12}$$

or

$$\frac{q}{2\pi}\int_{-\frac{\pi}{q}}^{\frac{\pi}{q}} \mathrm{d}z_2 \left[e^{iq_z z_2}+\sum_j \frac{\Delta_j}{2}\left(e^{i(q_z+jq)z_2}+e^{i(q_z-jq)z_2}\right)\right]. \tag{C.13}$$

This can be evaluated as

$$\frac{q}{2\pi}\int_{-\frac{\pi}{q}}^{\frac{\pi}{q}} \mathrm{d}z_2 \left(e^{iq_z z_2}+\sum_j \frac{\Delta_j}{2}\left(e^{i(q_z+jq)z_2}+e^{i(q_z-jq)z_2}\right)\right) = \left(1+\sum_j (-1)^j \Delta_j \frac{q_z^2}{q_z^2-j^2q^2}\right) j_0\left(\frac{\pi q_z}{q}\right). \tag{C.14}$$

Hence, we can write $\hat{\hat{D}}^+(q_r,q_z)$ as

$$\hat{\hat{D}}^+(q_r,q_z) = \hat{\hat{C}}^+(q_r,q_z)\left(1+\sum_j (-1)^j \Delta_j \frac{q_z^2}{q_z^2-j^2q^2}\right) j_0\left(\frac{\pi q_z}{q}\right). \tag{C.15}$$

Since the connectedness Ornstein-Zernike equation in the smectic-A phase, Equation (6.17), only needs to be solved for $q_z = nq$, with $n \in \mathbb{Z}$, this expression can be simplified significantly by evaluating it only at $q_z = nq$. We need to take the proper limit on $j_0(\frac{\pi q_z}{q})$ for $q_z = nq$ into account, with $n \geq 1$. Doing this allows us to obtain

$$\hat{\hat{D}}^+(q_r,0) = \hat{\hat{C}}^+(q_r,0) \tag{C.16}$$

$$\hat{\hat{D}}^+(q_r,q) = \frac{\Delta_1}{2}\hat{\hat{C}}^+(q_r,q) \tag{C.17}$$

$$\hat{\hat{D}}^+(q_r,nq) = \frac{\Delta_n}{2}\hat{\hat{C}}^+(q_r,nq) \qquad \text{for } n \geq 2, \tag{C.18}$$

While this derivation for $\hat{\hat{D}}^+(q_r,q_z)$ is carried out specifically for the cherry-pit model, Equation (C.11) is, at least, valid for any connectivity criterion where the radial and z dependency decouple.

The lateral correlation length

The function $f(\eta,\lambda_z,\lambda_r)$ in Equation (6.35) is given by

$$f(\eta,\lambda_z,\lambda_r) = \eta\Gamma(\eta)\frac{a_1+a_2+a_3}{a_4}, \tag{C.19}$$

where

$$a_1 = 2\lambda_z + 2\lambda_r(2+\lambda_r)(2+\lambda_r(2+\lambda_r))(1+\lambda_z) \\ - (\Delta_1)^2\left[j_0(Q) - (1+\lambda_r)^4(1+\lambda_z)j_0((1+\lambda_z)Q)\right], \tag{C.20}$$

and

$$a_2 = 16(-2+(\Delta_1)^2)\Gamma(\eta)(\lambda_z + \lambda_r(2+\lambda_r)(2+\lambda_r(2+\lambda_r))(1+\lambda_z))\eta\times \\ \left[-j_0(Q) + (1+\lambda_r)^2(1+\lambda_z)j_0((1+\lambda_z)Q)\right], \tag{C.21}$$

and

$$a_3 = 32(-2+\Delta_1^2)^2\eta^2(\lambda_z + \lambda_r(2+\lambda_r)(2+\lambda_r(2+\lambda_r))(1+\lambda_z))\times \\ \left[j_0(Q) - (1+\lambda_r)^2(1+\lambda_z)j_0(Q(1+\lambda_z))\right]^2\Gamma(\eta)^2, \tag{C.22}$$

and

$$a_4 = \left[1 - 4\left(\Delta_1^2 - 2\right)\eta\Gamma(\eta)\left(j_0(Q) - (\lambda_r+1)^2(\lambda_z+1)j_0((\lambda_z+1)Q)\right)\right]^2. \tag{C.23}$$

Appendix D

Line segments: Contact angles

In order to calculate the overlap coefficients A_N^M for line segments, we need to obtain the contact angles for all positions and orientations for the line segments. The parametric equation for a line segment is given by

$$\begin{pmatrix} y_a \\ x_a \end{pmatrix} = \begin{pmatrix} y_1 \\ x_1 \end{pmatrix} + t_1 \left[\begin{pmatrix} y_2 \\ x_2 \end{pmatrix} - \begin{pmatrix} y_1 \\ x_1 \end{pmatrix} \right], \tag{D.1}$$

where $x_{1,2}$ and $y_{1,2}$ are the coordinates of the end points of a line segment, and $0 \leq t_1 \leq 1$. Both line segments in Figure D.1 can be expressed in this parametric expression. We can extract the intersect coordinates for two line segments by writing the parametric equation for both lines, and equating the y and x coordinates. Solving for $t_{1,2}$ gives us

$$t_1 = \frac{(x_4 - x_3)(y_1 - y_3) - (x_1 - x_3)(y_4 - y_3)}{(x_2 - x_1)(y_4 - y_3) - (x_4 - x_3)(y_2 - y_1)} \tag{D.2}$$

$$t_2 = \frac{(x_2 - x_1)(y_1 - y_3) - (x_1 - x_3)(y_2 - y_1)}{(x_2 - x_1)(y_4 - y_3) - (x_4 - x_3)(y_2 - y_1)}, \tag{D.3}$$

where we can express all x_i, y_i as functions of L, r, θ_1 and θ_2 using trigonometry. Inserting the proper expressions and after some algebra, we obtain

$$t_1 = \frac{1}{2} + x \frac{\sin\theta_2}{\cos(\theta_1 + \theta_2)} \tag{D.4}$$

$$t_2 = \frac{1}{2} - x \frac{\sin\theta_1}{\cos(\theta_1 + \theta_2)}, \tag{D.5}$$

where $x = r/L$. Next, the contact angles for line segments can be calculated by noting that contact *always* occurs at the end-point of one of the two line segments. Hence, we need to solve both $t_{1,2} = 0$ and $t_{1,2} = 1$ as function of θ_2. This gives multiple solutions, which have to be checked for consistency with $0 \leq t_{1,2} \leq 1$ and $0 \leq \theta_2 \leq \pi$. Doing so gives

$$\theta_{2a}(x, \theta_1) = \begin{cases} \arccos \frac{\cos\theta_1 - 2x}{\sqrt{1 + 4x^2 - 4x\cos\theta_1}} & \text{for } \theta_1 \leq \arccos x, \\ \theta_1 + \arcsin 2x \sin\theta_1 & \text{for } \theta_1 > \arccos x, \end{cases} \tag{D.6}$$

$$\theta_{2b}(x, \theta_1) = \pi + \theta_1 - \arcsin 2x \sin\theta_1. \tag{D.7}$$

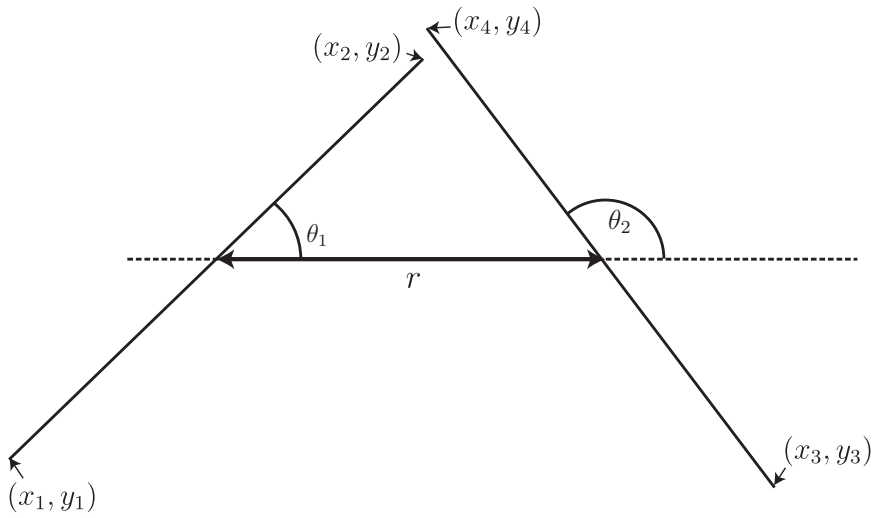

Figure D.1: A schematic overview of the coordinates, angles and distance coordinate r necessary to describe overlap for line segments.

Appendix E

Connectedness-shell in one dimension

Similar to the three-dimensional case, we can investigate the cherry-pit model in one dimension [25]. In the presented method, we assume that the diameter σ of the hard core of the particle is larger than half of the diameter d of entire particle, *i.e.*, hard core and connectivity shell. In that case we can cast the auxiliary function $Q(r)$ as

$$\begin{aligned} Q(r) &= Q_{\mathrm{a}}(r), & 0 < r < d - \sigma, \\ &= Q_b(r - \sigma), & \sigma < r < d, \end{aligned} \tag{E.1}$$

and it can be easily shown that $Q(r)$ is zero in between these regions. We set $d = 1$ for convenience. This allows us to rewrite the one-dimensional factorised connectedness Ornstein-Zernike equation, Equation (3.21), as two equations

$$0 = Q_{\mathrm{a}}(r) + \rho \int_{r+\sigma}^{1} \mathrm{d}s P(s - r) Q_{\mathrm{b}}(s - \sigma) \tag{E.2}$$

and

$$P(r + \sigma) = Q_{\mathrm{b}}(r) + \rho \int_{0}^{r} \mathrm{d}s P(r + \sigma - s) Q_{\mathrm{a}}(s), \tag{E.3}$$

where $P(r)$ is given by the Percus-Yevick radial distribution function. This distribution function is exact in one dimension and completely known as

$$g_{\mathrm{PY}}(x) = \frac{1}{\eta} \sum_{k=1}^{\infty} \Theta(x - k) \left(\frac{\eta}{1 - \eta} \right)^{k} \frac{(x - k)^{k-1}}{(k - 1)!} \exp\left[t_1 (x - k) \right], \tag{E.4}$$

where $t_1 = -\frac{\eta}{1-\eta}$ and $x = \frac{r}{\sigma}$ [40]. Similarly to the connectedness-shell method in three dimensions by DeSimone *et al.* [25], we can cast these equations in two differential equations as

$$0 = Q'_{\mathrm{a}}(r) + \frac{t_1}{\sigma} (Q_{\mathrm{a}}(r) + Q_{\mathrm{b}}(r)), \tag{E.5}$$

$$0 = Q'_{\mathrm{b}}(r) - \frac{t_1}{\sigma} (Q_{\mathrm{a}}(r) + Q_{\mathrm{b}}(r)). \tag{E.6}$$

These two coupled first order homogeneous differential equations can be solved via standard methods. Doing this, we find that the characteristic equation has a double zero root and the solution is therefore given by a polynomial with the maximum order of 2. Hence, we write these equations as

$$Q_{\mathrm{a}}(r) = C_1 r + C_2 r^2 + C_3 \tag{E.7}$$
$$Q_{\mathrm{b}}(r) = -C_1 r - C_2 r^2 + C_4, \tag{E.8}$$

with the boundary conditions

$$Q_{\mathrm{a}}(1-\sigma) = 0, \tag{E.9}$$
$$Q_{\mathrm{b}}(0) = \frac{1}{1-\eta}, \tag{E.10}$$
$$\frac{1}{1-\eta}\frac{t_1}{\sigma} = Q'_{\mathrm{b}}(0) - \frac{t_1}{\sigma} Q_a(0), \tag{E.11}$$
$$0 = Q'_{\mathrm{a}}(1-\sigma) + \frac{t_1}{\sigma} Q_{\mathrm{b}}(1-\sigma). \tag{E.12}$$

This allows us to write $Q(r)$ as a piecewise continuous function of r, given by

$$Q(r) = \begin{cases} \frac{\eta(r+\sigma-1)}{(1-\eta)(\eta+\sigma-2\eta\sigma)}, & r < 1-\sigma \\ 0, & 1-\sigma \leq r \leq \sigma \\ \frac{\sigma-\eta(r+\sigma-1)}{(1-\eta)(1\eta+\sigma-2\eta\sigma)}, & \sigma < r < 1. \end{cases} \tag{E.13}$$

Using this expression, we can calculate the mean cluster size as

$$S = \frac{1}{\hat{Q}(0)^2} = \frac{(\eta+\sigma-2\eta\sigma)^2}{(-\eta\sigma+\sigma)^2}. \tag{E.14}$$

The value of the pair connectedness function just outside the connectedness shell can be obtained by evaluating Equation (3.21) at 1^- and 1^+. This gives

$$P(1^+) = g_{PY}(1/\sigma) - Q(1^-), \tag{E.15}$$

which to the lowest non-zero order in η is given by

$$P(1^+) = \left(-\frac{1}{2} - \frac{1}{2\sigma} + \frac{1}{\sigma}\right)\eta^2 + \mathcal{O}(\eta^3). \tag{E.16}$$

This is zero for $\eta = 0$ and negative for $0 < \eta \leq 1$. Hence, the pair connectedness function shows unphysical behaviour, as it is, by definition, a positive quantity.

Appendix F

Details of the numerical scheme

We have solved the Ornstein-Zernike equation with the Percus-Yevick closure via iteration. This iteration is based on the Fourier-space Ornstein-Zernike equation, while the Percus-Yevick closure is in real-space and can be summarised as

$$Z_i(r) \to C^+(r) \to \widehat{C}^+(q) \to \widehat{Z}(q) \to Z_{i+1}(r).$$

Here, $Z(r) = P(r) - C^+(r)$. $Z_i(r)$ and $Z_{i+1}(r)$ are then mixed in some manner and used as input for the next iteration step. If the difference in output Z_{i+1} and the input Z_i is smaller than a pre-set value, we assume the method to have converged. While the method is essentially simple, some care is required in the Fourier transforms and to the mixing method as the iteration of the (connectedness) Ornstein-Zernike equation near a critical region is often found to be problematic. Numerically computing the radial Fourier transform in a two dimensional system is more troublesome than its three-dimensional counterpart, as we cannot rely straightforwardly on accurate FFT-methods. Many different methods have been proposed for two-dimensional radial fourier transforms, often tailored to the specific problem at hand. We need a method that is accurate, fast and can also calculate Hankel transforms of arbitrary integer order. For this purpose, we have employed a method based on a logarithmic change of variables, *i.e.*, we calculate the Fourier transform on a grid where both the r-grid and q-grid have a logarithmic grid spacing. We have relied on the FFTlog program that has been published by Hamilton [92], which we found to be sufficiently accurate. We discuss this method in the next section.

FFTlog: Hankel Transforms on logarithmic grids

The FFTlog method is based on an logarithmic change of variables, and for a formal discussion we refer to Talman [93] and Hamilton [92]. We start by considering the Hankel transform pair

$$G(q) = \int_0^\infty g(r) J_\nu(qr) q \mathrm{d}r, \tag{F.1}$$

and

$$g(r) = \int_0^\infty G(q) J_\nu(qr) r \mathrm{d}q, \tag{F.2}$$

where J_ν is the Bessel function of order ν, q is the complex wave vector and r is the radial coordinate. Let us consider the change of variables $r = e^\tau$, $q = e^\kappa$ and define $\tilde{G}(\kappa) = G(e^\kappa)$ and $\tilde{g}(\tau) = g(e^\tau)$. This allows us to rewrite Equation (F.1) as

$$\tilde{G}(\kappa) = \int_{-\infty}^{\infty} \tilde{g}(\tau) J_\nu(e^{\tau+\kappa}) e^\kappa \mathrm{d}\tau e^\tau. \tag{F.3}$$

We immediately observe that this integral is a convolution type integral. Since convolution type integrals are naturally calculated via FFT methods, this allows us to calculate the Hankel transform of arbitrary order ν by use of standard FFT methods. While this integral can be simplified further, we do not discuss this here, as a clear derivation is available in Hamilton [92] and Talman [93].

The Hankel transform pair can be linked to the Fourier transform in any dimension via

$$\widehat{F}(q) = \frac{(2\pi)^{D/2}}{q^{D/2-1}} \int_0^\infty \mathrm{d}r r^{D/2} f(r) J_{D/2-1}(qr), \tag{F.4}$$

and the inverse is defined as

$$f(r) = \frac{r^{1-D/2}}{(2\pi)^{D/2}} \int_0^\infty \mathrm{d}q q^{D/2} \widehat{F}(q) J_{D/2-1}(qr), \tag{F.5}$$

where D is the dimension. This allows us to calculate the Fourier transform in any dimension with one simple and accurate method. We believe that this method is exceptionally well suited to investigate continuum percolation numerically. Since the pair connectedness function $P(r)$ becomes long-ranged near the percolation threshold, it is necessary that the range of the sampling in r extends to large values to properly sample the function. Secondly, upon approaching the percolation threshold, the $q \to 0$ component of $\widehat{P}(q)$ diverges. Hence, a small grid-spacing is necessary near $q = 0$ to properly capture the divergence. The use of a logarithmic grid allows us to do both without an excessively large number of grid points.

We now continue with the total number of grid points N and the logarithmic grid spacing $\Delta\tau$ and $\Delta\kappa$. We have chosen N as large as possible, such that we obtain results within a sensible time frame. For isometric particles, and anisometric particles in a small basis expansion, $N = 2^{18}$ was used. For the larger basis expansions, it was necessary to reduce the total number of grid points N to $N = 2^{13}$. The grid spacing $\Delta\tau$ was chosen such that the grid extends from $r_{\min} = 10^{-8}$ and $r_{\max} = 10^8$. While $\Delta\kappa = \Delta\tau$, the central point of the q-grid is slightly shifted to satisfy the so-called low-ringing condition of the transform, given by

$$\ln r_0 q_0 = \frac{L}{N}\left[\frac{1}{\pi}\mathrm{Arg}\left(2^{\pi i N/L}\frac{\Gamma(\nu/2+1/2+\pi i N/(2L))}{\Gamma(\nu/2+1/2-\pi i N/(2L))}\right) + z\right], \tag{F.6}$$

where L is the *logarithmic* period (*i.e.*, $\ln r_{\max} - \ln r_{\min}$), Arg gives the phase of the complex argument, Γ is the gamma function and z is an arbitrary integer number. This condition must be satisfied for maximum accuracy in the transform [92]. We find that $r_0 q_0 \approx 1$. While the method is

accurate in the central part of the transform, errors can accumulate at both small and large values for r and q. Therefore we found it necessary to only include the central parts of the transform, and set the lowest and highest quartile of the grid to zero [94]. Hence, we effectively reduce the grid from $r_{\min}, q_{\min} \approx 10^{-4}$ to $r_{\max}, q_{\max} \approx 10^{4}$. If the range of $P(r)$ is significantly smaller than $r_{\max}$, it is necessary to tune the upper limit such that the accumulation of errors is prevented.

While we can sample close to $q = 0$, this transform is not able to sample at $q = 0$ itself. Similarly, we do not sample for $r, q > r_{\text{text}}, q_{\max}$. The region far away from the origins is not a problem, as we can tune $r_{\max}$ sensibly, such that the connectedness functions P, C^{+} go to zero at the boundary of this domain. The region around $q = 0$ can be more problematic, as the divergence near the percolation threshold occurs at $q \to 0$. We could either use a sensible extrapolation for small values of r, q near $r, q = 0$, or only iterate up to densities where this lower boundary cut-off is not an immediate problem [95]. We find that the solution is insensitive to such lower-end correction, while the convergence rate of the solver is slightly increased. We have therefore opted to not include this lower-end correction.

Numerical Procedure

Now that we have discussed all relevant parts of the Fourier transform, we continue with the iterative solver. We show a schematic overview of the numerical procedure in Figure F.1. We have

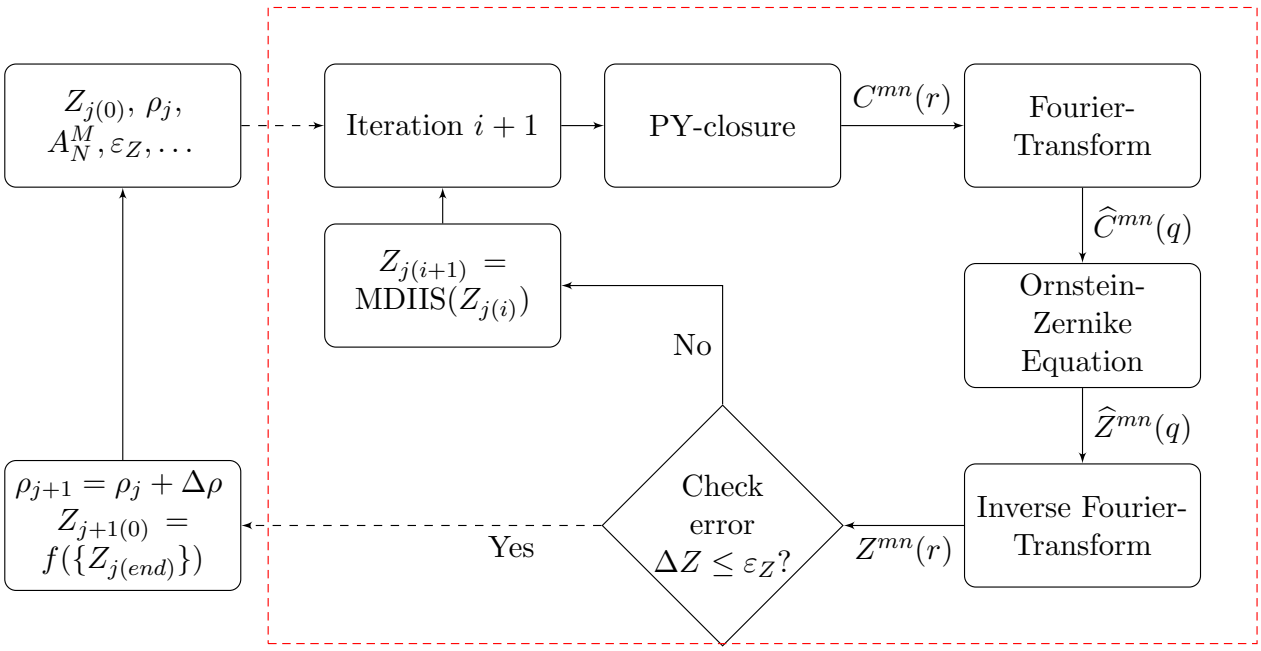

Figure F.1: Flowchart of the steps in the iterative solution strategy. It consists of two iteration procedures. The inner iteration denoted by the red box solves the (connectedness) Ornstein-Zernike equation at a fixed input density ρ_j. The outer iteration increases the density and insert an optimised input value $Z_{j(0)}$ into the inner iteration. MDIIS is an appreviation for the mixing scheme, see main text.

used the same strategy for both isometric and anisometric particles. For isometric particles the superscript mn are to be ignored. The iterative solver consists of two iteration procedures. The inner iteration is denoted in Figure F.1 by the red box. Here, the iteration number is given by i. The iteration number of the outer iteration is given by j. The iterative solver starts at zero density $\rho_0 = 0$, with initial guess $Z^{mn}_{0(0)}(r) = 0$. From the Percus-Yevick closure (4.15) we calculate $C^{+}_{0(1)}(r)$ from $Z_{0(0)}(r)$ and $A^{M}_{N}(r)$. Next, we take the Fourier (or Hankel) transform of $\{C^{mn}\}$ and insert this into Fourier-space Ornstein-Zernike Equation (4.9) to calculate a new value for $\widehat{Z}_{0(1)}(q)$. Finally we check if the error ΔZ is below a predefined value ε_Z. We define the error as

$$\Delta Z = \frac{1}{N}\sqrt{\sum_{l}^{N}\left(Z^{00}_{j(i)}(r_l) - Z^{00}_{j(i-1)}(r_l)\right)^2}. \tag{F.7}$$

If this error is smaller than a predefined error bound ε_Z, we assume the solution to be converged. We use $\varepsilon_Z = 10^{-4} - 10^{-8}$ as a convergence criterion. If the mean cluster size S becomes large, the denominator in the connectedness Ornstein-Zernike equation in Fourier space, $1 - \rho\widehat{C}^{00}(q) \approx 0$, and is therefore sensitive to small errors. Hence we find that is necessary to constrain the error in $C^{+}(r)$ as well, where we have used $\varepsilon_C = 10^{-5}$. If the error ΔZ and the error in $C^{+}(r)$ is larger than the convergence criterion, we construct a best guess for the next iteration $Z_{0(1)}$ by using a method known as the Modified Direct Inversion of Iterative Subspace (MDIIS) [96]. We discuss this method in more detail later.

If, after n iterations, the error ΔZ and the error in $C^{+}(r)$ are smaller than the error bounds, we assume the solution to have converged. We increase the density by $\Delta\rho$ and construct the next input value $Z_{j+1(0)}$ by extrapolating from previous solutions, see the next section. We have found that the convergence of the solver is highly sensitive on the input value, especially at high densities. We discuss the steps that we have taken to improve the convergence in the next section.

Convergence

The (connectedness) Ornstein-Zernike equation is known to be difficult to solve via simple iterative methods at high densities and either many iteration steps are necessary or convergence cannot not be achieved. We have applied two methods to improve the convergence of the method.

Initial guess

The convergence of the method is highly dependent on accuracy of the initial guess to the final solution. We start the iterative solver at low densities and increase the density with density increments $\Delta\rho$. At high densities, this is not enough and we approximate an initial guess for $Z_{j+1(0)}$ by using a second order backward finite-difference scheme, using both the first and second order derivative as

$$Z_{j+1(0)} = Z_j + \left(\frac{3}{2}Z_{j-1} - 2Z_{j-2} + \frac{1}{2}Z_{j-3}\right) + \frac{1}{2}\left(2Z_{j-1} - 5Z_{j-2} + 4Z_{j-3} - Z_{j-4}\right), \tag{F.8}$$

where Z_j represent the converged solutions. While the order of the backwards finite difference scheme is arbitrary, we did find that a two-point finite-difference scheme was not accurate enough. If the iterative solution does not converge, it is necessary to either change the density increments $\Delta\rho$, or reiterate previously obtained solutions to obtain better results.

MDIIS

The second method we have applied to improve the convergence is the use of the so-called Modified Direct Inversion of Iterative Subspace (MDIIS). This is a method that tries to estimate the best input $Z(r)$ for the next iteration step by using the last m solutions. This best guess is constructed from a linear combination of the last m input vectors

$$Z^*(r) = \sum_{l=1}^{m} c_l Z_{(l)}(r) \tag{F.9}$$

by requiring that the corresponding linear combination of the error vectors $R(r)$

$$R^*(r) = \sum_{l=1}^{m} c_l R_{(l)}(r) \tag{F.10}$$

approximates the zero vector in the mean-square sense [96]. We have used $R_{(l)}(r) = Z_{j(i-m+l)}(r) - Z_{j(i-1-m+l)}(r)$ as the error vector. The optimal estimate for the next iteration step is then given by

$$Z_{j(i+1)} = Z^*(r) + \delta R^*(r). \tag{F.11}$$

The number of included vectors m and the parameter δ are chosen such that the convergence is optimal. If the number of iterations is less than m, the next best guess is constructed from n vectors, where n is the number of iterations. While this method is relatively insensitive to the choice for m and δ at low densities, we found that at high densities $\delta \ll 1$ and $m > 10$ can be necessary. These few steps are repeated until the error (F.7) is smaller than the convergence criterion. If the error in Equation (F.7) grows significantly after the new iteration step, it can be necessary to restart the method from the solution with the lowest error vector. Hence we flush the last m input vectors and start again with one previous solution only. We have reset the iterative solution when the new error given by Equation (F.7) is one order in magnitude larger than the smallest error of the last m input vectors.

Test

We have tested our solver with the three-dimensional ideal particle model, for which an analytical expression for the mean cluster size S is known. While this does not test the correct implementation of the rotational invariant basis, it does confirm that our method is accurate enough to obtain sensible results. We can obtain the mean cluster size S from either $C^+(r)$ or $P(r)$ via

$$S = \frac{1}{1 - \rho\widehat{C}^+(0)}, \tag{F.12}$$

or

$$S = 1 + \rho\widehat{P}(0). \tag{F.13}$$

We find that the first method is unreliable. Equation (F.13) is significantly more accurate, and we therefore estimate the percolation threshold via Equation (F.13) only. While we are not entirely certain where this difference stems form, it is likely due to the fact that minor errors in $\widehat{C}^{+}(0)$ have a significant effect when $\rho\widehat{C}^{+}(0) \approx 1$, whereas this is not the case for Equation (F.13). In Figure F.2a we plot the mean cluster size S for the three dimensional ideal particle model. Here we have used a grid of $N = 2^{18}$, and have scaled the upper limit of the r-grid such that accumulation of errors is prevented. We observe no difference between the analytical solution and the numerical solution. In Figure F.2b we plot the relative error with respect to the analytical solution. The error is negligible everywhere except near the percolation threshold, where it increases sharply. We find the critical exponent $\gamma = 2.06 \pm 0.03$, and the percolation threshold $\eta_p = 0.5001 \pm 0.0001$, both of which are close to the analytical result $\gamma = 2$, and $\eta_p = \frac{1}{2}$. The relative error in γ is larger than the relative error in the percolation threshold η_p.

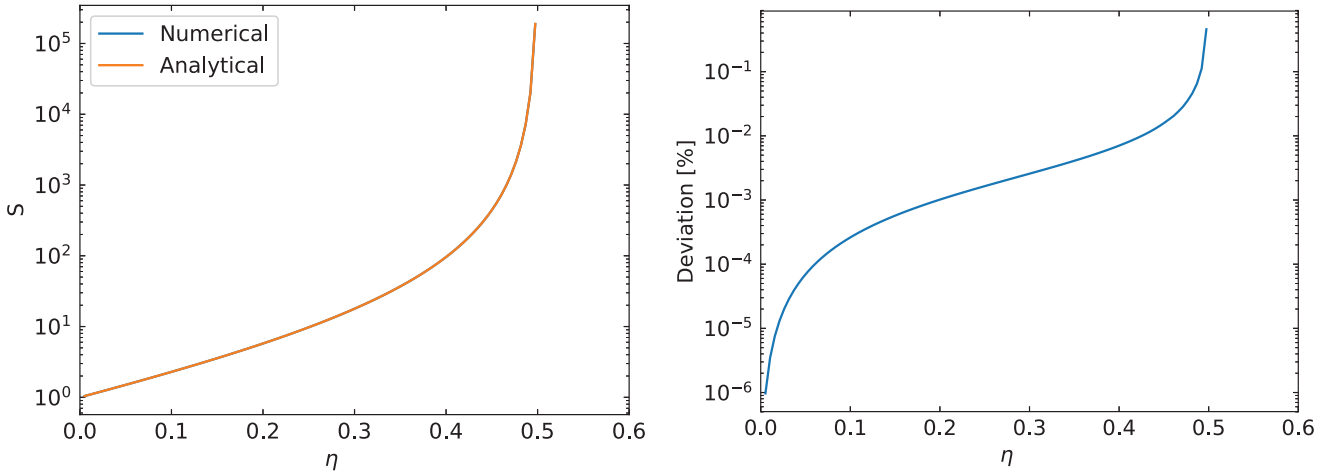

(a) (b)

Figure F.2: (a) The mean cluster size S as a function of the volume fraction η, where we have included both the analytical result and the numerical result. (b) A plot of the relative error in the mean cluster size S with respect to the analytical solution. The error is small everywhere except close to the percolation threshold.

Appendix G

Percolation in connected planes

Here we reduce the connectedness Ornstein-Zernike equation to matrix-form for a delta-wave approximation. In this approximation, we do not use the full smectic density distribution as obtained from the bifurcation analysis, but use a discrete distribution, where the centres of mass of the particles are positioned perfectly in pre-defined planes. Although the perfect spatial ordering into discrete layers is not physical, it can be seen as the limiting case in which the periodic density distribution becomes sharply peaked, and is tractable and gives simple insight into the effect of a periodic density modulation on the percolation threshold. We start by defining a density distribution as

$$\rho(z_1, \Omega_1) = \rho\psi(z_1), \tag{G.1}$$

where $\tilde{\rho}$ is the average density and $\psi(z_1)$ is the normalised density distribution function given by

$$\psi(z_1) = \sum_{l=1}^{n} \alpha\delta(z_1 - l\alpha). \tag{G.2}$$

Here, α is the layer spacing and n is the total number of layers. We define the surface density on each plane to be $\rho_0 = \rho\alpha$. Next, we insert this form for the density modulation in the definition of the inhomogeneous mean cluster size (2.8) and obtain

$$S(\vec{q}_r, \vec{q}_z) = 1 + \frac{A}{N}\int_{-\infty}^{\infty} \rho(z_2)\left[\int_{-\infty}^{\infty} \rho(z_1)P(\vec{q}_r, z_1, z_2)e^{iq_z(z_1-z_2)}\mathrm{d}z_1\right]\mathrm{d}z_2, \tag{G.3}$$

where A is the area of a layer and N is the total numbers of particles defined as

$$N = \int \rho(\vec{r})\mathrm{d}\vec{r} = n\rho\alpha A, \tag{G.4}$$

where n is the total number of layers. Inserting the definition for the density distribution into the mean cluster size gives

$$S(q_r) = \frac{1}{n}\sum_{m=1}^{n}\left(1 + \rho\alpha\sum_{l=1}^{n}\hat{P}(q_r, m\alpha, l\alpha)\right). \tag{G.5}$$

We can rewrite the connectedness Ornstein-Zernike Equation (2.12) in appropriate from by multiplying it with $\rho(z_2)$ defined by Equation (G.2) and integrating over z_2, from which we obtain

$$\widehat{P}(q_r, m\alpha, l\alpha) = \widehat{C}^+(q_r, m\alpha, l\alpha) + \rho\alpha \sum_{j=1}^{n} \widehat{C}^+(q_r, m\alpha, j\alpha)\widehat{P}(q_r, j\alpha, l\alpha), \tag{G.6}$$

We note that this equation is conveniently written in matrix notation as

$$\mathbf{P} = \mathbf{C}_c + \rho\alpha\mathbf{C}\mathbf{P}, \tag{G.7}$$

or

$$\mathbf{P} = \mathbf{C}_c[\mathbf{I} + \rho\alpha\mathbf{C}]^{-1}, \tag{G.8}$$

where $\mathbf{I}$ is the identity matrix,

$$\mathbf{P}, \mathbf{C}_c = \begin{bmatrix} f(q_r, \alpha, \alpha) & f(q_r, \alpha, \alpha) & \dots & f(q_r, \alpha, n\alpha) \\ f(q_r, 2\alpha, \alpha) & f(q_r, 2\alpha, 2\alpha) & \dots & f(q_r, 2\alpha, n\alpha) \\ \vdots & \vdots & \ddots & \vdots \\ f(q_r, n\alpha, \alpha) & f(q_r, n\alpha, 2\alpha) & \dots & f(q_r, n\alpha, n\alpha) \end{bmatrix}, \tag{G.9}$$

for $f = \widehat{P}, \widehat{C}^+$, and

$$\mathbf{C} = \begin{bmatrix} \widehat{C}^+(q_r, \alpha, \alpha) & \widehat{C}^+(q_r, \alpha, \alpha) & \dots & \widehat{C}^+(q_r, \alpha, n\alpha) \\ \widehat{C}^+(q_r, 2\alpha, \alpha) & \widehat{C}^+(q_r, 2\alpha, 2\alpha) & \dots & \widehat{C}^+(q_r, 2\alpha, n\alpha) \\ \vdots & \vdots & \ddots & \vdots \\ \widehat{C}^+(q_r, n\alpha, \alpha) & \widehat{C}^+(q_r, n\alpha, 2\alpha) & \dots & \widehat{C}^+(q_r, n\alpha, n\alpha) \end{bmatrix}. \tag{G.10}$$

We assume that particle connections can be made between nearest layers only, *i.e.*, $\widehat{C}^+(q_r, l\alpha, k\alpha) = 0$ for $|l - k| > 1$. The mean cluster size in the limit of infinite layers can be obtained by assuming periodic boundary conditions on $\mathbf{C}$, which we have evaluated with the help of Mathematica and results in

$$S = \frac{1}{1 - \rho\alpha\left(\hat{C}^+(0,0) + 2\hat{C}^+(0,\alpha)\right)}, \tag{G.11}$$

where $\hat{C}^+(0,\alpha) = \lim_{q_r \to 0} \hat{C}^+(q_r, l\alpha, k\alpha)$ for $|k - l| = 1$. It can also be solved in closed form for a finite number of layers. In this case, we can use a method developed by Hu and O'Connell [89], as the matrix $\mathbf{C}$ is a triband matrix with constant bands. This allows us to obtain the percolation threshold as

$$1 = \rho\alpha\left(\widehat{C}^+(0,0) + 2\cos\left(\frac{1}{k+1}\pi\right)\widehat{C}^+(0,\alpha)\right), \tag{G.12}$$

where k is the total number of layers in the model.